Magnetotransport studies of the single and bilayer two dimensional electron gas in the quantum Hall regime

ACADEMISCH PROEFSCHRIFT

ter verkrijging van de graad van doctor
aan de Universiteit van Amsterdam
op gezag van de Rector Magnificus
prof. dr. D.C. van den Boom
ten overstaan van een door het college voor promoties
ingestelde commissie, in het openbaar te verdedigen
in de Agnietenkapel
op vrijdag 11 juni 2010, te 10:00 uur

door

Giovanni Maria Galistu
geboren te Oldenzaal, Nederland

Promotiecommissie

Promotor:	Prof. dr. ir. A.M.M. Pruisken
Co-promotor:	Dr. A. de Visser
Overige leden:	Prof. dr. M.S. Golden
	Prof. dr. K. Schoutens
	Prof. dr. T. Gregorkiewicz
	Prof. dr. P.M. Koenraad
	Dr. I.S. Burmistrov

Faculteit der Natuurwetenschappen, Wiskunde en Informatica

The work described in this thesis was carried out at the Van der Waals-Zeeman Institute of the University of Amsterdam, Valckenierstraat 65, 1018 XE Amsterdam, The Netherlands.
The work is part of the research program of the Foundation for Fundamental Research on Matter [Stichting voor Fundamenteel Onderzoek der Materie (FOM)] and was made possible by financial support from the Netherlands Organization for Scientific Research [Nederlandse Organisatie voor Wetenschappelijk Onderzoek (NWO)].

‘‘*Nothing is too wonderful to be true if it be consistent with the laws of nature.*’’

(Michael Faraday)

‘‘ *En merk: Wij blijven toch eeuwig leken. Dat doet mij schier het harte breken.*’’

(Goethe’s Faust)

To my parents

Contents

1. Introduction

1.1 The classical Hall effect

In 1879 Edwin Hall discovered that the application of a magnetic field B perpendicular to a thin conducting slab through which a current flows produces a voltage across the slab and perpendicular to the current (*Fig.1*). This voltage has been called the Hall voltage V_H and the effect itself is called the Hall effect.

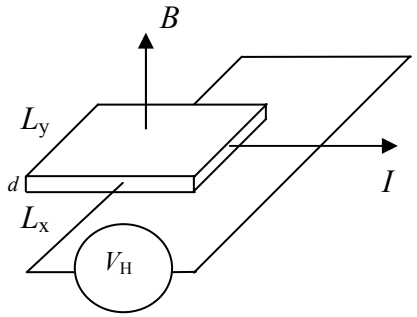

Figure 1.1 Schematic representation of the classical Hall effect.

So basically the Hall voltage is caused by the Lorentz force acting on the charges moving in the presence of a magnetic field. In equilibrium the Lorentz force $|F_L| = qv_DB$ is balanced by the electric force qV_H/L_y, where q is the carrier charge, v_D is the drift velocity and L_y is the width of the sample. So $V_H = v_DBL_y$ exhibits a linear dependence on the magnetic field B. Writing the current I as the product of the drift velocity v_D, the charge density n_q and the cross-sectional area of the sample $S = L_yd$, we find the perpendicular resistivity $R_H = V_H/I$ to be [1]

$$R_H = \frac{B}{qn_ed} = \frac{B}{qN_S}, \tag{1.1}$$

where $n_e = n_q/q$ is the number of carriers per unit volume and N_S is the number of carriers per unit surface area. Because the Hall resistance R_H only depends on the magnetic field B and the carrier density and not on other material parameters, the Hall effect has become a standard tool of material characterization. The direct proportionality of the Hall resistivity on the local magnetic field has allowed the development of scanning Hall probe microscopes which allow for instance a detailed determination of the magnetic field distribution near the vortices in type II superconductors [2]. The ordinary Hall effect can be fully explained by classical ideas about electron transport in metals, like the Drude model and the semi-classical theories elaborated in *Refs*. [3-5]. The fact that there is a quantum mechanical follow-up in the form of the quantum Hall effect which adds totally new dimensions to the study of low dimensional electronic systems, originally came as a complete surprise in physics as a whole.

1.2 The quantum Hall effect

The discovery of the ordinary Hall effect and advent of the quantum Hall effect (K. von Klitzing, 1980) are one century apart. The quantum Hall effect has already led to two Nobel prizes in physics, one for the integral quantum Hall effect [6] in 1985 and one for the fractional quantum Hall effect [7-9] in 1998. These robust quantum phenomena on a macroscopic scale Hall effect manifest themselves in the transport parameters of the two dimensional electron gas that are directly measurable, notably the longitudinal resistance (usually denoted by R_{xx} or R_0) and the Hall resistance (usually denoted by R_{xy} or R_H).

Still to date, more than 25 years after the first discovery, our microscopic understanding of the quantum Hall effect is far from being complete. The quantum Hall effect is standard observed in strong perpendicular magnetic fields B and at low temperatures ($T \leq$ 4 K) and it is well known that the phenomenon only exists because of the breaking of translational invariance by random impurities. Instead of the linear dependence of R_H with varying magnetic field B, it now turns out that the Hall resistance is quantized in units of h/e^2

$$R_H = \frac{h}{ie^2} \approx \frac{25.8128}{i} k\Omega \quad . \tag{1.2}$$

Here, i is an integer, h denotes Planck's constant and e is the charge of the electron. It is now generally accepted that the transitions between adjacent quantum Hall plateaus are continuous *quantum phase transitions* that are characterized by a diverging length scale ξ

usually termed the *localization length* of the electrons near the Fermi energy. The longitudinal resistance R_0 shows a peak at the transitions but it vanishes at the plateau values of R_H. The quantization phenomenon is extraordinarily accurate (better than one part in 10^8 [10]). This precision led the International Committee for Weights and Measures (CIPM) to adopt the quantum Hall effect as the new standard for electrical resistance in 1988.

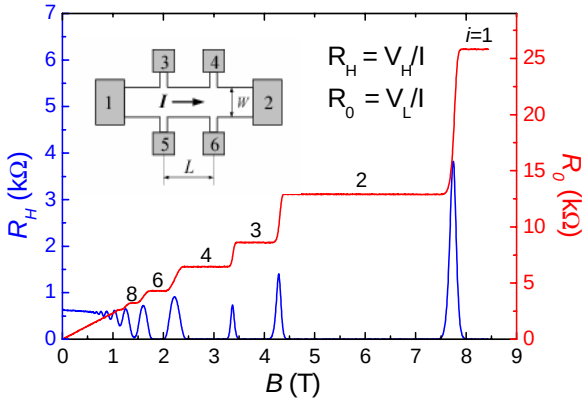

Figure 1.2 Quantum Hall effect measured on a sample with Hall bar geometry (top left corner). The Hall voltage V_H is measured between contacts 3 and 5 or 4 and 6. The longitudinal voltage V_L is measured between contacts 3 and 4 or 5 and 6. Data taken on an InGaAs/GaAs quantum well with electron density $n_e = 2.7 \times 10^{15}$ m^{-2} at T = 0.03 K). Figure taken from *Ref.* [11].

Years later Stormer *et al*. [12] discovered that under very specific circumstances (very clean samples or high mobility) i can assume a series of fractional values. In this thesis we consider only the integer quantum Hall effect. To explain the quantization of the Hall resistance one usually thinks in terms of simple pictures that assume the effects of Anderson localization in strong magnetic fields. Most popular are Laughlin's gauge argument [13], the semi-classical percolation picture [14], the Landauer-Buttiker edge states picture [15] and the heuristic ideas on Anderson localization by Aoki and Ando [16] that are based on Kubo formula [17].

One way to realize the two dimensional electron gas (2DEG) is by making use of MOS field effect transistors (MOSFETs). Another way is to use GaAs/AlGaAs heterostructures [18] or GaAs/InGaAs quantum wells [11]. In MOSFETs one can easily change the electron density by changing the gate voltage. This is also possible in III/V heterostructures and

quantum wells, but easier than building an additional gate is to control the electron density by illuminating the sample at low temperatures (if the Hall bar has the property of persistent photoconductivity).

The breaking of translational invariance is due to ionized impurities or lattice impurities, both of which contribute to the disorder of the system. Anderson localization phenomena in perpendicular magnetic fields strongly depend on the *range* of the potential fluctuations. *Short-ranged* disorder gives rise to strong scattering between the electrons whereas *long-ranged* disorder is usually associated with semi-classical pictures where open orbits ("edge" states) percolate throughout the system. What determines the type of disorder in quantum Hall samples is the *range* of the potential fluctuations relative to the *magnetic length* $l_B = \sqrt{(\hbar/eB)}$. It is well known that in order to experimentally observe the *quantum critical* behavior of the quantum Hall plateau transition, short-range potential fluctuations should be prevalent.

1.3 Landau quantization

A major ingredient for the quantum Hall effect is Landau quantization. In absence of a magnetic field the density of states $N(E)$ (or DOS) of th e 2DEG is constant up to the Fermi level and given by [13]

$$N(E) = \frac{m^*}{\pi\hbar^2} \tag{1.3}$$

where m^* is the effective carrier mass. The Fermi energy (E_F) is given by

$$E_F = \frac{\pi n_e h}{m^*}, \tag{1.4}$$

where n_e is the 2DEG carrier density. Under influence of a magnetic field B directed perpendicular to the 2DEG the DOS splits up in a discrete set of Landau levels (*LL*s) per subband n with energies [19]

$$E_{n,s} = (l + \frac{1}{2})\hbar\omega_c + m_s g^* \mu_B B, \tag{1.5}$$

where l is an integer, m_s is the spin quantum number, g^* is the Landé-factor, μ_B is the Bohr magneton and ω_c is the cyclotron frequency:

$$\omega_c = \frac{eB}{m^*} \tag{1.6}$$

The second term in *Eq*. 1.5 accounts for the spin splitting. It follows from *Eqs* 1.5 and 1.6 that the energy distance between the *LL*s is proportional to the applied magnetic field *B*. In order to observe the quantum Hall effect the energy splitting of the *LL*s should be much larger than the thermal broadening of a single *LL*, $\hbar\omega_c >> k_B T$, which requires typically the experiments to be carried out at liquid helium temperatures ($T < 4$ K). The number of occupied *LL*s, *i.e.* the number of *LL*s with $E_{n,s} < E_F$ is called the filling factor ν. The filling factor ν is related to the magnetic field

$$\nu = \frac{hn_e}{eB} \tag{1.7}$$

By increasing the magnetic field, the Landau levels are successively pushed to above E_F, which gives rise – under quantum Hall conditions – to the plateau-plateau (PP) transitions (see Figure 2). When the Fermi level is located between two *LL*s R_H attains a plateau value and $R_0 = 0$. Ideally the quantum Hall transitions occur at filling factors (n + ½), where n = 0, 1, 2 etc. These are called the critical filling factors (ν_c). In practice however ν_c may slightly deviate from the ideal values due to a finite overlap of the *LL*s [11].

1.4 Plateau-insulator transition

The quantum Hall transition at the lowest Landau level at ν_c = ½ is a very special one. In the limit of large magnetic fields the 2DEG becomes an insulator with R_H quantized at the value of h/e^2 [20]. This transition has been termed the plateau-insulator (*PI*) transition. An example of magnetotransport data taken on an InGaAs/InP heterostructure in this regime are shon in *Fig* 1.3 [21].

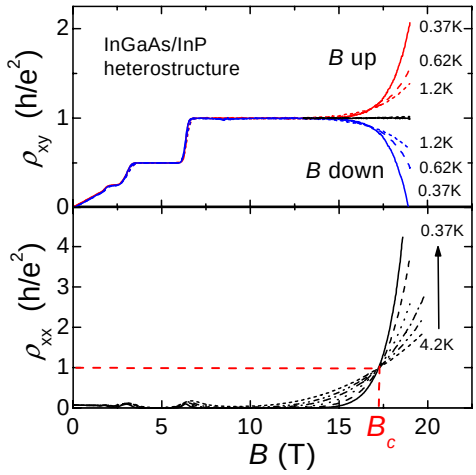

Figure 1.3 Magnetotransport data taken on an InGaAs/InP heterostructure ($n_e = 2.2 \times 10^{15}$ m^{-2}) covering PP transitions and the PI transition at $B_c = 17.2$ T. Upper frame: ρ_{xy} for positive and negative direction of the magnetic field B and the field-polarity averaged data. Lower frame: ρ_{xx}. Temperatures range from 0.37 to 4.2 K as indicated. Figure taken from *Ref.* [21].

The crossing point of the ρ_{xx} curves defines the critical field B_c at which the *PI* transition occurs. Due to sample inhomogeneities a sizeable component of ρ_{xx} is mixed into ρ_{xy} as seen in *Fig.* 1.3. However, by averaging over two polarities of the magnetic field ρ_H can be extracted from the ρ_{xy} data. An important feature to notice is that below the critical field B_c the longitudinal resistance decreases with decreasing temperature (metallic behavior) and above B_c the resistance increases with decreasing temperature (insulator type behavior). This is why often in literature this transition is referred to as a metal-insulator transition.

In this thesis we will focus on the plateau-insulator transition and extract the critical exponents of the quantum Hall quantum phase transition. The choice for the PI transition is motivated by the ability to deal with macroscopic sample inhomogeneities, which strongly affect the magnetotransport tensor and hamper a proper scaling analysis for the plateau-plateau transitions. This work strongly builds on the Ph.D thesis work of *Ponomarenko* [11] and *de Lang* [23].

1.5 Outline of this thesis

This thesis consists of seven chapters including this introduction.

In the second chapter several basic theoretical concepts relevant for the field of quantum phase transitions are introduced. We discuss scaling and power law behavior, and give the universal scaling functions for the conductivity tensor in the QHE. We illustrate relevant and irrelevant critical behavior with the help of a renormalization group flow diagram.
In Chapter 3 we present the experimental aspects of measuring the conductivity tensor on a Hall bar. We compare the commonly used AC-lock-in technique, with a newly implemented DC method, which we developed to reduce the effect of capacitive coupling for samples with very large resistance values. Sample details are also given in this Chapter.

In Chapter 5 we present a magnetotransport study on an InGaAs/GaAs quantum well in the quantum Hall regime. Data are taken at four carrier densities obtained by illuminating the sample. The PP-transition data are used to characterize the sample and determine the carrier density gradient of the Hall bar. The carrier density is evaluated with help of reflection symmetry and numerical simulations of the PP-transitions [11]. Next we investigate the longitudinal resistivity at the PI-transition and its critical behavior. The data are compared with previous results obtained on a different sized Hall bar [11]. Finally we report on a numerical study of the effect of the density gradient on the critical behavior of the PI transition for our specific Hall bar geometry.

Chapter 5 deals with the irrelevant critical behavior at the PI transition of the InGaAs/GaAs quantum well. We briefly discuss the concept of the "stress tensor" and distinguish between 'local' and 'global' variables. The ρ_H data are presented and analysed with a so-called data-collapse procedure, which gives access to the irrelevant critical exponent y_σ. Finally, we construct the renormalization group flow diagram and discuss its implications.

Chapter 6 deals with a different topic. Here we investigate the influence of a thin central AlAs barrier on the magnetotransport and optical properties of a δ-doped GaAs/InGaAs/GaAs quantum well. We first examine a series of six samples: three different pairs, each pair consisting of a sample with and without barrier. Magnetotransport data, photoluminescence data and wave function calculations are presented for the samples with and without barrier. It turned out that for this series of samples the δ-doping layers

themselves act as additional quantum wells and distort the shape and distribution of the wave functions. Therefore, a second series of samples was prepared and investigated.

In Chapter 7 again a new topic is introduced. Here we investigate the effect of a tilted magnetic field on an $In_xGa_{1-x}As/GaAs$ bilayer quantum well. In this material the Landé g-factor is much larger than the one in heterostructures that are traditionally used. This larger Landé g-factor will allow for a much larger spin splitting under influence of a magnetic field. Magnetotransport data in the quantum Hall regime for single (SQW) and double quantum wells (DQW) are presented and compared with each other. Several unique features in the data of the DQW system are explained using Landau level fan calculations.

1.6 References

[1] K.I. Wysokinski, *Eur. J. Phys.* **21** (2000) 535.

[2] A.M. Chang, H.D. Hallen, L. Marriott, H.F. Heu, H.L. Kao, J. Kwo, R.E. Miller, R. Wolfe, J. van der Ziel and T.Y. Chang, *Appl. Phys. Lett.* **61** (1992) 1974.

[3] L.D. Landau and E.M. Lifschitz, *Course in Theoretical Physics*, Vol. 8 (Pergamon Press, Oxford, 1984).

[4] A.A. Abrikosov, *Fundamentals of the Theory of Metals* (North-Holland, Amsterdam 1988).

[5] T. Ando, A.B. Fowler and F. Stern, *Rev. Mod. Phys*. **54** (1982) 437.

[6] K. von Klitzing, *Rev. Mod. Phys*. **58** (1986) 519.

[7] R.B. Laughlin, *Rev. Mod. Phys*. **71** (1999) 863.

[8] H.L. Störmer, *Rev. Mod. Phys*. **71** (1999) 875.

[9] D.C. Tsui, *Rev. Mod. Phys.* **71** (1999) 891.

[10] L. Bliek, E. Braun, F. Melchert, P. Warnecke, W. Schlapp, G. Weimann, K. Ploog, G. Ebert and G. Dorda, *IEEE Trans. Instrum. Meas*. **34** (1985) 304.

[11] L.A. Ponomarenko, *Ph. D Thesis* (University of Amsterdam, 2005), unpublished.

[12] D.C. Tsui. H.L. Stormer and A.C. Gossard, *Phys. Rev. Lett.* **48** (1982) 1559.

[13] R.B. Laughlin, *Phys. Rev. B* **23** (1981) 9375.

[14] J. H. Davies, *The Physics of Low-Dimensional Semiconductors*, (Cambridge University Press, Cambridge, 1998).

[15] M. Büttiker, *Phys. Rev. B* **38** (1988) 9375.

[16] H. Aoki and T. Ando, *Solid State Commun*. **38** (1981) 1079.

[17] R. Kubo, *J. Phys. Soc. Japan* **12** (1957) 570.

[18] T. Ando, A. B. Fowler and F. Stern, *Rev. Mod. Phys.* **54** (1982) 437.

[19] S. Datta, *Electronic Transport in Mesoscopic Systems* (Cambridge University Press, Cambridge, 1995).

[20] R.T.F. van Schaijk, A. de Visser, S. M. Olsthoorn, H.P. Wei and A.M.M. Pruisken, *Phys. Rev. Lett.* **84** (2000) 1567.

[21] D. de Lang, L.A. Ponomarenko, A. de Visser, C. Possanzini, S.M. Olsthoorn and A.M.M. Pruisken, *Physica E* **12** (2002) 666.

[22] D.T.N. de Lang, *Ph. D Thesis* (University of Amsterdam, 2005), unpublished.

2. Theoretical concepts

The quantum Hall effect (QHE) provides an exemplary study of quantum phase transitions (QPT). The most powerful theory to study (quantum) phase transitions available today is the renormalization group theory (RGT). Founding father of the RGT is K.G. Wilson [1-4], who in 1985 received the Nobel price for it. One of the strengths of the RGT is the capability of describing the system arbitrary close to the quantum critical point. This is done by renormalizing the system, i.e. redefining the concept of unity. Unity in the case of QPTs is defined by characteristic length scales, like the correlation length. When a system approaches the quantum critical point (QCP), a divergence of the characteristic length scales occurs. The RGT enables one to map a system asymptotically close to the QCP, thus having a certain length scale, onto the same system with a different length scale. None of the other existing theories, like mean field theory, and Landau-Lifshitz theory are capable of approaching the QCP as close as the RGT. The RGT predicts that the characteristic length scales of a system obey scaling. A system is said to scale if the equations of state, asymptotically close to the critical point, for different length scales are related to each other by so-called scaling factors (a_H and a_T). *Eq*. 2.1 gives a general expression of scaling behavior.

$$F_S(\lambda^{a_H} A, \lambda^{a_T} L) = \lambda F_S(A, L) \tag{2.1}$$

Critical exponents can always be expressed as a funtion of a_H and a_T. Systems with the same values of critical exponents and scaling functions belong to the same universality class. Essential to scaling is power-law behavior. If a system is proven to be renormalizable, this power-law behavior for the particular system is also observable by means of experiment. Pruisken has proven the renormalizability of the QHE for the non-interactive case in 1987 [5,6] and later for systems which include interactions [7]. The renormalizability of the QHE can be made visible in a so called renormalization flow

diagram. An example is given in *Fig*. 2.1. Basically the diagram shows the evolution of a quantum Hall system in the σ_{xx}-σ_{xy} plane as a function of the perpendicular magnetic field. Ideal semi-circles represent a homogeneous electron gas at $T = 0$ K (relevant flow). The vertical arrows in *Fig*. 2.1 show the flow of the system from $T \neq 0$ to $T = 0$ K (irrelevant flow).

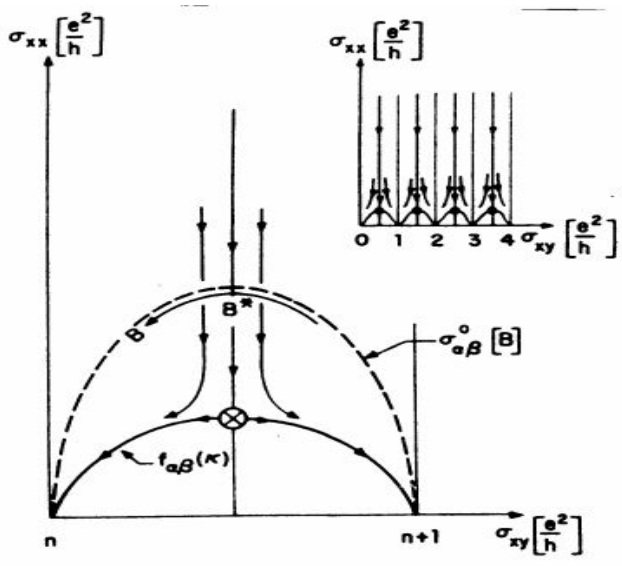

Figure 2.1 Renormalization flow diagram for the QHE. The top right corner shows four different transitions that obey the same scaling laws i.e. belong to the same universality class. Picture taken from *Ref.* [19].

The integer values $i = 0, 1, 2$ etc. on the σ_{xy} axis represent the stable fixed points. The values $i + ½$ represent the unstable fixed points. These are the QCPs at which the QPTs occur. At the QCP the components of the conductivity tensor attain the values [8]:

$$\sigma_{xx,c} = \frac{1}{2}, \sigma_{xy,c} = n + \frac{1}{2}; n = 0,1,2... \tag{2.2}$$

Using *Eq*. 2.2 we can define the scaling variables:

$$\sigma = \sigma_{xx} - \frac{1}{2}, \quad \theta = \sigma_{xy} - n - \frac{1}{2} \tag{2.3}$$

These are the variables that are transformed upon renormalization. The QHE effect is the only system in which the scaling variables can be directly measured. The conductivity tensor follows from the measured resistivities as shown in *Eq*. 2.4.

$$\sigma_{xx} = \frac{\rho_{xx}}{\rho_{xx}^2 + \rho_{xy}^2}, \quad \sigma_{xy} = \frac{\rho_{xy}}{\rho_{xx}^2 + \rho_{xy}^2} \tag{2.4}$$

Eq. 2.4 also describes the unusual state of both ρ_{xx} and σ_{xx} being zero when ρ_{xy} forms a plateau.

From a pure theoretical point of view the scaling functions can be constructed for $T = 0$. Experimentally this is inaccessible, so the scaling functions need to be adapted to the experimental situation of $T \neq 0$. This is done by coupling the temperature to the effective size of the system (finite-size scaling). As effective size is taken the phase coherence length L_φ:

$$L_\varphi = T^{-p/2}, \tag{2.5}$$

where p is the dynamical critical exponent. Renormalizing the system changes the effective size as: $L \to bL$, which in turn changes the scaling variables according to *Eq*. 2.1: $\theta \to b^{y_\theta}\theta$ and $\sigma \to b^{-y_\sigma}\sigma$, where y_θ is the relevant and y_σ the irrelevant critical exponent. Another relevant length scale is the localization length L_ξ:

$$L_\xi = \left|E - E_{n,s}\right|^{\chi}, \tag{2.6}$$

where $E_{n,s}$ is the energy at the center of the Landau level. When $L_\xi > L_\varphi$ electrons in the 2DEG are delocalized. The renormalization flow functions [9] have the shape:

$$\frac{d\sigma_{ab}}{d\ln L} = \beta_{ab}(\sigma_{xx}, \sigma_{xy}, c), \tag{2.7}$$

where

$$\sigma_{ab}(L_\varphi, B) = f_{ab}(L_\phi^{1/\chi}(B - B_c)) + O(L_\phi^{1/\chi}(B - B_c)^2, L_\varphi^{-y_\sigma}) \tag{2.8}$$

is the conductivity tensor and *ab* stands for the arbitrary combination of *x* and *y*.

It has been shown that the relevant exponent y_θ is just the inverse of the localization length exponent χ. From *Eq*. 2.8 we can draw two important conclusions. The first one is that the irrelevant exponent y_σ starts to play a role only at higher temperatures. The second (by

substituting the measurable quantity of T, using *Eq*. 2.5) is that the relevant critical exponent κ obtained by experiment equals:

$$\kappa = \frac{p}{2\chi} \tag{2.9}$$

The value of χ has analytically been estimated to be 2.3 ± 0.4 [10] for the non-interacting case. This is in good agreement with numerical results [11-16]. There is a strong uncertainty concerning the value of p, which is estimated to be bounded between 1 for the Fermi-liquid approach and 2, where the main scattering mechanism is due to electron-electron interactions, both for zero magnetic field [17]. Using these values for p and χ, the value of κ according to *Eq*. 2.8 should lie between 0.22 and 0.43. Consequently the exact value of κ is not predicted by theory, but can only be determined by experiment. In the experimental data certain quantities obey power-law temperature dependence involving κ as exponent. The width of the peaks in the ρ_{xx}-curves ($\Delta\nu$) and the maximum slopes of the transitions in the ρ_H-curves both obey power-law T dependence:

$$\Delta\nu \propto \left(\frac{d\rho_{xy}}{d\nu}\right)_{\max} \propto T^{\kappa} \tag{2.10}$$

In the same way the PI-transition around the crossing point satisfies the following relation (Shahar *et al.* [18]):

$$\rho_{xx}(\nu, T) = \frac{h}{e^2}\exp\left(-\frac{\nu - \nu_c}{\nu_0(T)}\right), \tag{2.11}$$

with

$$\nu_0(T) = (T/T_0)^{\kappa}, \tag{2.12}$$

where T_0 is a phenomenological temperature. The term between brackets in *Eq*. 2.11 is in fact the scaling variable X:

$$X = \frac{\nu - \nu_c}{(T/T_0)^{\kappa}} \tag{2.13}$$

It has been shown that for the QHE the components of the conductivity tensor, σ_{xx} and σ_{xy}, which are functions of both the magnetic field and the temperature (see *Fig*. 2.1), can in fact be described as functions of the single scaling variable X [19].

The corrections to scaling are described by the second term of *Eq*. 2.8. Even though present in every quantum Hall transition, the experimentally observable behavior that is only controlled by the irrelevant exponent y_σ is the deviation of the Hall resistance from the quantized value at the PI-transition:

$$\rho_{xy} = 1 + \eta(T)e^{-X},\ \eta(T) = (T/T_1)^{y_\sigma} \tag{2.14}$$

Here ρ_{xy} is given in units of h/e^2 and T_1 is a phenomenological temperature scale. The role of the critical exponents can be easily explained using the renormalization flow diagram (*Fig*. 2.1). Central in this diagram are the fixed points. Starting from the unstable fixed points at $\sigma_{xy,c} = n + ½$, with n being an integer, there are four directions to go: Two are along the semicircle ($T = 0$) towards the stable fixed points. The other two directions are toward the unstable fixed point originating outside the semicircle ($T \neq 0$). Simply put, the flow along the semicircle, in the neighborhood of the unstable fixed point is characterized by the relevant critical exponent κ, and the flow in the 'vertical direction' originating outside the semicircle is characterized by the irrelevant critical exponent y_σ.

The relevant and irrelevant critical behavior is combined in the universal scaling functions (to first order in X and η) [20]:

$$\sigma_0(X,\eta) = \frac{e^{-X}}{1 + 2\eta e^{-X} + e^{-2X}} \tag{2.15}$$

and

$$\sigma_H(X,\eta) = \frac{1 + \eta e^{-X}}{1 + 2\eta e^{-X} + e^{-2X}} \tag{2.16}$$

These functions describe every point in the renormalization flow diagram in the critical regime. Also they describe all quantum Hall transitions in the critical regime and for this reason are universal. So the relevant and irrelevant critical behavior is the evolution of a quantum state near the critical point, under influence of the magnetic field and temperature.

Eqs. 2.15 and 2.16 include two important symmetries concerning scaling behavior in the QHE.

- Particle-hole symmetry:

$$\sigma_0(X,\eta) = \sigma_0(-X,\eta) \tag{2.17}$$

$$\sigma_H(X,\eta) = 1 - \sigma_H(-X,\eta) \tag{2.18}$$

- Periodicity in σ_H.

The second symmetry is another expression of the universality of the quantum Hall transitions.

The concepts discussed in this chapter will be used to analyze the experimental results presented in chapters 4 and 5 of this thesis.

References

[1] K.G. Wilson, *Phys. Rev. B* **4** (1971) 3174.

[2] K.G. Wilson, *Phys. Rev. B* **4** (1971) 3184.

[3] K.G. Wilson, *Phys. Rev. D* **3** (1971) 1818.

[4] K.G. Wilson, *Rev. of modern physics* **47** (1975) 773.

[5] A.M.M. Pruisken, *Nucl. Phys.* **B285** (1987) 719.

[6] A.M.M. Pruisken, *Nucl. Phys.* **B290** (1987) 61.

[7] A.M.M. Pruisken and I.S. Burmistrov, *Annals of Physics* **316** (2005) 285.

[8] Y. Huo, R.E. Hetzel and R.N. Bhatt, *Phys. Rev. Lett*. **70** (1993) 481.

[9] M.A. Baranov, A.M.M. Pruisken and B. Škorić, *Phys. Rev. B* **60** (1999) 16821.

[10] A.M.M. Pruisken and I.S. Burmistrov, *Annals of Physics* **316** (2005) 285.

[11] J.T. Chalker and P.D. Coddington, *J. Phys. C* **21** (1988) 2665.

[12] B. Huckenstein and B. Kramer, *Phys. Rev. Lett.* **64** (1990) 1437.

[13] B. Mieck, *Europhys. Lett.* **13** (1990) 453.

[14] Y. Huo and R.N. Bhatt, *Phys. Rev. Lett*. **68** (1992) 1375.

[15] T.Ando, *J. Phys. Soc. Japan* **61** (1992) 415.

[16] D.H. Lee, Z. Wang and S. Kivelson, *Phys. Rev. Lett*. **70** (1993) 4130.

[17] E. Abrahams, P.W. Anderson, P.A. Lee and T.V. Ramakrishnan, *Phys. Rev. B* **24** (1981) 6783.

[18] D. Shahar, M. Hilke, C.C. Li, D.C. Tsui, S.L. Sondhi, J.E. Cunningham and M. Razeghi, *Solid State Commun.* **107** (1998) 19.

[19] A.M.M. Pruisken, *Phys. Rev. Lett*. **61** (1988) 1297.

[20] A.M.M. Pruisken, D.T.N. de Lang, L.A. Ponomarenko and A. de Visser, *Solid State Commun.* **137** (2006) 540.

3. Experimental aspects

3.1 Introduction

Traditionally magneto-transport measurements on two-dimensional electron-gasses (2-DEG's) in order to probe the quantum Hall effect have been done using the lock-in technique. The reason for this is that the measurements take place at temperatures ranging from a few Kelvin to sub-Kelvin temperatures and a very small current has to be used (varying from a few nano-amperes to even less than 1nA) in order to prevent Joule heating. Measuring with a small current becomes even more important when the 2DEG reaches the insulating regime and the resistance of the sample diverges exponentially, since heat is dissipated as the product of the resistance with the square of the current. Under these experimental conditions measuring the electrical resistance using the lock-in technique will give the best signal-to-noise ratio. The sinusoidal signal also causes thermal voltages present in the circuit to be averaged out, without any additional manipulation of the data required. The Hall and longitudinal resistances are measured using a four point configuration, such that the voltage and current leads in the circuit do not play a role.

Nevertheless, in spite of this great advantage of the lock-in technique, it turned out to be inadequate for our magnetotransport experiments when probing the 'irrelevant' critical behavior of the PI-transition of the quantum Hall effect. The main reason for this is that when the 2DEG enters the insulating state, its resistance increases drastically and the experimental circuit (wiring, cables etc.), due to the AC-nature of the measurement, gives rise to an additional capacitive coupling. Consequently not all the current flows through the Hall bar and the voltages measured over the Hall bar contacts become unreliable.

In this chapter the above mentioned method will be discussed together with its inadequacy to work under the extreme experimental conditions needed to observe the critical behaviour of the PI transition. Following this we will present an alternative method that has been used. Even though this DC-method cannot compete with the signal-to-noise ratio offered

by the lock-in technique, its application has overcome the main difficulty of capacitive coupling, connected to the ac-measuring method, mentioned before. Then a comparison of both methods will be made. Finally we will mention some adjustments that we made on the size of the Hall-bar in order to reduce the total resistance of the 2DEG once the system enters the insulating state.

3.2 Measuring techniques

3.2.1 AC-measuring

The alternating current (ac) - method is widely used to measure electrical resistance, by means of the lock-in amplification technique. The basic working principle of the lock-in technique is phase sensitive detection, i.e. the ability to extract a sinusoidal signal of known frequency and phase which is immersed in a 'background'. The total input signal measured with the lock-in amplifiers (V_{in}) can be represented within the complex plane in the following way:

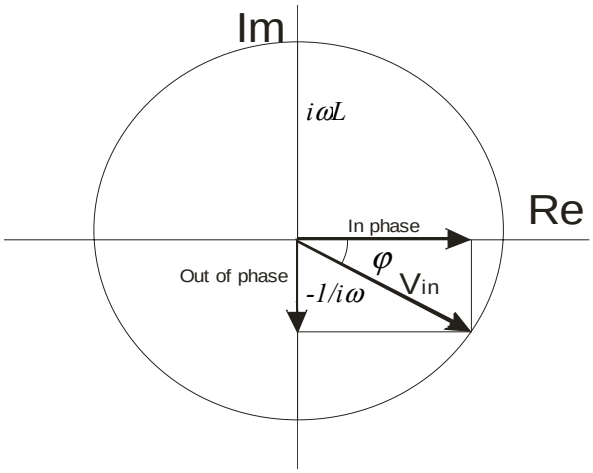

Figure 3.1 Representation of V_{in} in the complex plane. The input signal is shown here decomposed in an in-phase and an out-of-phase component. Note that a capacitor gives a phase shift of -90° with respect to the in-phase component and an inductance gives a phase shift of +90° with respect to the in-phase component.

A capacitor causes a phase shift of -90° and an inductance a phase shift of + 90°. The out-of-phase signal in *Fig*. 3.1 is the net vector of the capacitive effect and the contribution of a

possible inductance. A measurement scheme representing our experimental case is given in *Fig*. 3.2 [1].

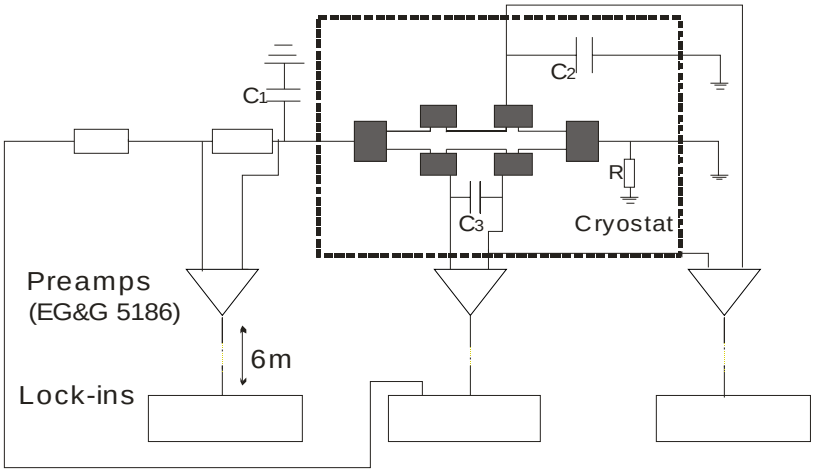

Figure 3.2 Scheme of the lock in amplification 4-point resistance measurement technique on a Hall bar. C_1, C_2, C_3 and R show unwanted capacitors and resistors an ac-current can flow through.

As *Fig. 3.2* shows, a big part of the measurement scheme consists out of wiring:

- The coax-cables connecting the lock-in amplifiers to the pre-amplifiers and the current cable connecting one lock-in amplifier to the top of the cryostat (~6 m)
- The coax-cables connecting the pre-amplifiers to the connector at the top of the cryostat
- The wiring connecting the connector at the top of the cryostat to the sample (~2 m)

At this point we should remark that the Hall bar needs to be completely isolated from its environment (sample-holder, cryostat) in order to prevent current flowing to ground, so '*R*' in *Fig.* 3.2 should be much larger than the resistance of the Hall bar. Basically there are three main constructions within the experimental setup that can contribute to the effect of capacitive coupling. These are shown in *Fig.* 3.2 as C_1, C_2 and C_3.

- C_1 is the capacitor formed by the core and the shield of a coax cable.
- C_2 is the capacitor formed by a wire and its environment, e.g. the cryostat.
- C_3 is the capacitor formed by two neighboring wires.

The impedance of a capacitor is given by:

$$Z = 1/(i \cdot \omega \cdot C) \tag{3.1}$$

where ω is the angular frequency and C is the capacitance. Capacitive coupling becomes a significant problem when the resistance of the sample becomes comparable to the impedances caused by C_1, C_2 and C_3 and is the main reason for the ac-method to become inadequate. From *Fig.* 3.2 the problem becomes clear immediately. Not all the current flows through the Hall bar. This means that the voltages measured by the lock-in amplifiers over the different Hall bar contacts are based on a current that is not exactly known to us. To give a quantitative example: Coax cables have a capacitance of 50 pF/m.
In the past in another similar cryostat the typical capacitance between wires for one contact pair has been shown to be around 700 pF [1]. Using the typical frequency of 13 Hz will give an impedance of $1/(\omega C) = 1/(2\pi fC) \approx 17$ MΩ. This becomes a problem in the insulating regime where the total resistance of the sample can reach values > 1 MΩ, meaning that not all the current flows from one current contact to the other. Measuring with a very low frequency is not a practical solution to the problem. In that case we would have to integrate over a much larger time scale (at least over ten periods of the input-signal [1]) to get an accurate averaging, which will cause a considerable delay in the measurement. This delay could be overcome by increasing the magnetic field at a lower sweep-rate, a process that would become too much time and helium consuming.

One could think of measuring the values of C_1, C_2 and C_3 and correct for the 'current-loss' due to them. This is also not a very practical solution. The reason is obvious. The reality is far more complicated than shown in *Fig.* 3.2. In fact current can leak away between every pair of wires and between every wire and its environment. To correct for this is a very difficult task at least. In the past a criterion has been set up based on the magnitude of the out-of phase component in order to determine whether the measured signal is reliable. It has been shown that if the out-of-phase component stays below 10 % of the in phase component, than the (systematic) error in the measured R (B) stays below one percent [1]. This follows easily from *Fig.* 3.1, where if the out of phase component is 10 % of the in-phase component, then $\varphi \approx 5$ deg and the in-phase component is still > 99 % of the real value. This criterion, regardless how helpful it has been in the previous measurements, has turned out to be not strict enough for the purpose of measurement presented in the following chapters.

It turned out that even if the 10 %-criterion was satisfied, the effect of capacitive coupling was still to high to give reliable data. Considering this limitation of the lock-in technique we decided to switch to a different method, based on a commutating DC- signal. This method will be discussed in the next paragraph.

3.2.2 DC-measuring

To measure DC we used a 6220 DC current source and a 2182A nanovoltmeter, both from Keithley Instruments Inc. The 6220 current source can generate currents from 0.1 pA to 105 mA. The 2182A voltmeter can measure voltages from 1 nV to 120 V. The input resistance of the voltmeter lies above 10 GΩ for all the measuring ranges. Measuring DC will give additional problems. Since there is no phase- or frequency dependent detection, we will have to deal with a higher noise level. Also a way has to be found to deal with thermoelectric voltages throughout the circuit. To deal with thermoelectric voltages we applied a measuring technique that makes use of commutating DC-current. A simple measurement scheme is shown in *Fig.* 3.3.

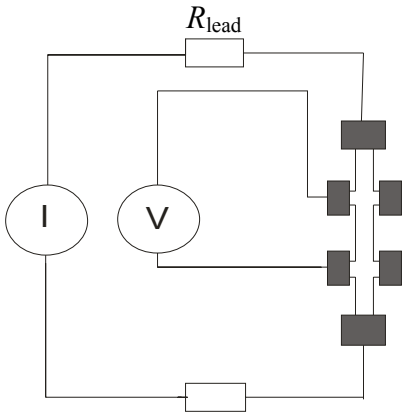

Figure 3.3 Schematic representation of 4-points DC measuring:
$V_{measured} = V_{Hallbar} + V_{thermoelectric} + V_{noise}$

Thermoelectric voltages can be dealt with by commutating the current. By averaging the measured voltages for $+I$ and $-I$ we can eliminate this contribution. In formula form this looks like:

$$V_{I+} = V_{Hallbar} + V_{Thermal}$$
$$V_{I-} = -V_{Hallbar} + V_{Thermal} \tag{3.2}$$

Thermoelectric voltages may vary in time (drift). In order to deal with the above mentioned problems we used the 3-step delta-method [2], [3] described next.

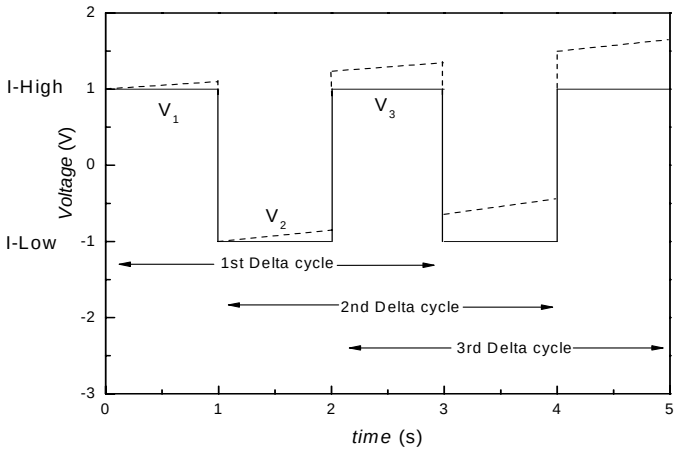

Figure 3.4 three-step delta method. The dashed line shows the situation, of a linear dependence of the thermoelectric voltages with time. Figure taken from [2], [3].

The final value V_f of the first delta cycle is calculated in the following way [2], [3]:

$$V_a = \frac{V_1 - V_2}{2}; V_b = \frac{V_3 - V_2}{2}; \quad , \qquad V_f = \frac{V_a + V_b}{2} \tag{3.3}$$

where V_1, V_2 and V_3 are the values of three successive steps in the delta method. The advantages of this method are twofold. It deals better with thermoelectric variation in the system and it does additional averaging on the data which helps improve the accuracy of the measurement. Every step in this procedure can be divided in two parts. The *delay time* and the *integration time*. The delay is needed to take into account the response time of the system. By adjusting this we can make sure that all the current goes through the circuit, before we start measuring the voltage during the integration time. The delay time should increase as the resistance we want to measure increases. The length of this integration-time

is expressed in PLC (power line cycle). One PLC is 0.02 s for 50 Hz. After each step the voltmeter gives one value, which is the average over the number of PLC's (NPLC) in that step. The higher the NPLC the more accurate the measurement of the voltage will be, but the longer it takes (see *Fig*. 3.5).

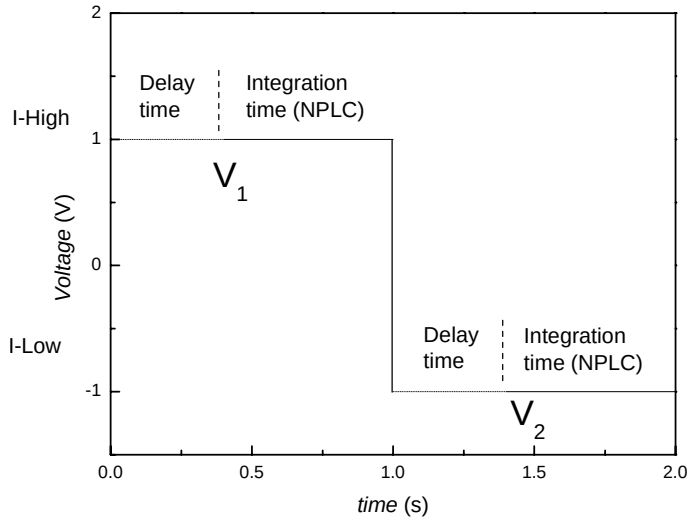

Figure 3.5 For one current polarity the measuring time is divided in a 'delay' and a 'time of integration', expressed in number of PLC's. Figure taken from [2].

A delay of 400 ms and a NPLC of 30 will give total period time of 2 s, which can be considered as 0.5 Hz (*Fig*. 3.5). Expressing this commutating behavior in Hertz can create the impression that this method is fundamentally similar to the AC method. This is actually not the case and the next point we make is a very important one. In the DC method a current source with adjustable output value is being used. The delay time in the voltage measurement makes sure that all the set-current goes through the circuit before the voltage is measured. Since the current during one step is completely DC in nature, this means that, in theory, all the set-current has to go through the Hall bar before the voltage measuring starts. The only period in time in which the current changes is when its polarity changes. Considering that during this period the voltage is not measured (if the delay time (*Fig*. 3.5) is bigger than the response time of the system), what is left is a way of measuring that is effectively 100% DC and the previous mentioned problem of capacitive coupling does not play a role anymore. Important now is to find a compromise between the accuracy of the

measurement and the time it takes, since we are dealing with a signal that varies in time. To reduce the noise level further, a so called 'moving filter' has been added, which averages over a subsequent number 'n' of values of V_f (*Eq*. 3.3), moves one value further, repeats the averaging, and so on. The question that now rises is: How does this DC-method compare to the traditional AC-method? This will be discussed in the next paragraph.

3.2.3 AC versus DC

The easiest way to compare these methods is to look at the insulating regime of the quantum Hall effect. Since the resistance of the 2DEG in this regime diverges exponentially as function of the magnetic field, we can expect that the method of measuring sooner or later will reach its limitation. In *Fig.* 3.6 the insulating regime measured both AC and DC is presented. The settings during both measurements where such that the time-constants (i.e. the time over which is averaged before the equipment gives a resistance value) were similar (~ 5 s). *Fig.* 3.7 shows that the out of phase component reaches about 6 % of the maximal resistance value. This is within the previous mentioned 10 % criterion. There is a clear difference between the ac and dc measured curve. This difference, however, is not only explained by the ac method losing accuracy due to capacitive coupling. In *Fig*. 3.8 the Hall resistivity is shown for the same density and temperature. A difference between the measured plateau values and the expected plateau values is obvious. The measured plateau values are about 1.5 % below the expected values. This difference can be attributed to an inaccuracy in the multiplication factor of the pre-amplifiers (*Fig.* 3.2). So every curve measured ac should be corrected for this. Multiplying the ac measured curve in *Fig.* 3.6 with a factor of 1.015 allows us to make a better comparison of both methods (see *Fig*. 3.9). The difference between the AC- and DC-curves in *Fig*. 3.9 is still considerable. At the critical value 'B_c' the difference amounts 7.5 %. The total sample resistance at this point is about 182 kΩ. The DC measured values are at each point higher than the AC measured values. Even though the above mentioned is a simple approach to the problem, it certainly speaks in favor of the DC-method. In section 3.3 we will look at the differences observed in the measurements of the Hall resistance.

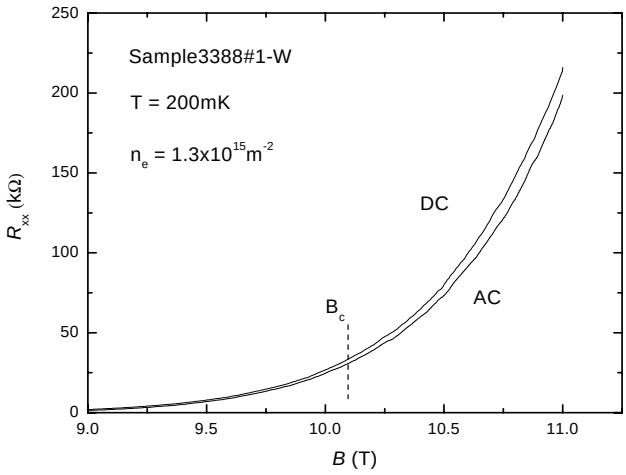

Figure 3.6 Insulating regime measured both AC and DC. AC: f = 2.6 Hz, I = 1 nA, TC = 5 s; DC: Del = 0.2 s; $NPLC$ = 15; MF = 2; I= 1 nA.

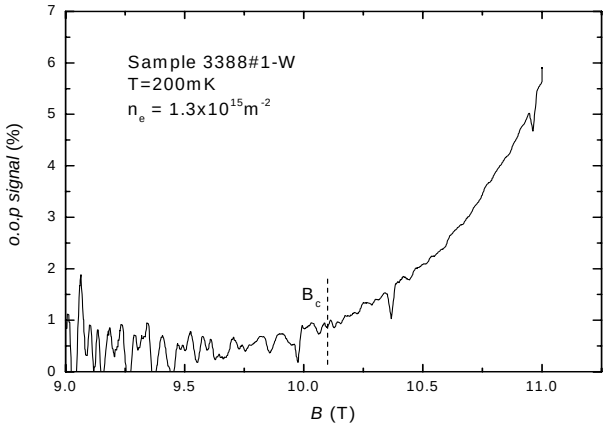

Figure 3.7: Out of phase component in percent of R_{xx}.

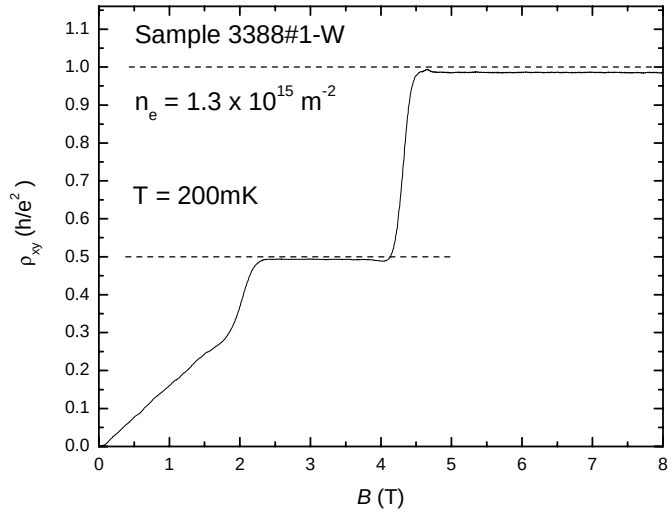

Figure 3.8 Hall resistance measured AC for n_e = 1.3 x 10^{15} m^{-2}. Dashed lines indicate the expected plateau values.

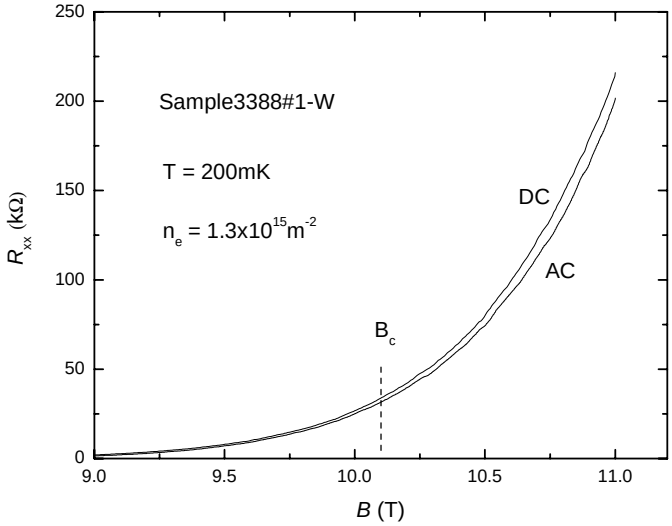

Figure 3.9 Same curves as in *Fig.* 3.6 only with the ac curve multiplied with a factor 1.015.

3.3 Capacitive coupling: The subtle difference

In the previous paragraph it has been shown that the effect of capacitive coupling strongly influences the resistance measurement in the insulating regime. We can assume that the influence of this capacitive coupling will be even more drastic while measuring the deviation from quantization in the insulating regime, since the effect we are after is very small (~ 100 Ω), compared to the actual measured signal (> 25 kΩ) and the total resistance of the sample. In *Fig.* 3.10 the ρ_{xy} -data measured for two field polarities at T = 0.8, 1.0 and 1.2 K are presented. From previous experiments we expect the averaged curves to show a positive deviation from the quantized value ρ_{xy} = 1 in units h/e^2 [1],[4]. This is clearly not the case for T = 0.8 K. In *Fig.* 3.11 we show the averaged curves both for the ac- and the dc-method. There is a big difference between the ac and dc measured data. Notably is that for the dc-method all the curves show a positive deviation. In *Fig.* 3.12 we show the out-of-phase component for the measured Hall resistances.

Indeed something peculiar happens: The increase of the out of phase signal is asymmetric for both field polarities. The effect of capacitive coupling is larger when measuring with positive field polarity. This explains why the ac-measured curves are always lower in magnitude than the dc-measured ones.

One might wonder where this asymmetry comes from. By changing the field polarity, we also change the polarity of the Hall voltage. Since every contact is wired differently in terms of length of cables, position of wires with respect to each other and with respect to the cryostat, it can be assumed that the effects of C_1, C_2 and C_3 (*Fig.* 3.2) are different for different field polarities.

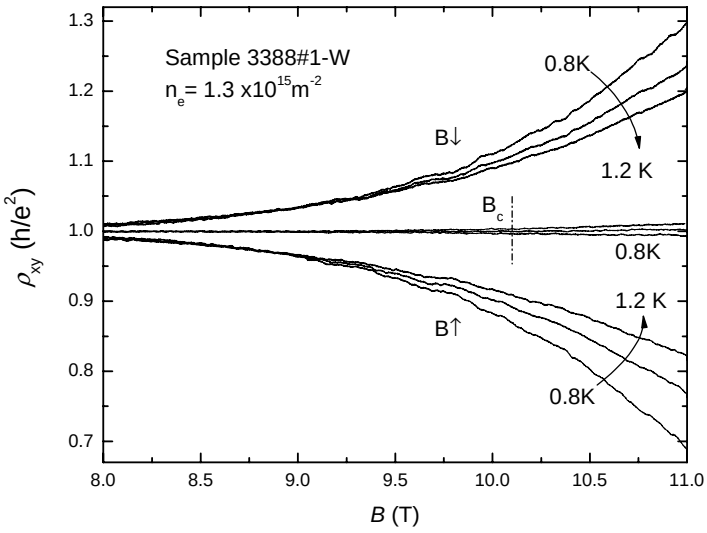

Figure 3.10: Hall resistance measured AC for both positive and negative field near the PI-transition at T = 0.8, 1.0 and 1.2 K plus the averaged curves for both field polarities.

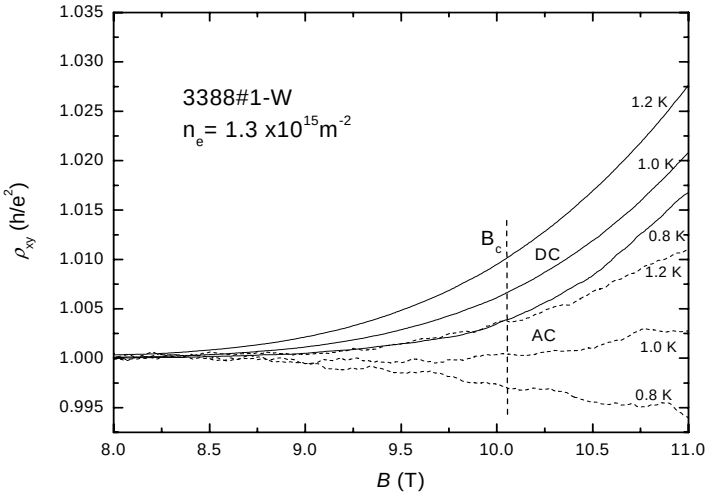

Figure 3.11 Hall resistivity for T = 0.8, 1.0 and 1.2 K measured with both the ac- and dc-method. Dashed lines: AC; solid lines: DC.

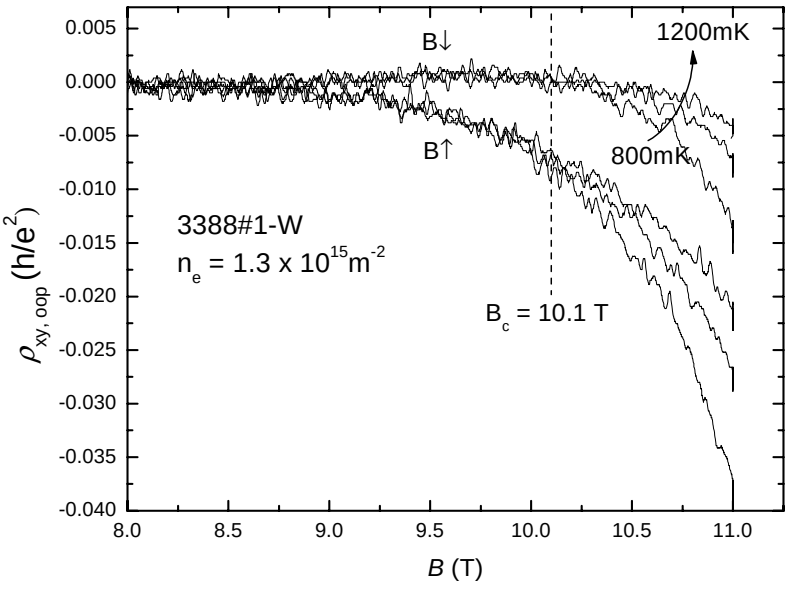

Figure 3.12 Out op phase component of the R_{xy} measurement for positive and negative magnetic field.

3.4 Shape of Hall-bar

Since we want to keep the resistance of the 2DEG as low as possible we have designed a Hall-bar with different dimensions than the one used in previous measurements [1]. The newly designed Hall bars have a width of 200 μm against the 75 μm of the Hall bar described in [1]. The total length of the Hall bar has been adapted to assure that the current between the voltage-contacts flows parallel to the Hall bar. Our decision has been supported by numerical calculations [1]). The dimensions of the Hall bar that we used are displayed in *Fig.* 3.13.

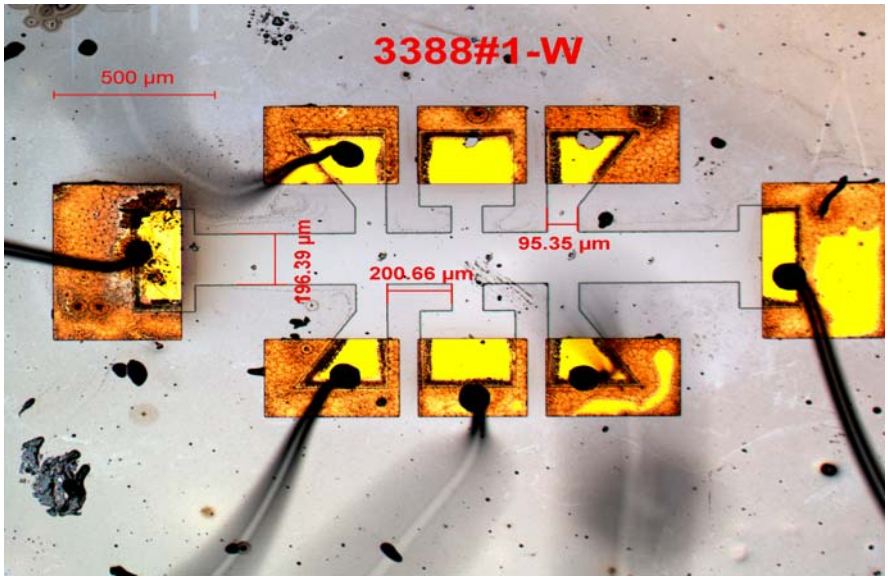

Figure 3.13 Sample 3388#1-W with respective dimensions.

Notice that the geometrical factor (Length/Width) now becomes 1.5, with respect to the previous 5.2 [1], keeping the longitudinal resistance more than three times as low. In *Table* 3.1 a comparison is made between both Hall bars at the PI- transition. Both samples were made from the same wafer, which is an $In_{0.2}Ga_{0.8}As/GaAs$ quantum well grown by MBE. The quantum well is a 12 nm thick $In_{0.2}Ga_{0.8}As$ layer, separated by the doping layer by a 20 nm thick spacer. There is no caplayer. The Hall bars were etched by photolithography.

Table 3.1 Comparison of R_{xx} and $R_{Hallbar}$ at the PI-transition for 3388#1 and 3388#1-W

Hallbar	(L/W)	R_{xx} (kΩ)	$R_{Hallbar}$ (kΩ)
3388#1	(5.2)	134.2	498.5
3388#1-W	(1.5)	38.7	219.3

It is clear that Hall bar 3388#1-W is the most suited of the two for our aim of keeping the total resistance of the Hall bar as low as possible.

3.5 Conclusions

In this chapter two different methods of measuring the magnetotransport properties of a Hall bar made of a 2DEG in the quantum Hall regime have been discussed.

- The traditional low frequency ac-method using the lock-in technique
- The dc-method which through signal averaging and commutation has been adapted to make it suitable for measurements using very low excitation currents.

Due to the nature of the dc-method the problem of capacitive coupling, inherent to the ac-method, can be strongly reduced or avoided completely, depending on the measurement parameters ‘delay time’ and ‘NPLC’ (*Fig.* 3.5). Thus the dc method compares favorable when measuring Hall bars in the high-ohmic regime of the plateau-insulator transition.

3.6 References

[1] L.A. Ponomarenko, *Ph.D Thesis* (University of Amsterdam, 2005), unpublished.

[2] Keithley Instruments Inc., Model 6220 DC Current Source User's manual, *622X-900-01 Rev. B*/June 2005. www.keithley.com/products/locurrhiresist/?path=6220/Documents#6

[3] Keithley Instruments Inc., Model 2182/2182A Nanovoltmeter, User's manual, *2182A-903-01 Rev. A*/ June 2004. www.keithley.com/products/lovoltloresist/nanovoltmeters/?path=2182A/Documents

[4] A.M.M. Pruisken, D.T.N. de Lang, L.A. Ponomarenko and A. de Visser, *Solid State Commun.* **137** (2006) 540.

4. Critical behavior

4.1 Introduction

During the last two decades, following the discovery of the quantum Hall effect by von Klitzing *et al.* [1] and the pioneering work on quantum criticality of the PP-transitions by Wei *et al*. [2a-3], a host of experimental work has been done in order to shed light on the exact nature of scaling in the quantum Hall regime at low temperatures. The principal objective is to establish the following scaling laws for the experimentally observed Hall resistance R_{H} and the longitudinal resistance R_0 with varying magnetic field B and temperature T [2b]

$$R_{H,0} = F_{H,0}(\Delta B, T^{-\kappa}) \tag{4.1}$$

Here, $\Delta B = B - B^*$ is the magnetic field relative to the critical value B^* which corresponds to the center of a Landau band. The critical exponent κ equals the ratio

$$\kappa = p / 2\nu_0 \tag{4.2}$$

with ν_0 denoting the localization length exponent of the 2DEG and p is a finite temperature exponent determined by inelastic scattering. *Eq*. (4.3) determines the maximum slope of the Hall resistance R_{H} with varying B to diverge algebraically as T goes to zero according to

$$\left(\frac{\partial R_H}{\partial B}\right)_{\max} \propto T^{-\kappa}. \tag{4.3}$$

Wei *et al.* originally extracted the numerical value $\kappa = 0.42$ from the transport data taken from a low mobility *InP-InGaAs* heterostructure which is independent of the index of the PP transition [2a-3]. Following the renormalization theory of the quantum Hall effect developed by Pruisken [2b] this experimental value was subsequently regarded to be universal.

These remarkable advances have led several groups around the world to investigate the power law of *Eq*. (4.3) for a variety of different but otherwise arbitrarily chosen laboratory samples [4-7]. A range of different values for κ were measured, however, varying from 0.3 to 0.9. The difficulty in experimentally establishing universality of the PP transition has

caused the quantum Hall community to split up into two different groups with entirely different physical objectives each.

4.1.1 The 'H.P. Wei' school of thought

The first group, briefly termed the 'H.P. Wei group', held on to the general belief that the critical exponent κ is universal. Motivated by the theoretical foundations of scaling established by Pruisken, this group experimentally pursued the universality of not only κ but also the complete scaling functions $F_{\mathrm{H},\,0}$ with varying T and B. It was well understood, however, that universality strictly holds in the limit where T goes to absolute zero. In practice this means that the transport measurements at finite T should be conducted on sufficiently homogeneous samples with potential fluctuations that are short-ranged relative to the magnetic length.

4.1.2 The 'phenomenological' school of thought

Quite unlike the experimental objectives of the H.P. Wei group, the second school of thought, briefly termed the 'phenomenological group', went on in different directions altogether. For example, to explain the differences in the experimental κ; finite size scaling experiments have been conducted that were aimed at disentangling the individual exponents values of p and ν_0. These investigations led to the idea that the exponent p, unlike the localization length exponent ν_0, is a material dependent parameter that varies not only from sample to sample but also from Landau level to Landau level.

At a much later stage, experiments conducted on a new class of high quality samples indicated yet a very different behavior. Rather than a *power law* in T, the transport data were now fitted to a semi classical '*linear law.'* (Shahar *et al*. [8]) This kind of data fitting clearly does not teach us anything about the phenomenon of Anderson localization and fundamentally upsets the entire idea of quantum criticality in the quantum Hall regime.

At the time of this writing, the various conflicting results and ideas advocated by the 'phenomenological school of thought' seem to have lost most of its support in the literature. What has in general been overlooked by this group is that the transport data taken from arbitrary samples at finite T do not necessarily reveal the true (scaling) behavior of the

2DEG in the limit $T = 0$. It may therefore not be a complete surprise to know that the most important advances in the field have emerged from entirely different sources.

4.1.3 The PI transition

First, there is the longstanding experimental problem of how to disentangle the effects of macroscopic sample inhomogeneity from the intrinsic transport properties of the 2DEG. In brief, it has turned out that defects such as small gradients in the electron density can cause major aberrations in the extraction of κ from the PP transitions [11-14]. These as well as other kinds of defects such as contact misalignment have a much less dramatic impact when the measurements are conducted on the PI transition. Subsequently, the PI transition became the primary focus of experimental interest.

The most important conclusions drawn from the experiments on the PI transition can be found in *Refs* [15,16]. Unlike the 'generally accepted' exponent value $\kappa = 0.42$ previously obtained from three different PP transitions of an *InP-InGaAs* heterostructure, the *correct* experimental value extracted from the PI transition of the same sample turns out to be $\kappa = 0.57$. The difference between these two experimental estimates can be explained based on density gradients that dramatically complicate the experiment on the PP transition but do not affect the κ taken from the PI transition.

The detailed studies on the PI transition furthermore revealed universal scaling functions for the longitudinal conductance σ_0 and the Hall conductance σ_H. These scaling functions, when plotted as T-driven flow lines in the σ_0-σ_H conductance plane, display all the fundamental features of scaling that previously could not be observed from the data taken from the PP transitions. As pointed out in the original papers, these findings provide important information on the unification of the fractional quantum Hall effects based on composite fermion theory, in particular, the cross-over between the half-integral Fermi-liquid state and the quantum critical state.

Even though the advances made on the PI transition have resolved many longstanding controversies in the field, several major experimental difficulties have nevertheless remained. For example, since not much is known about the microscopic details of the low mobility *InP-InGaAs* heterostructure it is unclear whether the criteria for a homogeneous, short ranged random potential are being satisfied. The random alloy scattering in these

samples may, in fact, exhibit long-ranged components relative to the magnetic length. This would mean that the newly extracted value of $\kappa = 0.57$ is, in fact, an effective exponent and even lower temperatures are needed in order to be able to extract the much sought-after critical value.

4.1.4 Numerical value of κ

This takes us to the second important advance more recently made by the Princeton group of D.C. Tsui who investigated the PP transitions taken from a set of specially grown state-of-the-art $Al_xGaAs/Al_{0.33}Ga_{0.67}As$ heterostructures with different *Al* concentration *x* [17,18]. By varying *x* one effectively varies the range of the potential fluctuations in these otherwise extremely homogeneous samples. For example, for small values of *x* the *Al* atoms are all distant apart from each other and the disorder potential is predominantly *long- ranged*. On the other hand, by increasing the concentration *x* the *Al* atoms come closer together and the random potential fluctuations become predominantly *short-ranged*. Upon further increasing the concentration *x* the *Al* atoms are believed to form clusters. This clustering takes place over distances which are large relative to the magnetic length and, hence, the randomness becomes *long-ranged* again.

The experimental values for κ extracted for different values of *x* generally exceed the value 0.42. However, when the criteria for *short range* potential fluctuations were met D.C. Tsui *et al.* measured a value of $\kappa = 0.42$ in the temperature range from10 to 1000 mK. This experimental value - which surprisingly coincides with the original but incorrect result of H.P. Wei *et al*. - is now believed to be the correct universal value of κ. These impressive findings by the Princeton group unequivocally demonstrate the existence of quantum criticality in the quantum Hall regime and, hence, the correctness of the `H.P. Wei' school of thought.

4.1.5 Confronting controversies

The advances made on both the PI transition and the critical exponent κ are an important step toward establishing a unified renormalization theory of the quantum Hall effects. At the same time, these advances are a landmark in the theory of Anderson localization and interaction effects. However, the subject matter is still at its infancy and certainly not free of controversies. First of all, it is important to emphasize that the newly established value

of $\kappa = 0.42$ has absolutely nothing to do with the original findings of H.P. Wei *et al.* Unlike the claims made by D.C. Tsui *et al.*, the coincidence is purely accidental thus creating a lot of confusion. The only way to understand the original H.P. Wei result of $\kappa = 0.42$ is by considering the combined effects of both *long ranged* potential fluctuations and macroscopic sample *inhomogeneity*. Whereas the former causes the experimental κ to *increase* from the universal value 0.42 up to the aforementioned value of 0.57, the latter causes κ to *decrease* from 0.57 back to the numerical value 0.42. Notice that this combination of experimental defects typically explains the different values of κ in the range 0.3 – 0.9 previously extracted from arbitrarily chosen samples at finite temperatures.

Secondly, there are the more recent attempts by the Princeton group to disentwine the critical exponents p and ν from the definition of κ in *Eq*. (4.0) [19]. In particular, by studying the scaling of the PP transition with varying sample size L rather than T, the individual exponent values have been extracted and the result is $p = 2$ and $\nu = 2.4$ respectively. Since the localization length exponent ν is numerically the same as the free electron result known from computer simulations, D.C. Tsui *et al.* conclude that the critical behavior of the interacting electron gas and the disordered free electron gas are in the same universality class. According to Pruisken this conclusion is incorrect. In particular, the advances made in the theory of localization and interaction effects have clearly shown that the infinitely ranged Coulomb interaction present in the laboratory sample renders the transport of the 2DEG entirely non-Fermi liquid-like. This transport behavior is characterized by previously unrecognized interaction symmetries (termed F-invariance) as well as distinctly different non-Fermi liquid critical exponent values.

The experimental problem that was discarded by D.C. Tsui *et al.* is that finite size scaling can only be studied if it compares the data taken from *different* samples. However, along with different values of L one also finds that the characteristic length scale L_s and temperature scale T_s for scaling varies from sample to sample in an uncontrolled manner. Unlike κ which is measured on a single sample, there is as of yet no experimental design that warrants an unambiguous measurement of the individual exponent values of p and ν.

Last but not least, the samples used by D.C. Tsui *et al.* do not permit an investigation of the PI transition since that lowest Landau level displays the fractional quantum Hall effect. This most likely complicates the study of macroscopic inhomogeneity effects and, along with that, the subtleties of a unified scaling diagram that incorporates both the integral and

fractional quantum Hall effects. In any case, D.C. Tsui *et al.* do not investigate the universal scaling functions for σ_0 and σ_H and it remains unclear whether the PP transitions of their samples provide access to the *irrelevant* exponents describing the corrections to scaling. Future work probably will tell.

4.1.6 Outline of this Chapter

In this chapter we will present the results of magnetotransport measurements conducted on an InGaAs/GaAs quantum well with a geometrical factor of 1.5 (see *Fig*. 3.11) using four different electron densities (n_e = 1.0, 1.3, 1.8 and 2.0 × 10^{15} m^{-2}). We will consider both the PP and PI transition. Whereas the PP transitions give us the necessary information about the quality of the Hall bar in terms of density gradients, only the PI transition will be used to study quantum criticality.

The analysis of the data is done in much the same way as was done previously in *Refs* [11-14]. The results will be compared with those obtained from a similar quantum well with a geometrical factor of 5.2 in *Ref* [11]. We will discuss the results of numerical simulations and see to what extent the relatively large gradients in the electron density of the 2DEG can explain the deviations found in the curves displaying critical behavior.

Using our experimental results discussed in this Chapter as well as *Chap*. 5 we will construct a *T*-driven flow diagram that displays both relevant and irrelevant critical behavior. We then compare the results with the theoretical predictions on scaling similarly to what was previously done in *Ref.* [15].

4.2 InGaAs/GaAs quantum well with tunable carrier density: PP transition

The InGaAs/GaAs 2DEG used for our magnetotransport measurements has a tunable carrier density. Being insulating in the dark, the electron density in the quantum well can be increased by illuminating the 2DEG with an infrared LED at low temperatures.

The carrier density is an important parameter of the 2DEG since it determines at which values of the magnetic field the quantum Hall transitions occur. By changing the carrier density in the range in which the field-value at which the PI transition occurs is still achievable with our magnet, we can create different sample conditions. This allows us to

check for the universality of the critical exponents. The wafer out of which the Hall bar was prepared has been grown by molecular beam epitaxy (MBE) at the Moscow state university. The 2DEG is located in a 12 nm thick $In_{0.2}Ga_{0.8}As$ layer, separated from the doping layer by a 20 nm thick spacer. Etching of the Hall bar was done using photolithography. The carrier concentration in the sample can be varied smoothly between zero (insulating sample) and $n_e = 4 \times 10^{15}$ m^{-2} with an accuracy better than 1 % [11]. To illuminate the 2DEG we send a current through the LED using a Keithley 2400 current source. The illumination was done stepwise by controlling the pulse duration and slowly increasing the current through the LED. An image of the Hall bar is shown in *Fig*. 3.11 of the previous chapter. The Hall bar has 6 potential and 2 current contacts. Unfortunately one current contact and two potential contacts turned out to be high-Ohmic which reduced the possibility of directly probing the inhomogeneities in the carrier density of the Hall bar. Still there are other methods available to estimate the inhomogeneous nature of the carrier density. These methods have been applied and will be discussed in this chapter. In the following *Figs*. 4.1 a) - d) we will show the resistance- and Hall curves measured DC for the four densities attained after longer and longer illumination. All curves where measured using the DC method described in *Chap* 3.

Figs. 4.1 a) – d) show the expected improvement of the quality of the data with increasing density. For the highest two densities (*Figs*. 4.1 c, d) the small overshoot of the resistivity (ρ_{xy}), at the beginning of the plateaus, still visible in the lowest two densities (*Figs*. 4.1 a, b), disappears. The plateaus become quantized within 0.05 % of the expected values and ρ_{xx} becomes zero between the transitions.

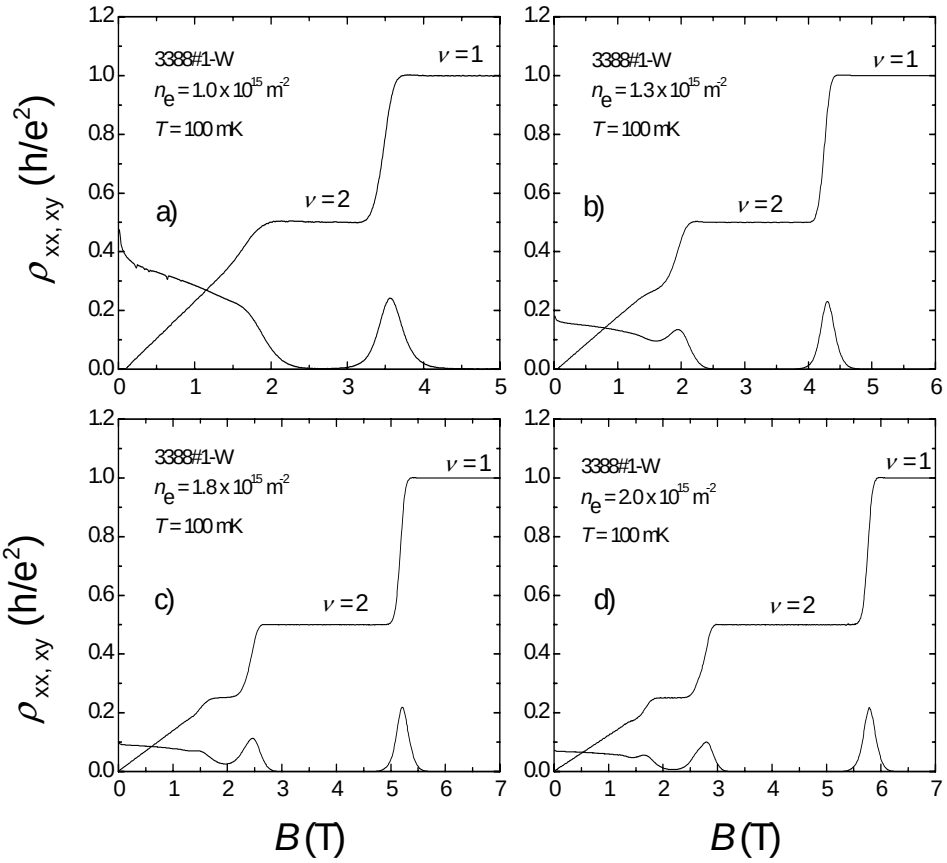

Figure 4.1 Resistance and Hall-curve for a) $n_e = 1.0 \times 10^{15}$ m^{-2}, b) $n_e = 1.3 \times 10^{15}$ m^{-2}, c) $n_e = 1.8 \times 10^{15}$ m^{-2} and d) $n_e = 2.0 \times 10^{15}$ m^{-2}. The measurement current is 10 nA. T = 100 mK.

4.2.1 Determining inhomogeneities

A great obstacle in probing the quantum critical behavior is the inhomogeneous nature of the Hall bar. Inhomogeneities in the electron density of the 2DEG are mainly a result of the growth process of the wafer. The simplest approach to the inhomogeneity problem is a gradient in the electron density throughout the Hall bar. The most harmful consequence of inhomogeneities is that transitions take place at different values of the magnetic field

throughout the 2DEG and make an accurate determination of the scaling behavior impossible. This is especially true for the PP transitions [11]. It is important therefore to be able to make an estimate of the magnitude of this gradient in the electron density. The common way of doing this is to measure the Hall resistance at two places of the Hall-bar. The shift in curves then tells us how large this gradient is. Unfortunately only one pair of Hall contacts and one pair of resistance contacts were present on the Hall-bar. Another way of estimating the magnitude of the gradient is making use of reflection symmetry [11,13]. Reflection symmetry states that the longitudinal resistances measured at both sides of the Hall bar interchange by reversing the polarity of the magnetic field.

$$R^{t}_{xx}(B) = R^{b}_{xx}(-B) \tag{4.4}$$

where *t* and *b* stand for top and bottom respectively. So having only one pair of resistance contacts but measuring for reversed field also, gives us the data for the opposite pair of resistance contacts. It is shown that the longitudinal resistances at the top and bottom of the Hall bar are given by [13]

$$R^{t}_{xx} = \frac{V^{t}_{xx}}{I_x} = \frac{L}{W}(\rho_0 + \alpha\frac{W}{2}) \tag{4.5}$$

and

$$R^{b}_{xx} = \frac{V^{b}_{xx}}{I_x} = \frac{L}{W}(\rho_0 - \alpha\frac{W}{2}) \tag{4.6}$$

where

$$\alpha = \frac{\partial\rho_H}{\partial\nu}\frac{\partial\nu}{\partial x} \tag{4.7}$$

From Eq. (4.2) and (4.3) it follows that

$$R^{t}{}_{xx}(B) - R^{t}{}_{xx}(-B) = \alpha L \tag{4.8}$$

Combining Eq. (4.4) and (4.5) gives

$$R^{t}{}_{xx}(B) - R^{t}{}_{xx}(-B) = \frac{\delta\rho_H}{\delta\nu}\frac{\partial\nu}{\partial x}L \tag{4.9}$$

Zero coordinates (*x, y*) are taken at the center of the Hall bar. *Eq*. (4.9) tells us that the difference of R_{xx} for both field polarities is equal to the slope of the Hall resistivity times the gradient along the total length *L* of the Hall bar. ρ_H is the Hall resistivity for the ideal case without gradient. Since we do not know this value, we approximate it by

$$\rho_H = \frac{R_{xy}(B) + R_{xy}(-B)}{2} \tag{4.10}$$

Plotting our data versus the filling factor ν for the PP-transition $2 \longrightarrow 1$ and applying *Eqs*. (4.9) and (4.10) gives us the ΔR_{xx} and $\delta\rho_H/\delta\nu$ curves for $n_e = 1.0$ and 1.3×10^{15} m^{-2} (*Fig*. 4.2) and $n_e = 1.8$ and 2.0×10^{15} m^{-2} (*Fig*. 4.3).

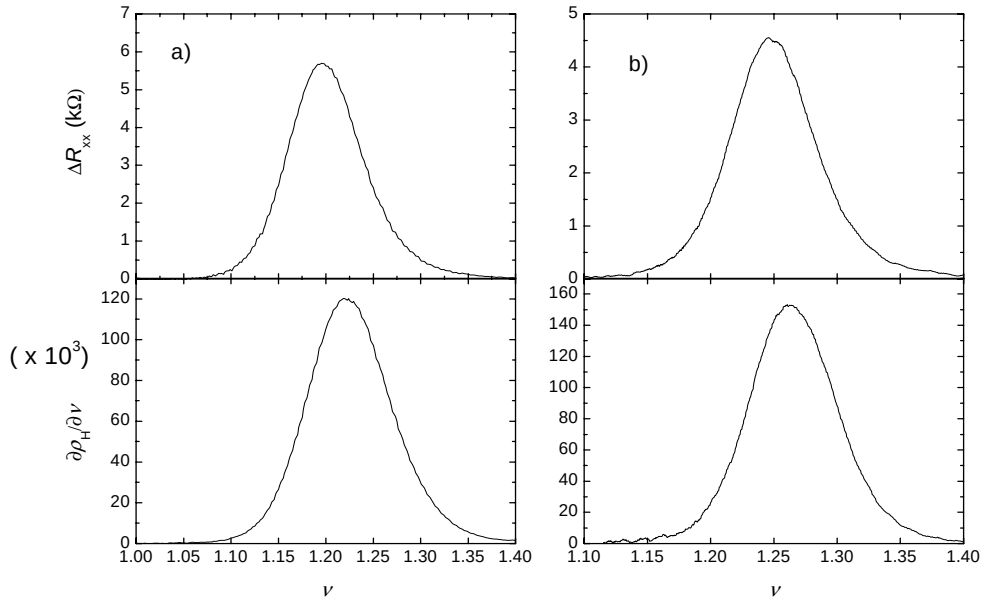

Figure 4.2 ΔR_{xx} for both field polarities (top) and slope of ρ_H versus filling factor (bottom) at $T = 100$ mK for a) $n_e = 1 \times 10^{15}$ m^{-2} and b) $n_e = 1.3 \times 10^{15}$ m^{-2}.

Using *Eq*. 4.9 the ratio of peak values (top/bottom) gives us approximately a gradient of 4.7 % for the lowest density. Also interesting is to look at the shift of the lower curve with respect to the upper curve. In doing so we assume that the Hall transition occurs at a local filling factor, while the R_{xx} transition occurs at some sort of averaged filling factor over the whole Hall bar. Twice this shift should give an approximate value for the gradient. In this case using $2 \cdot \Delta\nu/\nu$ also results in a gradient of 4.7 %.

In *Table* 4.1 the same results for the other densities are shown. Notice how close the results of both methods are. From this it follows that the Hall bar is the most homogeneous at $n_e = 1.8 \times 10^{15}$ m^{-2}.

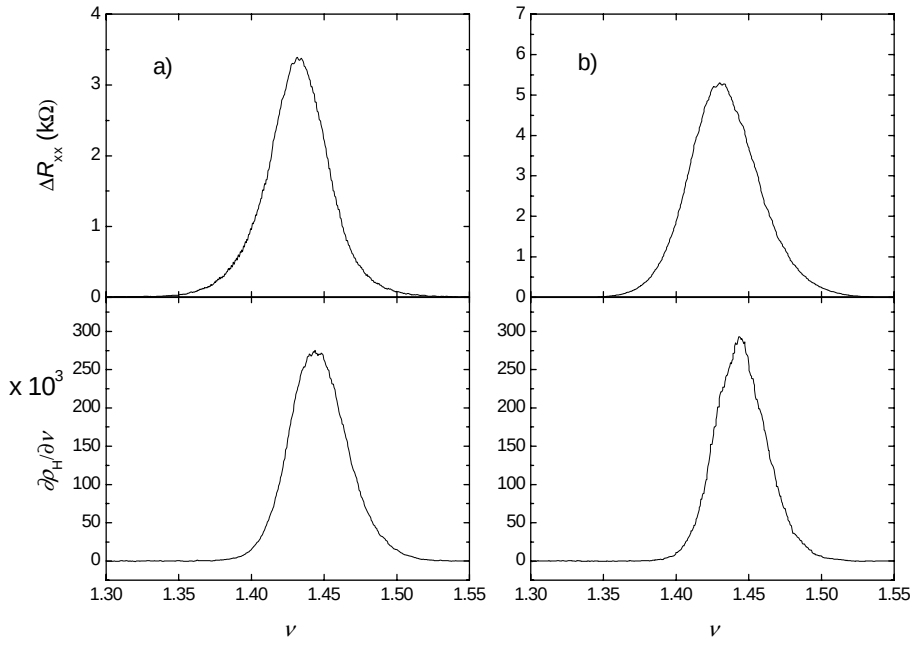

Figure 4.3 ΔR_{xx} for both field polarities (top) and slope of ρ_H (bottom) versus filling factor at $T = 100$ mK for a) $n_e = 1.8 \times 10^{15}$ m^{-2} and b) $n_e = 2.0 \times 10^{15}$ m^{-2}.

The density gradients obtained from the analysis in *Figs*. 4.2 and 4.3 for the different densities are listed in *Table* 4.1.

Table 4.1 Density gradients for the four different densities

n_e (m^{-2})	Gradient (%) reflection symmetry	Gradient (%) shift between ΔR_{xx} and $\delta\rho_H/\delta\nu$ curves
1.0×10^{15}	4.7	4.7
1.3×10^{15}	3.0	2.4
1.8×10^{15}	1.4	1.7
2.0×10^{15}	1.8	1.8

Another way of estimating the gradient is by simulating the PP-transition numerically [11]. Since a gradient causes a difference between the R_{xx}^t and R_{xx}^b curve, we can simulate a transition using the parameters obtained from the experiment (T_0, κ) and vary the gradient

until we get a result similar to the experimentally obtained curves. The measured PP transitions for the four different densities are presented in *Fig*. 4.4. Simulations using the equations shown in [21] are presented in *Fig*. 4.5. The gradients here are 2.5 % and 5 %. More about simulations will be discussed in section 4.4.

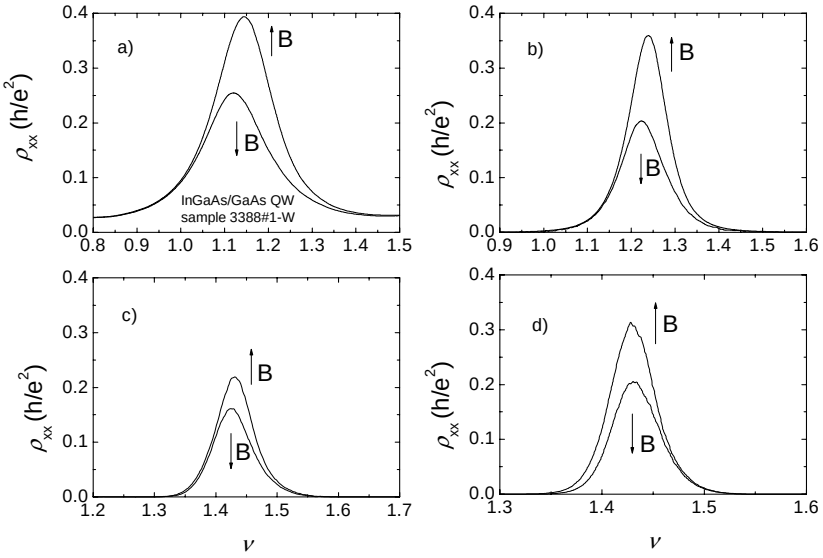

Figure 4.4 ρ_{xx} at the PP transition 2 → 1 for positive and negative field for a) $n_e = 1.0 \times 10^{15}$ m^{-2}, b) $n_e = 1.3 \times 10^{15}$ m^{-2}, c) $n_e = 1.8 \times 10^{15}$ m^{-2} and d) $n_e = 2.0 \times 10^{15}$ m^{-2}. T = 100 mK.

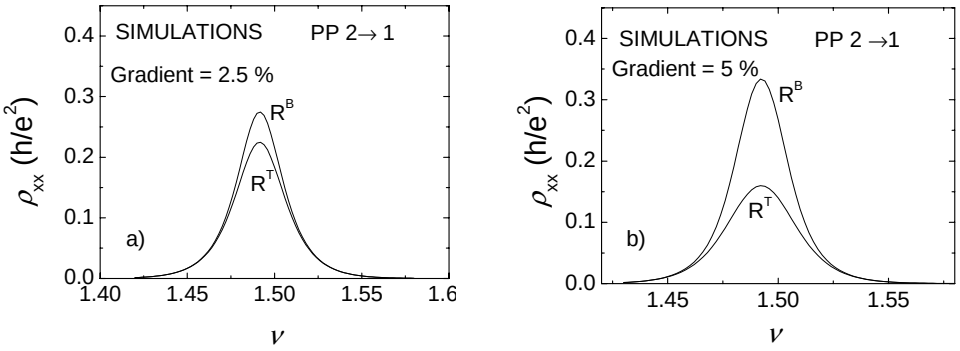

Figure 4.5 Numerical simulation of ρ_{xx} at the PP transition 2 → 1 for a) 2.5 % and b) 5 %.

First of all it should be noticed that in both the simulated curves and the measured data the transition does not occur at the theoretically expected filling factor of 1.5. The higher the gradient, the more the actual critical filling factor deviates. This deviation however, is much smaller for the simulated cases than for the measured ones, for comparable gradients. For example if we consider $n_e = 1.8 \times 10^{15}$ m^{-2}, where the density gradient according to reflection symmetry is 1.4 %, the critical filling factor is shifted to 1.43, whereas in the simulated case (2.5 %) it is only shifted to 1.49. Now consider the ratio of the maximum peak values for the different densities as shown in *Table* 4.2.

Table 4.2 Ratio of maximum peak values of $R_{xx,max}$ (B↑) /$R_{xx.max}$ (B↓) for the four measured densities and the two simulated gradients.

n_e (m^{-2})	$R_{xx,max}$ (B↑) /$R_{xx.max}$ (B↓)	Gradient (%) (simulated)	$R_{xx,max}$ (B↑) /$R_{xx.max}$ (B↓)
1.0×10^{15}	1.6	2.5	1.2
1.3×10^{15}	1.8	5	2.0
1.8×10^{15}	1.4		
2.0×10^{15}	1.6		

The ratio $R_{xx,max}$ (B↑) /$R_{xx.max}$ (B↓) follows the same trend as seen in the previously discussed methods, being the lowest for the third density and then increasing slightly for the highest density. From *Table* 4.2 we can conclude that there is a correspondence between simulations and experiment. Summarizing we can say that we have approximated the inhomogeneous nature of the 2DEG by a density gradient along the current direction of the Hall bar and that we have tried to determine this gradient in three different ways from the PP-transition: From reflection symmetry, from the shift in filling factor between the transitions of the Hall and longitudinal resistance and by making use of numerical simulations. The answers obtained from all three methods correspond with each other.

4.3 The PI-transition

In the previous paragraph we showed curves of magnetotransport data taken on the 2DEG before it reached the insulating state. This has been done only for the lowest temperature measured (100 mK). We did not consider any temperature dependence of the slope of the plateau-plateau transitions of ρ_H or the width of the peaks of the longitudinal resistance,

since in the past it turned out that these transitions are not suited for investigating critical behavior. The universal critical behavior is too much affected by sample dependent aspects like inhomogeneities in the electron density of the 2DEG. It has also been shown that for the PI-transition it is possible to disentangle the universal critical behavior from sample dependent aspects [11,12]. In this section we will examine the PI transition for all four measured densities. The resistivity near the critical filling factor ν_c follows the empirical law [11,15,20]:

$$\ln(\rho_{xx}/\rho_{xx,c}) = -\Delta\nu/\nu_0(T) \tag{4.11}$$

where:

$$\nu_0(T) = (T/T_0)^{\kappa} \tag{4.12}$$

Figs. 4.6 and 4.7 show the longitudinal resistance near the PI transition on a semi-log plot, both as a function of the filling factor and the magnetic field for $n_e = 1.8$ and 2.0×10^{15} m^{-2}. By plotting the resistivity in this way we can directly extract $\nu_0(T)$ from the slope of the curves near ν_c.

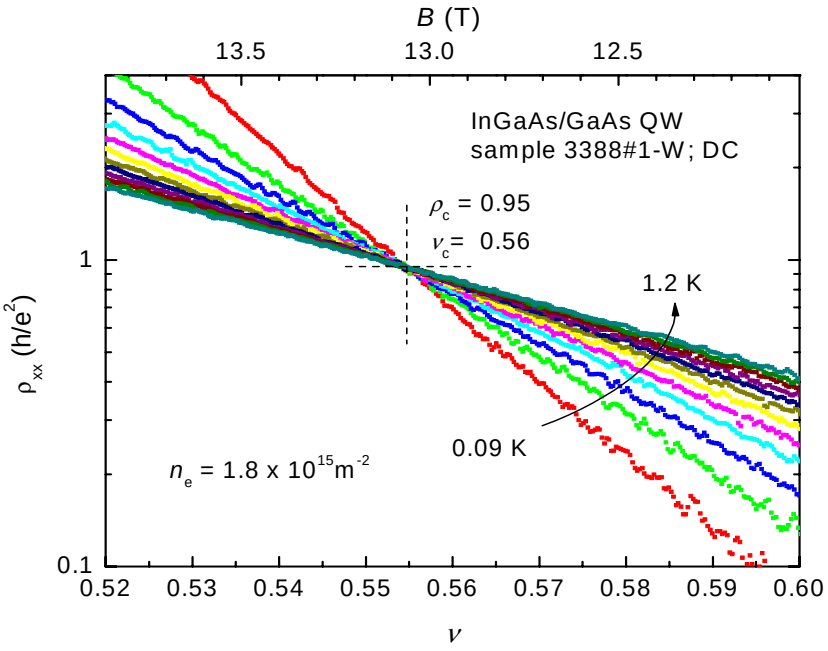

Figure 4.6 The longitudinal resistance in the regime of the PI transition for twelve different temperatures: 0.09, 0.2, 0.3, 0.4, 0.5, 0.6, 0.7, 0.8, 0.9, 1.0, 1.1 and 1.2 K as a function of filling factor (lower axis) and magnetic field (upper axis). The crossing point indicates the location of the PI-transition. The electron density is 1.8×10^{15} m^{-2}. $I = 10$ nA.

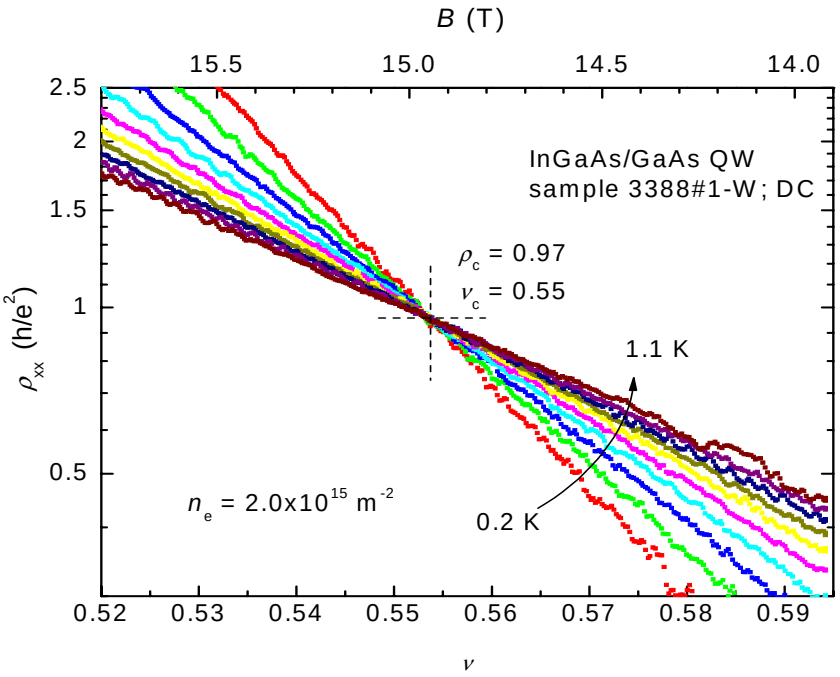

Figure 4.7 The longitudinal resistance in the regime of the PI-transition for ten different temperatures: 0.2, 0.3, 0.4, 0.5, 0.6, 0.7, 0.8, 0.9, 1.0, and 1.1 K as a function of filling factor (lower axis) and magnetic field (upper axis). The crossing point indicates the location of the PI-transition. The electron density is 2.0×10^{15} m^{-2}, $I = 10$ nA.

Data for the lowest two measured densities (1.0 and 1.3×10^{15} m^{-2}) are not shown. The value of $\rho_{xx,c}$ deviates up to 6% from the ideal value of h/e^2. This deviation is explained by sample inhomogeneities. Indeed as the density increases and the sample becomes more homogeneous, the value of $\rho_{xx,c}$ shifts towards its ideal value. Plotting the inverse of the slope of the resistivity curves (ν_0) in the vicinity of the PI-transition as function of the temperature on a log-log plot illustrates its critical behavior.

In *Fig*. 4.8 this is shown for four densities. The slopes of the curves are: 0.43 for the lowest two and 0.53 for the highest two densities.

A comparison between the curves that we obtained and the ones obtained by Ponomarenko [11] on Hall-bar 3388#1, with a geometrical factor of 5.2 is shown in *Fig*. 4.9. The values of ν_0 coincide better for the highest density.

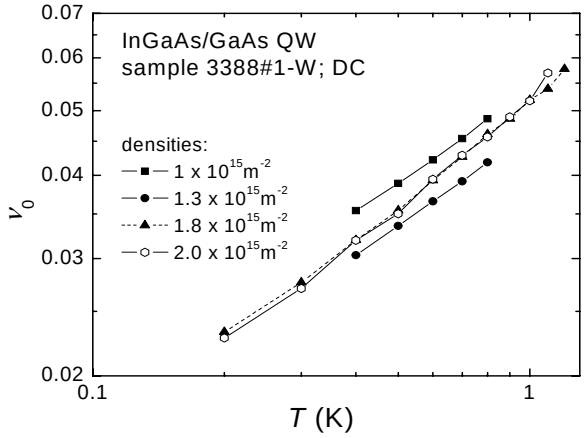

Figure 4.8 Temperature dependence of ν_0 for four different electron densities.

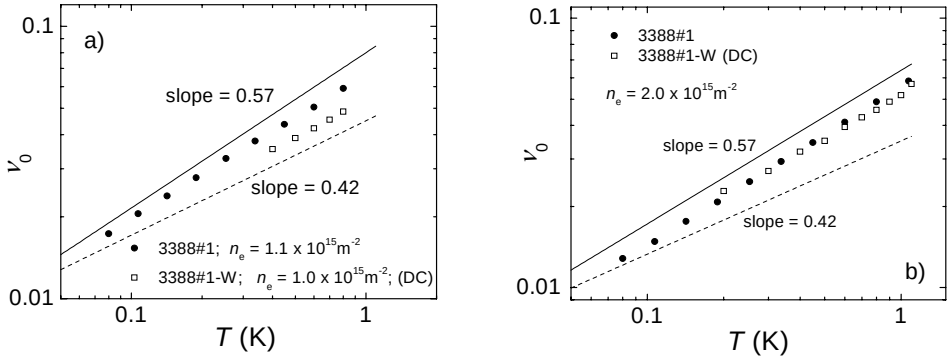

Figure 4.9 Comparison of the Temperature variation of ν_0 for sample 3388#1-W and 3388#1 [2], a) for $n_e \approx 1.0 \times 10^{15}$ m^{-2}, b) for $n_e = 2.0 \times 10^{15}$ m^{-2}. The straight lines representing slopes of 0.57 and 0.42 are given as a guide to the eye only.

4.4 Simulating the PI-transition

Hall-bars in practice turn out to be non-ideal. This means that in an attempt to measure universal properties, like critical exponents, there will always be some unwanted influences of sample-dependent (and thus non-universal) aspects. As discussed in section 4.2 one of the main disturbing factors in probing critical behavior are so called macroscopic sample inhomogeneities. In the simplest approach the inhomogeneity is a density gradient in the length direction of the Hall-bar. Making use of numerical simulations we are able to determine the influences of these inhomogeneities on the measured critical behavior. For the simulations we used software written by L.A. Ponomarenko [11], which allows

simulating a gradient in the electron density of the 2DEG. The gradient can be defined both in the direction parallel to the current flow (along the Hall bar) or perpendicular to the current flow. The Hall bar used in the simulations can be represented as follows:

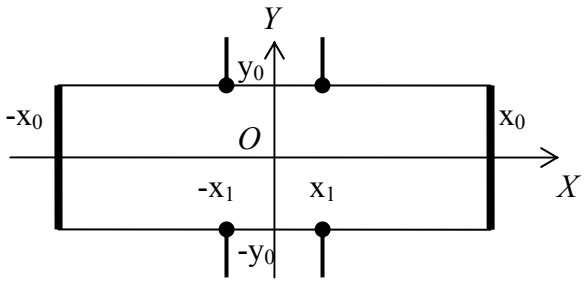

Figure 4.10 Representation of Hall bar used in numerical simulations.

The dimensions taken for the Hall bar are based on realistic ones. For the ratio between length, width and distance between the pair of Hall contacts we used 17:2:3. The simulations were done starting for zero gradient and then increasing the gradient between the Hall contact pairs in the x-direction up to 30%. The results are shown in *Figs*. 4.11a-c, where the behavior of ρ_{xx} is plotted near the PI transition for increasing gradient in the electron density. With increasing gradient the crossing point of the resistivity curves becomes less well defined. It spreads out due to shifting of the low temperature curves. The same is observed experimentally. The slope determined from the log-log plots on the right side starts to deviate from the 'zero-gradient' value of 0.58 with increasing gradient. This deviation however starts after a relatively high value of the gradient (>10%). As shown before [11], it confirms that the PI-transition is much less sensitive for density gradient than the PP-transitions. If the gradient exceeds a certain limit, also the resistivity values near the PI-transition are distorted.

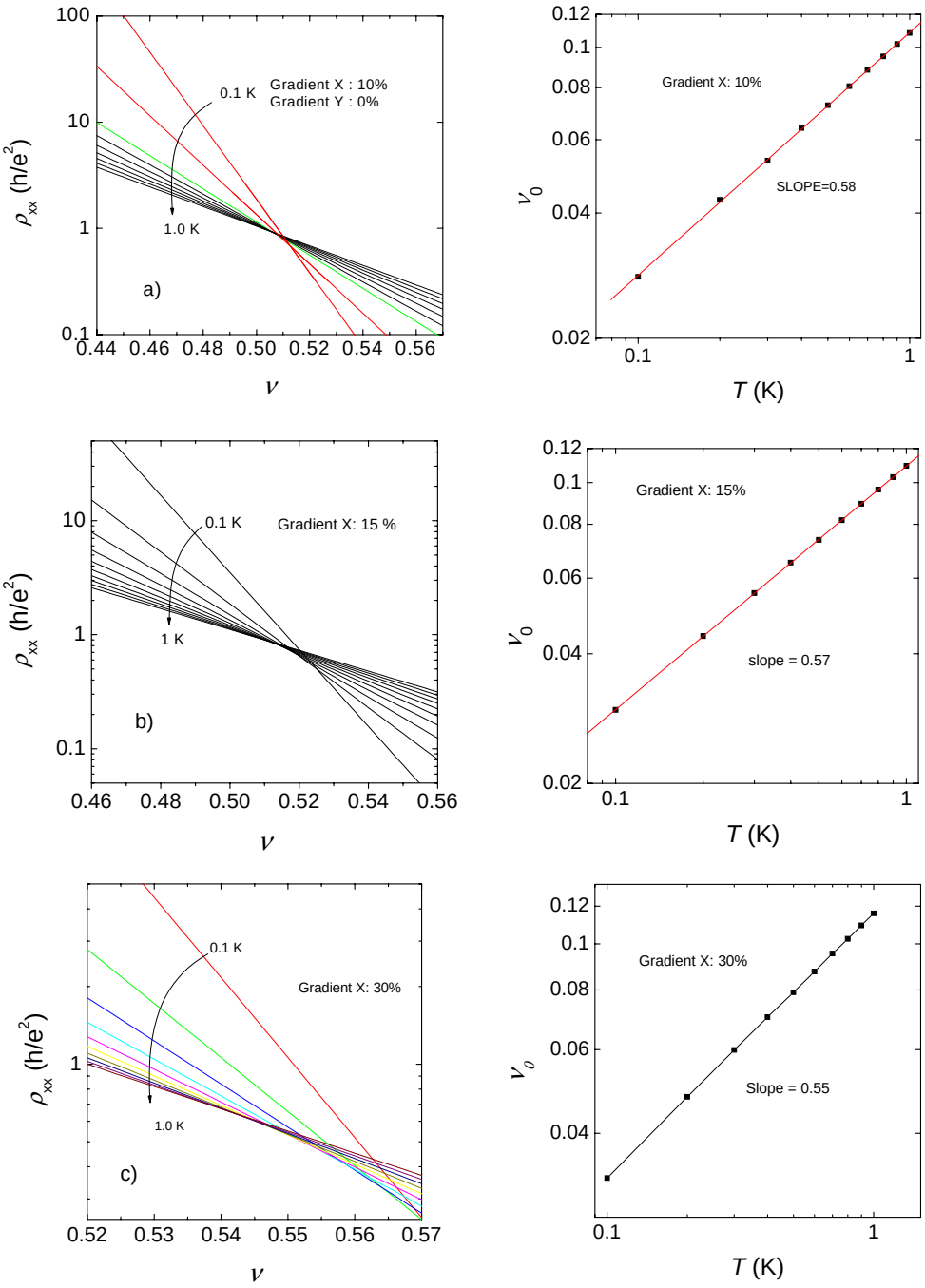

Figure 4.11 Results of numerical simulations a) 10 % gradient in x-direction b) 10 % in x-direction and c) 30 % gradient in the x-direction.

4.5 Conclusions

- Magnetotransport measurements have been carried out on an InGaAs/GaAs QW at four different electron densities tuned by illumination in the range 1.0-2.0×10^{15} m^{-2} in order to study the 2→1 PP and PI transitions.
- The density gradient in the Hall bar was determined from the 2→1 PP transition by the method of "reflection symmetry". The gradient ranges from 1.4 to 4.7 % for the investigated densities.
- The effect of the density gradient on the magnetotransport data was investigated by numerical simulations for the 2→1 PP and PI transition. The results are in good agreement with those observed in the experimental data.
- Scaling of the PI transition was investigated by extracting the temperature variation of ν_0 from the longitudinal resistance data. The critical exponent κ falls in the range 0.43-0.53. The latter value is slightly lower than the value $\kappa = 0.57$ obtain previously [11] on a narrower Hall bar prepared from the same InGaAs/GaAs wafer.

4.6 References

[1] K. von Klitzing, G. Dorda and M. Pepper, *Phys. Rev. Lett.* **45** (1980) 494.

[2a] H.P. Wei, D.C. Tsui, M.A. Paalanen and A.M.M. Pruisken, *Phys. Rev. Lett.* **61** (1988) 1294.

[2b] A.M.M. Pruisken, *Phys. Rev. Lett*. **61** (1988) 1297.

[3] H.P. Wei, D.C. Tsui and A.M.M. Pruisken, *Phys. Rev. B* **33** (1985) 1488.

[4] S. Koch, R.J. Haug, K. von Klitzing and K. Ploog, *Phys. Rev. Lett.* **43** (1991) 6828.

[5] R.B. Dunford, N. Griffin, M. Pepper, P.J. Phillips and T.E. Whall, *Physica E* **6** (2000) 297.

[6] J. Wakabayashi, A. Fukano, S. Kawaji, Y. Koike and T. Fukase, *Surf. Science* **229** (1990) 60.

[7] K.H. Yoo, H.C. Kwon and J.C. Park, *Solid State Commun.* **92** (1994) 821.

[8] D. Shahar, D.C. Tsui, M. Shayegan, J.E. Cunningham, E. Shimshoni and S.L. Sondhi, *Solid State Commun.* **102** (1997) 817.

[9] A.M.M. Pruisken, B. Skoric and M. Baranov, *Phys. Rev. B* **60** (1999) 16838.

[10] H.P. Wei, S.Y. Lin and D.C. Tsui, *Phys. Rev. B* **45** (1992) 3926.

[11] L.A. Ponomarenko, *Ph.D Thesis* (University of Amsterdam, 2005), unpublished.

[12] B. Karmakar, M.R. Gokhale, A.P. Shah, B.M. Arora, D.T.N. de Lang, A. de Visser, L.A. Ponomarenko and A.M.M. Pruisken, *Physica E* **24** (2004) 187.

[13] L. A. Ponomarenko, D.T.N. de Lang, A. de Visser, V.A. Kulbachinskii, G.B. Galiev, H. Künzel and A.M.M. Pruisken, *Solid State Commun.* **130** (2004) 705.

[14] D.T.N. de Lang, *Ph.D Thesis* (University of Amsterdam, 2005), unpublished.

[15] A.M.M. Pruisken, D.T.N. de Lang, L.A. Ponomarenko and A. de Visser, *Solid State Commun.* **137** (2006) 540.

[16] A. de Visser, L.A. Ponomarenko, G. Galistu, D.T.N. de Lang, A.M.M. Pruisken, U. Zeitler and D. Maude, *J.Phys. Conf. Series* (2006) Sendai.

[17] Wanli Li, G.A. Csathy, D.C. Tsui, L.N. Pfeiffer and K.W. West, *Phys. Rev. Lett*. **94** (2005) 206807.

[18] Wanli Li, G.A. Csathy, D.C. Tsui, L.N. Pfeiffer and K.W. West, *Int. Journal of Modern Physics B* **18** (2004) 3569.

[19] Wanli Li, C.L. Vicente, J.S. Xia, W. Pan, D.C. Tsui, L.N. Pfeiffer and K.W. West, *Phys. Rev. Lett*. **102** (2009) 216801.

[20] D.T.N. de Lang, L.A. Ponomarenko, A. de Visser and A.M.M. Pruisken, *Phys. Rev. B* **75** (2007) 1.

[21] J. Oswald, G. Span and F. Kuchar, *Phys. Rev. B* 58 (1998) 15401.

5. Irrelevant critical behavior

5.1 Introduction

Having discussed the relevant critical behavior in *Chap.* 4, we here focus on the irrelevant critical behavior and its irrelevant critical exponent. The meaning of the irrelevant critical behavior within the context of the scaling theory for the QHE is elaborated in *Chap*. 2. The experimental manifestation of this phenomenon will be discussed in this chapter. The deviations from quantization that we would like to determine in order to probe irrelevant critical behavior are of the order of a few percent of the quantized value h/e^2 of the $\nu = 1$ plateau [1,2,3]. For a perfect homogeneous sample these should be easily detectable using the appropriate measuring equipment. A discussion of the method used for these experiments is found in *Chap*. 3 of this thesis. However macroscopic sample inhomogeneities like gradients and especially contact misalignment thwart the proper observation of the deviations from quantization [1]. In this chapter we will discuss the most common ways to deal with these sample imperfections. Next we will show the measured deviations from quantization obtained with the DC method for three electron densities on sample 3388#1-W (n_e = 1.3, 1.8 and 2.0 x10^{15} m^{-2}). Then we report the analysis that has been performed on the data to extract the irrelevant critical behavior and the corresponding critical exponents. The analysis consists mainly of collapsing different data-sets (each data-set belonging to a different filling factor) onto one single curve, of which the general shape follows from the expected power-law behavior. It turns out that after applying a temperature dependent shift in filling factor of the measured curves the data-collapse improves. Finally we present the flow diagram calculated for the PI transition measured on the 2DEG for n_e = 1.8 x 10^{15} m^{-2}. This diagram is compared with experimentally obtained flow lines [5]. The evolution of our understanding of the flow diagram will briefly be elaborated.

5.2 Dealing with sample inhomogeneities and contact misalignment

The core of our task is to probe critical behavior in the quantum Hall regime, or more specifically: irrelevant quantum critical behavior in the Hall resistivity nearby the PI-transition. As a more ambitious task we also want to show that this quantum critical behavior is universally valid, meaning that it is sample independent and is obeyed by all 2DEGs, as long as the sample related criteria for scaling are satisfied. In order to proof universality there are different routes: One may take several suitable samples, possibly made out of different semiconductor materials, and carry out measurements on all of them. One may also take a sample in which the carrier density is tunable. In this case reaching a higher density by illuminating the 2DEG with infra-red light at low temperatures creates a situation which is equivalent to a different sample. The lack of availability of samples and that fact that not all available samples are suitable has limited us to the second option. Therefore, all the measurements described in this chapter were performed on an InGaAs/GaAs Quantum Well with tunable carrier density. An image of this sample is shown in *Fig*. 3.11 of chapter three. Unfortunately most samples are non-ideal 2-DEGs because of macroscopic sample inhomogeneities. This means that the electron density throughout the 2DEG is not constant, but varies with place. If we consider the expression for the B_c-values where the transitions occur, were ν is the filling factor, e is the electron charge and n_e is the electron density,

$$B_c = \frac{h \cdot n_e}{e \cdot \nu} \tag{5.1}$$

it is clear that an electron density that is not constant throughout the 2DEG will have drastic consequences. As result of this the same transition will occur for different values of the magnetic field in different parts of the 2DEG. So instead of one filling factor for the whole 2DEG, we have to deal with a local filling factor: $\nu(\mathrm{r}) = \nu_0 + \nu_x \times x + \nu_y \times y$. This results from an asymmetric growing technique of the semiconductor structure and an inhomogeneous freezing in of the impurities responsible for the disorder potential upon cooling down. An extended study on sample inhomogeneities can be found in *Refs*. [1,4]. Another sample imperfection we have to deal with is the so called contact misalignment. Due to microscopic differences in the electron-density nearby two geometrically perfectly opposing contacts, these contacts effectively are slightly misaligned. The main consequence of this is an admixture of resistivity components. It has been shown that there

are several ways to take care of sample inhomogeneities and contact misalignment [1-4]. These different ways and why a specific way has our preference in the case described here will be briefly discussed next. The first way to deal with these sample imperfections is the stretch-tensor formalism developed by Pruisken [3,4]. According to this an ideal Hall bar geometry can be represented as a rectangular shape with sides $L \times W$ and a homogeneous distribution of carrier density 'n_e'. A non-ideal Hall bar, that is a Hall bar with contact misalignment and macroscopic inhomogeneities can be mapped onto the same rectangular shape where the y-axis is tilted by an angle θ and where the electron density is spatially dependent: $n_e\ (x, y)$, i.e stretched out. See *Fig*. 5.1.

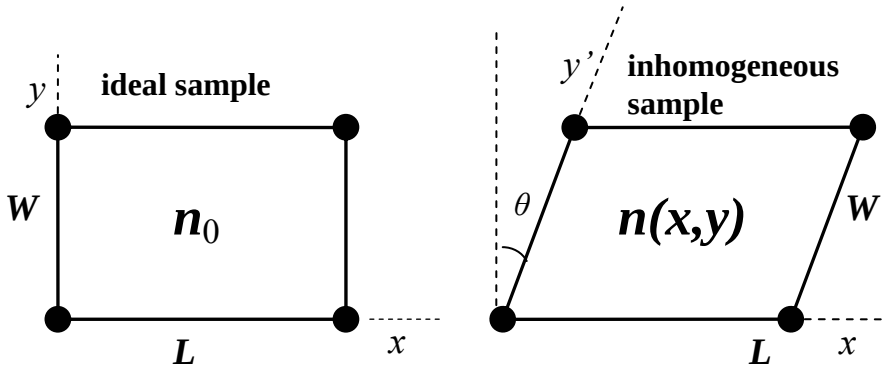

Figure 5.1 Schematic representation of the stretch tensor 'S_{ij}' Left an ideal sample with sides $L \times W$ and a homogeneous distribution of carrier density n_e. Right an inhomogeneous sample with a spatially dependent electron density n_e (x,y) and contact misalignment that can be represented by the angle θ.

It has been shown that any pair of components ρ_{xx}, ρ_{xy} measured on a non ideal sample, can be expressed in the following way [4]:

$$\rho_{ij} = S_{ij}\rho_0 + \varepsilon_{ij}\rho_H^{(0)} + S_{ij}'\rho_H^{(1)} \tag{5.2}$$

where ρ_H and ρ_0 are the intrinsic transport coefficients. $\rho_H^{(0)}$ and $\rho_H^{(1)}$ are both odd under a change of the polarity in B:

$$\rho_H^{(0)}(B) = -\rho_H^{(0)}(-B)$$
$$\rho_H^{(1)}(B) = -\rho_H^{(1)}(-B) \tag{5.3}$$

The intrinsic transport coefficients as a function of $X = (T/T_0)^{-\kappa}$ are:

$$\rho_0(X) = e^{-X+O(X^3)}$$

$$\rho_H(X,\eta) = \rho_H^{(0)} + \rho_H^{(1)}(X,\eta) \tag{5.4}$$

with $$\rho_H^{(0)} = 1, \qquad \rho_H^{(1)}(X,\eta) = \eta(T)\rho_0(X) \tag{5.5}$$

The effects of sample inhomogeneities (density gradients and contact misalignment) are all contained in:

$$S_{ij} = \frac{1}{\cos\theta}\begin{bmatrix} \rho_c & \sin\theta \cdot e^{\frac{\delta\nu_x}{\nu_0(T)}} \\ -\sin\theta \cdot e^{-\frac{\delta\nu_y}{\nu_0(T)}} & \rho_c^{-1} \end{bmatrix} \tag{5.6}$$

$$S_{ij}' = \frac{1}{\cos\theta}\begin{bmatrix} 0 & \sin\theta \cdot e^{\frac{\delta\nu_x}{\nu_0(T)}} \\ -\sin\theta \cdot e^{-\frac{\delta\nu_y}{\nu_0(T)}} & 0 \end{bmatrix} \tag{5.7}$$

Now consider that the ρ_{xy} data for constant T can be split in a symmetric and an antisymmetric part

$$\rho_{xy}(B) = \rho_H(B) + \rho_{xy}^s \tag{5.8}$$

in which ρ_{xy}^s is only an admixture of the R_{xx} component. The ρ_{xy}^s data is taken from a different part of the sample than the R_{xx} data, which is like a global average of the sample resistance. In case of macroscopic sample inhomogeneities there will be a noticeable difference between the critical fixed point ν_c obtained from the R_{xx} data, and $\tilde{\nu}_c$ obtained from the ρ_{xy}^s data (from now on all the parameters obtained from the ρ_{xy}^s data will be shown with a tilde). If we assume a spatially dependent filling factor $\nu(r) = \nu_0 + \nu_x x + \nu_y y$, than the stretch tensor S_{ij} is given by

$$S_{ij} = \frac{1}{\cos\theta}\begin{bmatrix} 1 & \sin\theta \cdot e^{\frac{\varepsilon_x \nu}{\nu_0(T)}} \\ -\sin\theta \cdot e^{-\frac{\varepsilon_y \nu}{\nu_0(T)}} & 1 \end{bmatrix} \tag{5.9}$$

where $\varepsilon_x = \pm\nu_x \frac{L}{2\nu}$ and $\varepsilon_y = \pm\nu_y \frac{W}{2\nu}$. These are taken as fixed quantities representing the relative uncertainties in the electron density in the *x* and *y* directions. From *Eqs.* (5.6), (5.7) and (5.8) it follows that

$$\rho_{xy}^{S}(B,T) = \tan\theta \cdot e^{\frac{\varepsilon_x \nu}{\nu_0(T)}} \rho_0(X) = \tan\theta \cdot \rho_0(\widetilde{X}) \tag{5.10}$$

where $\widetilde{X}$ is the local scaling variable

$$\widetilde{X} = \frac{\nu - \widetilde{\nu}_c}{\widetilde{\nu}_0(T)} \tag{5.11}$$

and

$$\widetilde{\nu}_c = \frac{\nu_c}{1+\varepsilon_x} \tag{5.12}$$

$$\widetilde{T}_0 = T_0(1+\varepsilon_x)^{1/\kappa} \tag{5.13}$$

are the local equivalents of ν_c and T_0 when there is only a measurable gradient in the *x*-direction. ε_x can be determined from the experimental data by using the distance between the local fixed point '$\widetilde{\nu}_c$' and the global fixed point 'ν_c'. A value for tan θ can be obtained by plotting $\frac{\rho_{xy}^{S}}{\rho_0(X)}$ and than fitting with tanθ exp*(X)*. In the abovementioned we have tried to explain how to use the abstract concept of the stretch tensor in order to obtain an idea about the contact misalignment and the density gradient in the Hall bar. Another way to deal with the inhomogeneities is just to extract all the parameters needed for the data analysis from the 'local' situation. Instead of using the ρ_0 data for extracting values like ν_c, κ and T_0 we use the ρ_{xy}^{s} data. We have applied both methods. In the final analysis however we have chosen for the second method. Reason for this is that in this way we can directly extract the 'local behavior' of the 2DEG for the small region of interest to us. We can do this without the concern of how the inhomogeneity profile of the 2DEG really looks like, whether it is a gradient in the *x*-direction, in the *y*-direction, in both directions or maybe something far more complicated. This in contrast to the first method in which we are bound to the assumption that we are dealing with a linear variation in the electron density, and based on this assumption we try to 'reconstruct' the local situation in the region of interest.

5.3 DC results for three electron densities of the 2DEG

In the course of our experiments the magnetotransport data for three electron densities have been examined: 1.3, 1.8 and 2.0 × 10^{15} m^{-2}. First we will elaborate the procedure of data analysis used for the lowest density. Then we will show the results obtained for all three densities. In all the DC measurements described in this chapter the set values for the Delay time and the NPLC's where 350 ms and 15, respectively. The Moving Filter was set to 4 (see *Chap*. 3). This corresponds to a time constant of around 4 seconds and a 'frequency' of around 0.8 Hz. In *Fig*. 5.2 we show the longitudinal resistance near the PI transition in a semi-logarithmic plot:

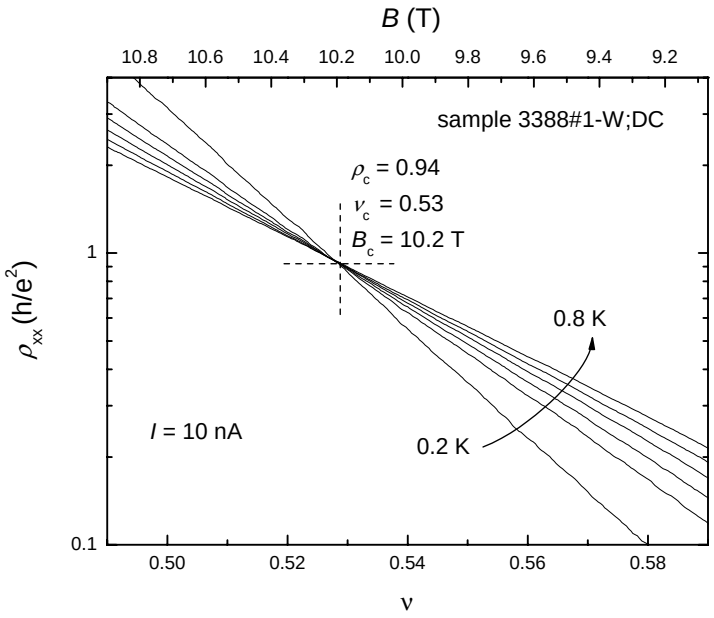

Figure 5.2 PI-transition of sample 3388#1-W for the longitudinal resistivity at six temperatures (T = 0.2, 0.4, 0.5, 0.6, 0.7 and 0.8 K) in a semi-logarithmic plot as a function of filling factor (lower axis) and magnetic field (upper axis); n_e = 1.3x10^{15} m^{-2}. The measurement current was 10 nA.

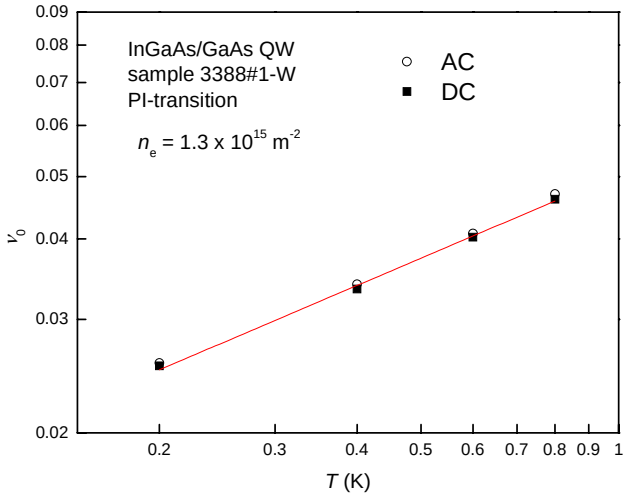

Figure 5.3 Temperature dependence of the parameter ν_0 in a double logarithmic plot of sample 3388#1-W. Both the AC and DC cases are shown.

In *Fig*. 5.3 we show ν_0 as a function of T for both the AC and DC measurements. For this density, fitting the data points with a linear fit gives a similar slope for both the AC and DC method: 0.43. Note that the critical filling factor for the PI transition $\nu_c = 0.53$. This value is higher than the theoretically expected value of $\nu_c = 0.5$. The reason for this is the non-zero overlap between the Landau levels [1]. *Figs*. 5.2 and 5.3 reflect the 'global' behavior of the 2DEG. In fact it should be seen as the average behavior over the whole area of the 2DEG between the resistivity contacts.

Due to inhomogeneities local behavior in a specific region of the 2DEG does not need to be the same as the global behavior. Since we are interested in the critical behavior of the Hall resistivity, our region of interest is the one between two opposite Hall contacts. One way to obtain experimental insight in this local region is provided by one of the sample imperfections: the contact misalignment. Since $\rho_{xy,s}$ is in fact the admixture of the longitudinal resistance component in the Hall component (*Eq*. 5.8), it is possible to do the same analysis on $\rho_{xy,s}$ as we did on ρ_{xx}. *Fig*. 5.4 shows the crossing point of the $\rho_{xy,s}$ data in a semi-log plot for seven temperatures. Note that the critical filling factor is significantly higher than for the ρ_{xx} data: $\nu_c = 0.6$. Also B_c is lower than for the ρ_{xx}- case: $B = 9.8$ T. This

indicates that the electron density between the Hall- contacts is lower than the averaged density over the whole 2DEG. From the $\rho_{xy,s}$ -curves shown in *Fig*. 5.4 we again extract ν_0 and trace ν_0 vs. T in *Fig*. 5.5.

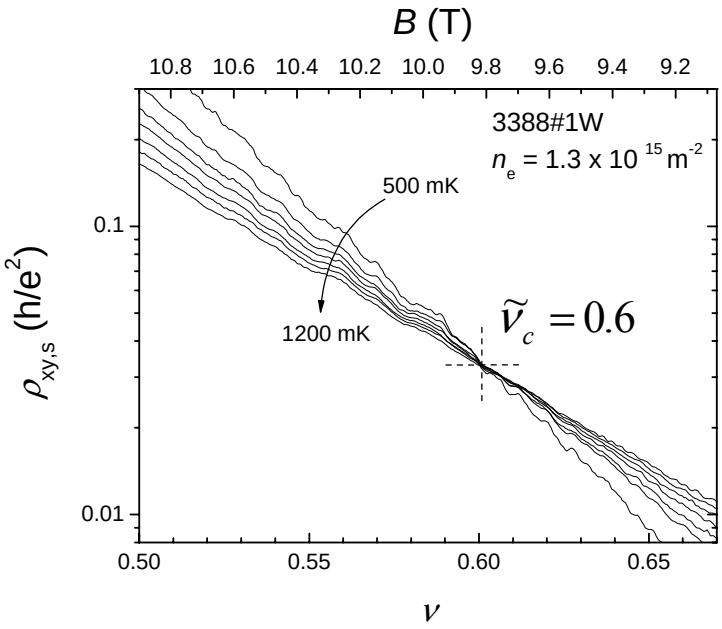

Figure 5.4 PI transition for the longitudinal resistivity component measured at the Hall contacts ($\rho_{xy,s}$) for seven temperatures in a semi-logarithmic plot (T = 0.5, 0.7, 0.8, 0.9, 1.0, 1.1 and 1.2 K) as a function of filling factor (lower axis) and magnetic field (upper axis). The field polarity is positive.

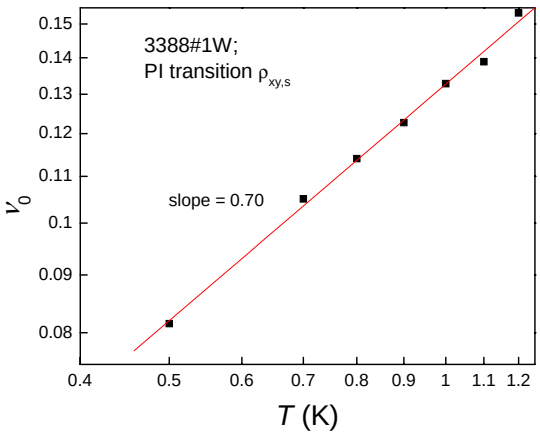

Figure 5.5 ν_0 vs. T for the PI transition of $\rho_{xy,}$

Fig. 5.5 shows that the slope of the temperature dependence of ν_0 for $\rho_{xy,s}$ differs a lot from the one found for the ρ_{xx}-data (*Fig.* 4.8). This illustrates clearly how the local inhomogeneity situation between the Hall contacts can distort critical behavior. The parameter of most interest to us in our further discussion is $\tilde{\nu}_c$, since this is the filling factor at which the PI transition occurs for ρ_H. We recall the scaling functions [2] for the critical behavior of ρ_H at the PI transition:

$$\rho_H = 1 + \eta(T)\rho_0(\tilde{X}), \tag{5.14}$$

with $$\eta(T) = \left(\frac{T}{T_1}\right)^{y_\sigma}; \quad \rho_0(\tilde{X}) = e^{-\tilde{X} - O(\tilde{X}^3)}; \tag{5.15}$$

where $$\tilde{X} = \frac{(\nu - \tilde{\nu}_c)}{\nu_0(T)} \tag{5.16a}$$

and $$\nu_0(T) = \left(\frac{T}{\tilde{T}_0}\right)^{\kappa} \tag{5.16b}$$

In *Fig*. 5.6a we show ρ_H after symmetrizing for both field polarities. Using $\nu = \frac{h \cdot n_e}{e \cdot B}$ and substracting $\tilde{\nu}_c$ we can plot ρ_H versus $\Delta\nu$ (*Fig.* 5.6b). Notice the noisy behavior of the T = 0.5 K curve. This is because the deviation from quantization is the smallest for this temperature, while the diverging of the $\rho_{xy,s}$ for both field polarities is the largest here. This gives a very bad signal to noise ratio.

Eq. 5.15 tells us that the deviation from quantization displays power law behavior. For $\Delta\nu$ = 0 this power law behavior is completely described by the η (T) term. For $\Delta\nu \neq 0$ this power law behavior is the product of η (T) and $\rho_0(\tilde{X})$. The data shown in *Fig*. 5.6b can be plotted in a different way: taking a fixed value for $\Delta\nu$ and plotting the temperature dependence of ρ_H-1 for this value. This is shown in *Fig.* 5.7 for seven values of $\Delta\nu$.

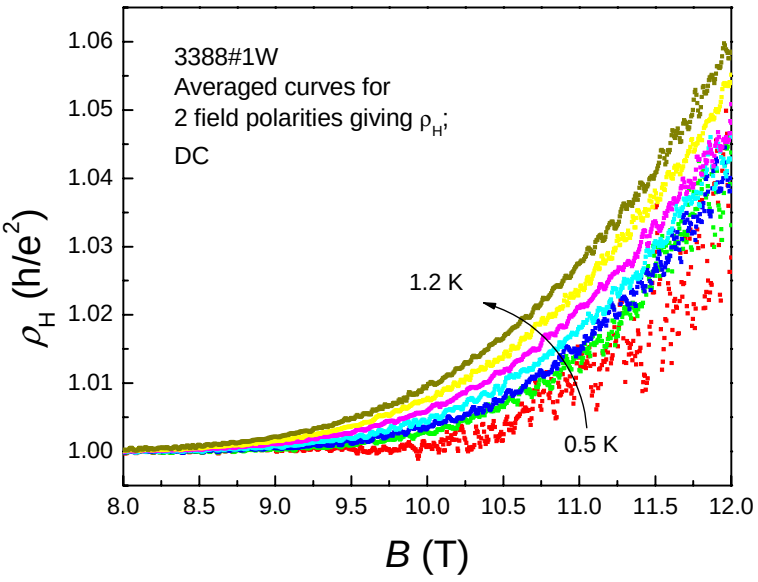

Figure 5.6a Critical behavior of ρ_H at the PI-transition for T = 0.5, 0.7, 0.8, 0.9, 1.0, 1.1 and 1.2 K.

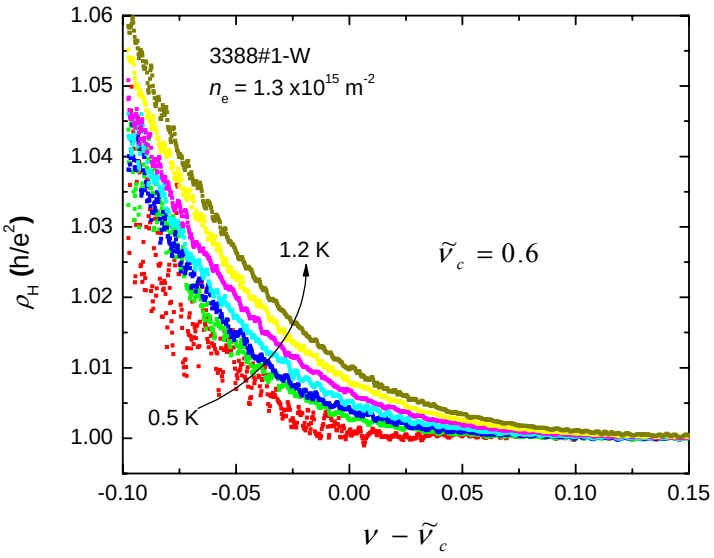

Figure 5.6b ρ_H vs. at T = 0.5, 0.7, 0.8, 0.9, 1.0, 1.1 and 1.2 K.

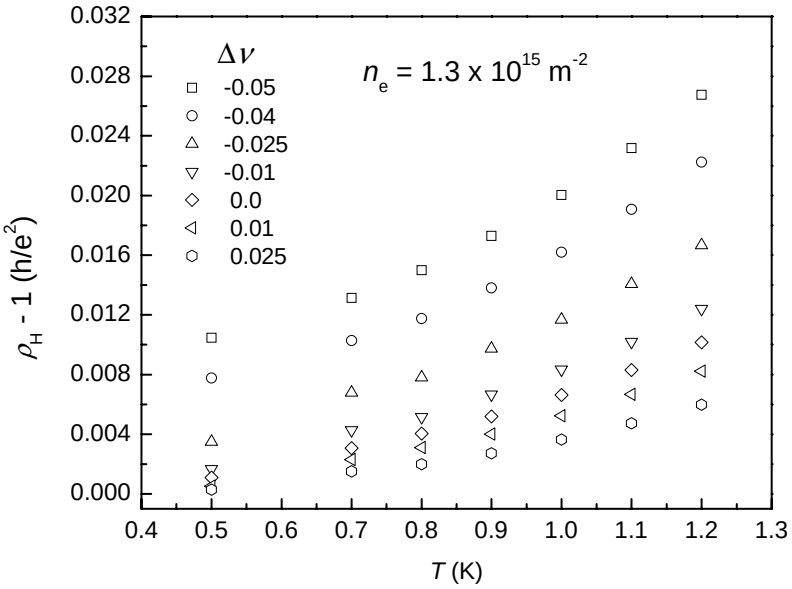

Figure 5.7 ρ_H -1 vs. *T* for seven values of $\Delta\nu$.

From *Eq*. 5.14 it follows that dividing out $\rho_0(\tilde{X})$ from the curves for constant $\Delta\nu$ in *Fig*. 5.7 will give a collapse of the data on $\eta(T)$. The parameters $\tilde{\nu}_c$, and $\tilde{T}_0$ present in $\rho_0(\tilde{X})$ are obtained in the following way: $\tilde{\nu}_c$ follows from the crossing point of the $\rho_{xy,s}$ curves as mentioned above. For $\tilde{T}_0$ and κ the following has been done. The data points in *Fig*. 5.7 can be seen as seven one dimensional (1D) functions $\rho_H(T)$ - 1 for different constant values of $\Delta\nu$. What we can do is map these seven 1D datasets on a 2D data- surface so that a 2D function $\rho_H(T,\Delta\nu)$-1 describes all the data-points. The function used is

$$\rho_H - 1 = \left(\frac{T}{T_1}\right)^{y_\sigma} e^{\frac{-(\Delta\nu-\delta\nu_c)}{(T/T_0)^\kappa}}, \qquad (5.17)$$

where $\delta\nu_c$ is the deviation from $\tilde{\nu}_c$, that can be temperature dependent. The fit is shown in *Fig*. 5.8.

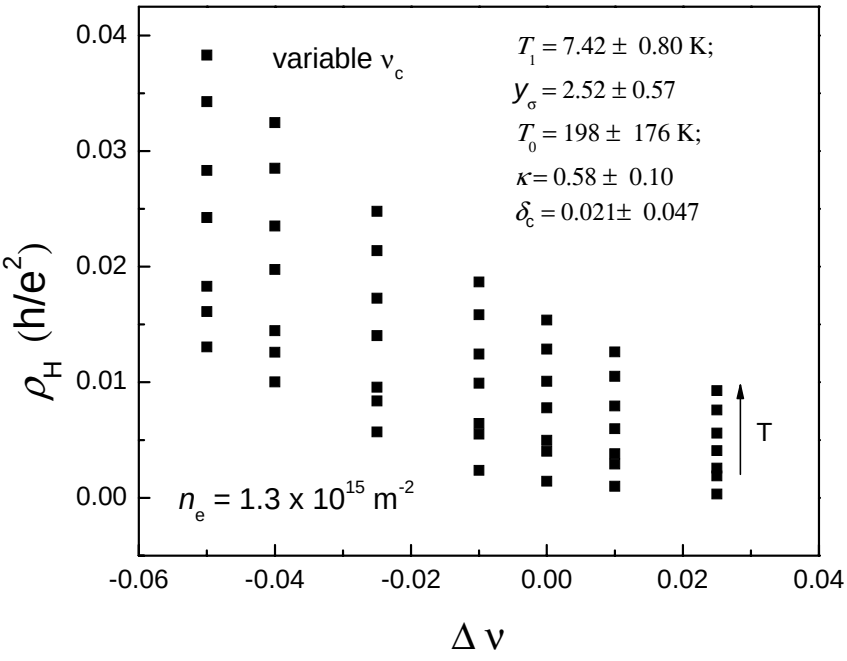

Figure 5.8 two dimensional display of all the data points shown in *Fig*. 5.7 using *Eq*. 5.17.

Important in this method is that we just get one set of the 5 fit parameters. These parameters can be considered an optimum based on all the information contained in the seven 1D datasets mentioned before. Using the values for $\widetilde{T}_0$ and κ we can apply the data collapse on the data sets in *Fig*. 5.7.

The values for T_1 and y_σ found after fitting with $\eta(T)$ are 11.8 K and 1.8 resp. These values are different than the ones mentioned in *Ref*. [1] for the same wafer: 4.5 K for T_1 and 2.6 for y_σ.

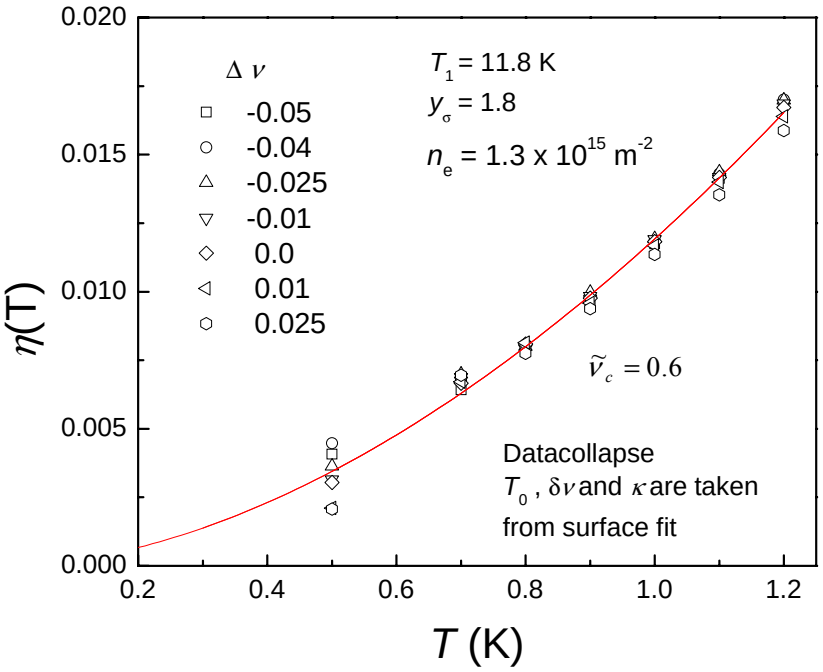

Figure 5.9 Collapse of the ρ_H data (see *Fig.* 5.7) onto a single curve $\eta = (\rho_H - 1)/\rho_o$ ($\widetilde{X}$) vs. T for different values of $\Delta\nu$. T_0, κ and $\delta\nu$ are taken from a 2D fit like in *Fig.* 5.8.

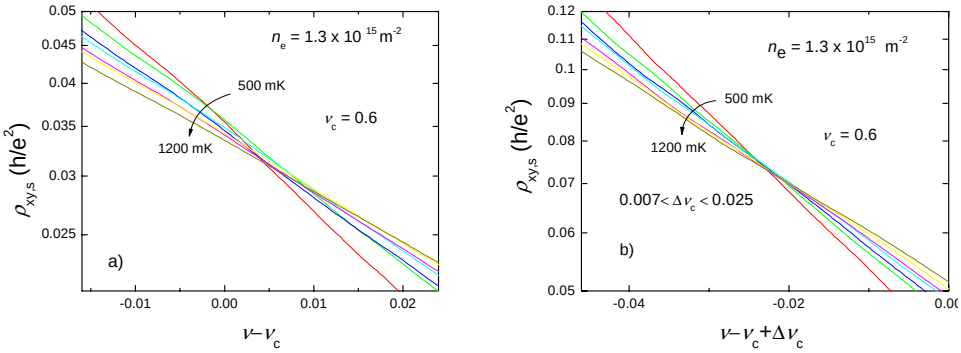

Figure 5.10a) The uncorrected situation for the $\rho_{xy,s}$ data. We can see a poorly defined crossing point and the data show a lack of symmetry around this 'crossing point'. *b*) The corrected situation. The data is smoothed using the 'adjacent averaging' procedure in Origin.

The $\rho_{xy,s}$ data do not show a well defined crossing point as shown in *Fig.* 5.10a. However, this can be obtained by a small temperature dependent shift $0.007 \leq \Delta\nu_c \leq 0.025$ as shown in *Fig.* 5.11b. The shift is the smallest for the highest temperature.

Also the data around the crossing point are now much more symmetric as is required by the condition of particle-hole symmetry [2]

$$\rho_0(X) = \rho_0^{-1}(-X) \tag{5.18}$$

Repeating the procedure described above using the shifted curves of ρ_H gives the data collapse shown in *Fig.* 5.11.

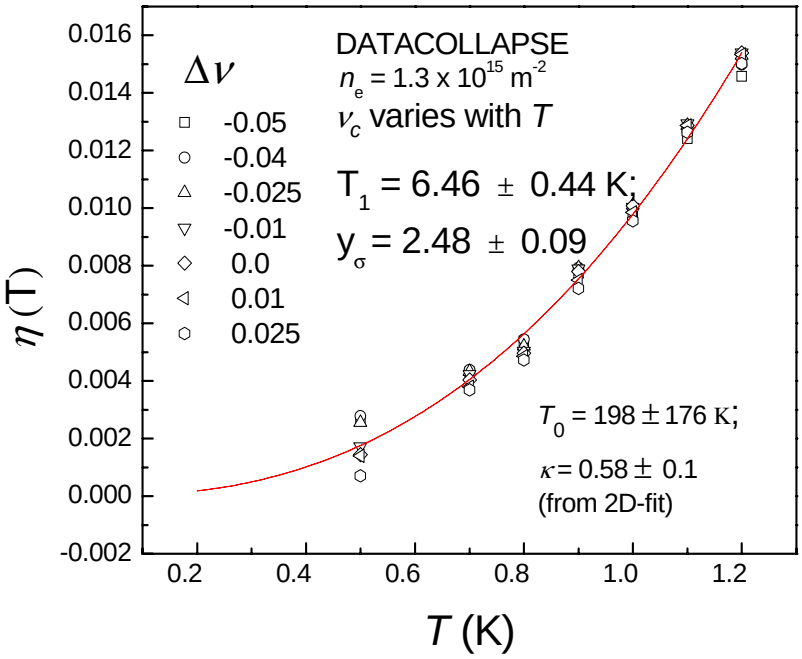

Figure 5.11 Collapse of the ρ_H data (see *Fig.* 5.7) onto a single curve $\eta = (\rho_H - 1)/\rho_o$ ($\tilde{X}$) vs. T for different values of $\Delta\nu$. T_0, κ and $\delta\nu$ are taken from a 2D fit like in *Fig.* 5.8. The original curves of ρ_H have been given a temperature dependent shift. $n_e = 1.3 \times 10^{15}$ m^{-2}.

For the other two densities the results are shown on the next pages. We will limit ourselves here to show the final results only.

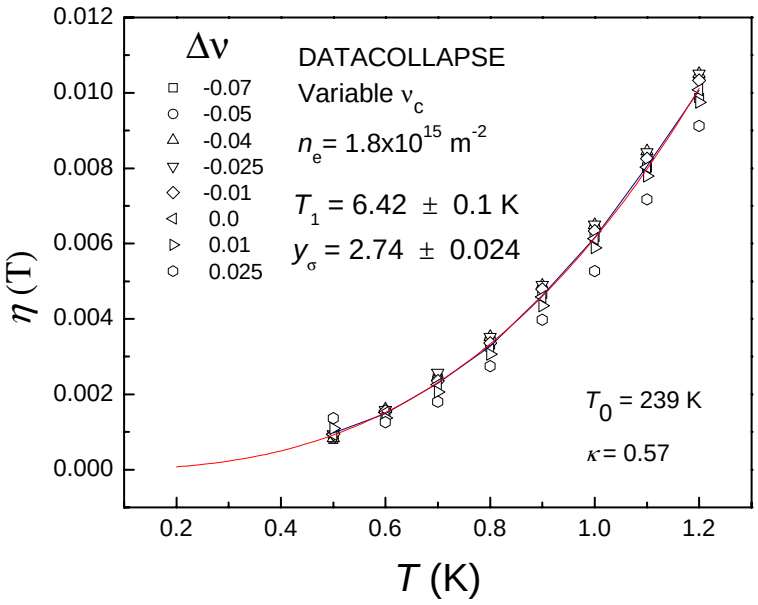

Figure 5.12 Collapse of the corrected ρ_H data onto a single curve $\eta = (\rho_H - 1)/\rho_o$ ($\widetilde{X}$) vs. T for different values of $\Delta\nu$. T_0, κ and $\delta\nu$ are taken from the 2D fit. $n_e = 1.8 \times 10^{15}$ m^{-2}.

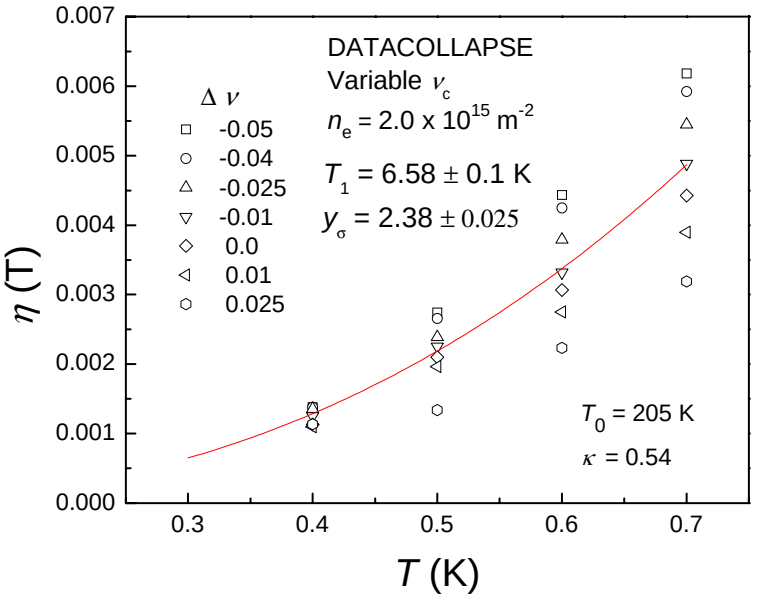

Figure 5.13 Collapse of the corrected ρ_H data (see *Fig.* 4.12) onto a single curve $\eta = (\rho_H - 1)/\rho_o$ ($\widetilde{X}$) vs. T for different values of $\Delta\nu$. T_0, κ and $\delta\nu$ are taken from the 2D fit. $n_e = 2.0 \times 10^{15}$ m^{-2}.

Notice that the datacollapse for $n_e = 2.0 \times 10^{15}$ m^{-2} shows more spread than for the previous densities. This is because we only could measure until 0.7 K for this density. In this low temperature range the effect is smaller and consequently the relative error is bigger.

5.4 Flow diagrams

By plotting σ_{xx} *versus* σ_{xy} for the *PI* transition using the tensor relation

$$\sigma_{xx} = \frac{\rho_{xx}}{\rho_{xx}^2 + \rho_{xy}^2}, \quad \sigma_{xy} = \frac{\rho_{xy}}{\rho_{xx}^2 + \rho_{xy}^2} \tag{5.19}$$

we construct the renormalization group flow diagram. Unfortunately, we were not able to directly measure the flow lines for $T > 1.2$ K. However, by making use of the universal scaling functions (see chapter 2)

$$\sigma_0(X,\eta) = \frac{e^{-X}}{1 + 2\eta e^{-X} + e^{-2X}} \tag{5.20}$$

$$\sigma_H(X,\eta) = \frac{1 + \eta e^{-X}}{1 + 2\eta e^{-X} + e^{-2X}} \tag{5.21}$$

with parameters κ, T_0, y_σ and T_1 as obtained from the experiment, we can plot the flow diagram up to higher temperatures. This most important diagram is shown in *Fig*. 5.14. The flow lines emerge from the Self Consistent Born Approximation (SCBA) curve [5] near $T \approx T_1 = 6.5$ K [2,3]. The scaling regime is entered below 4.2 K and is depicted by the (symmetric) upward flow towards the asymptotic semicircle ($T \rightarrow 0$) $\sigma_0^2 + (\sigma_H - e^2/2h)^2 = (e^2/2h)^2$ for the plateau-to-insulator transition.

The way we understand the complete flow diagram (i.e. displaying both relevant and irrelevant critical behavior) and how it should be interpreted has changed drastically since the first experimental study of scaling [5]. An early calculation of the flow diagram obtained from the dilute instanton gas method can be found in *Ref*. [6]. The only aspect that has remained unaltered in time is the presence of the semicircle for $T = 0$. This has been measured on all types of samples [7], regardless of their quality or even whether they displayed scaling properties or not. The only two criteria that need to be met in order to obtain a semicircle for the *PI* transition are a Hall resistance that remains quantized and an

exponentially diverging longitudinal resistance. In *Fig*. 5.14b) we reproduce an early flow diagram obtained for the 2→1 plateau-plateau transition [5]. When compared to our calculated flow diagram, based on the experimentally obtained parameters for the *PI* transition (sample 3388#1-W at $n_e = 1.8 \times 10^{15}$ m^{-2}), the differences are striking. In the early results, the trajectory of the flow lines towards the semicircle has been given a wrong interpretation. Also the expected particle-hole symmetry, causing the critical point to occur at half integer values of σ_{xy} was missing.

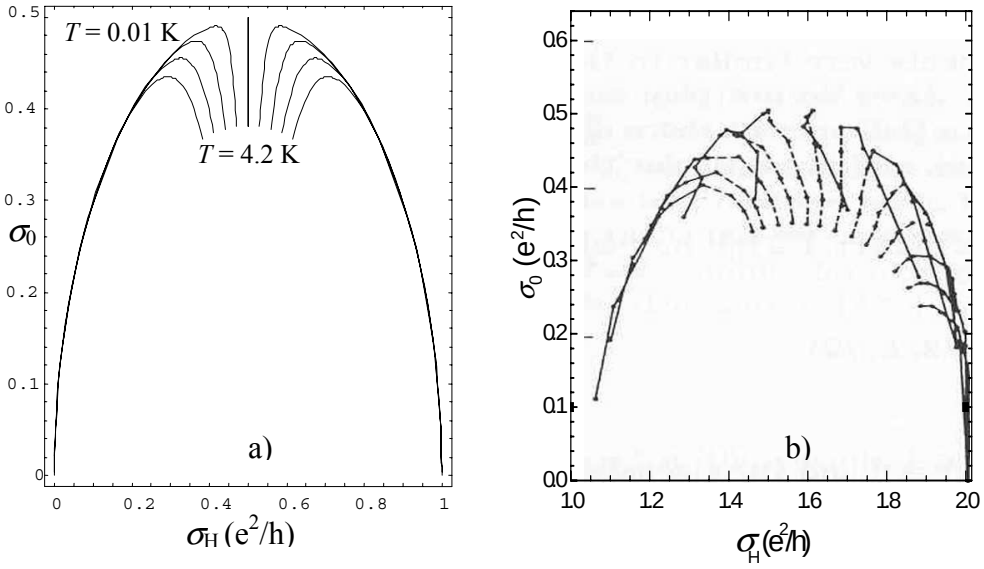

Figure 5.14 a) Temperature-driven flow lines with 0.01 < T < 4.2 K near the *PI* transition. The experimental values $T_0 = 202$ K, $T_1 = 6.4$ K, $\kappa = 0.53$ and $y_\sigma = 2.74$ have been used. b) Experimental σ_{xx} and σ_{xy} plotted as T-driven flow lines from T = 10 to 0.5 K for the *PP* transition 2→1 as taken from *Ref*. [5]. The dashed lines are from 10 to 4.2 K and the solid lines from 4.2 to 0.5 K.

The differences in the flow diagrams illustrate very well how our understanding of the process of scaling has evolved during the last decades. Initially the flow in the temperature range 4.2-10 K towards the semicircle in *Fig*. 5.12b) was attributed to the broadening of the Fermi-Dirac distribution with increasing temperature. Also it was thought that in the low-temperature regime 0.5-4.2K, where thermal broadening is much smaller than the Landau level broadening, proper scaling was represented in the flow diagram by the downward flow accompanied by a - not understood - decrease of σ_0 with temperature. Later, after having found experimental evidence for the already theoretically predicted irrelevant critical behavior, it turned out that the upward flowing of the conductivity lines towards the semicircle does represent genuine scaling behavior. The assumption that this had to be attributed to Fermi-Dirac broadening is wrong: Fermi-Dirac broadening does not play a significant role in the scaling regime. The major breakthrough in connecting the measured diagrams to the theoretically predicted ones, came through the understanding of how macroscopic inhomogeneities influence the observation of critical behavior [2,3,4]. It was shown [2,3,4] that *PP* transitions in general are much more sensitive to macroscopic sample inhomogeneities than PI transitions and as a result do not give proper flow diagrams. Thus only by measuring the *PI* transition, and considering both relevant and irrelevant critical behavior and the effect of sample inhomogeneities, the final flow diagram as shown in *Fig.* 5.14a can be obtained.

5.5 Conclusions

- The irrelevant critical behavior in the Hall resistance ρ_H near the PI transition was measured on an InGaAs/GaAs quantum well for three different electron densities. The data are analyzed within the scaling theory using a newly developed data collapse procedure. The extracted values for the irrelevant critical exponent y_σ and the temperature T_1 below which scaling sets in attain similar values for the three electron densities as shown in *Table* 5.1. The value $y_\sigma \approx 2.5$ corresponds well with the values reported in the literature [1,3].

Table 5.1 Value of T_1 and y_σ for $n_e = 1.3$, 1.8 and 2.0×10^{15} m^{-2}.

n_e	T_1 (K)	y_σ
1.3 x 10^{15} m^{-2}	6.46	2.48
1.8 x 10^{15} m^{-2}	6.42	2.74
2.0 x 10^{15} m^{-2}	6.58	2.38

- In order to obtain a good data collapse it appeared necessary to apply a small temperature dependent shift of the data in ν. Applying this shift improves the crossing point of the $\rho_{xy.s}$ data (*Fig.* 5.10). The fact that the critical filling factor has a small temperature variation underlines the high degree of macroscopic inhomogeneities in the sample: the filling factor differs when measured in different parts of the sample (compare *Figs* 5.2 and 5.4). The stretch tensor formalism, that assumes a linear variation of the electron density along the Hall bar, could not be used to analyze the data. Instead, we have chosen to look directly at the region of interest in the Hall bar by making use of the $\rho_{xy,s}$ data.

- The flow diagram of the PI transition has been calculated from the scaling functions using the experimental parameters for κ, y_σ, T_0 and T_1 extracted from the data collapse. The flow diagram shows all the properties predicted for genuine scaling: relevant and irrelevant flow, the location of the critical point $(\sigma_H, \sigma_0) = (½e^2/h, ½e^2/h)$ and particle-hole symmetry. The determination of the flow diagram was made possible after unraveling and fully understanding the effect of macroscopic sample inhomogeneities.

5.6 References

[1] L.A. Ponomarenko, *Ph.D Thesis* (University of Amsterdam, 2005), unpublished.

[2] A.M.M. Pruisken, D.T.N. de Lang, L.A. Ponomarenko and A. de Visser, *Solid State Communications* **137** (2006) 540.

[3] D.T.N. de Lang, *Ph. D Thesis* (University of Amsterdam, 2005), unpublished.

[4] B. Karmakar, M.R. Gokhale, A.P. Shah, B.M. Arora, D.T.N. de Lang, A. de Visser, L.A. Ponomarenko and A.M.M. Pruisken, *Physica E* **24** (2004) 187.

[5] H.P.Wei, D.C. Tsui and A.M.M. Pruisken, *Phys. Rev. B* **33** (1985) 1488.

[6] A.M.M. Pruisken, *Phys. Rev. Lett.* **32** (1985) 2636.

[7] M. Hilke, D. Shahar, S.H. Song, D.C. Tsui, Y.H. Xie and M. Shayegan, *Europhys. Letters* **46** (1999) 775.

6 Magnetotransport and optical properties of GaAs/InGaAs/GaAs quantum wells with a thin central AlAs barrier

6.1 Introduction

In recent years quantum wells with a complex potential profile have become of substantial interest. Thin barriers grown in the center of a quantum well and thus forming coupled quantum wells can tune the subband structure and in this way allow for desirable optical properties. Optical studies with thin AlAs or $Al_{1-x}Ga_xAs$ barrier layers incorporated in the well region demonstrated that the energy spectrum of the two-dimensional electrons could be tuned by changing either the barrier thickness or its height [1,2]. Such a tuning is utilized, for instance, in infrared photodetectors and lasers [3]. For practical use of quantum well structures high electron mobilities are desirable, and therefore it is of paramount importance to suppress electron-phonon scattering, which is dominant in modulation doped quantum well structures at temperatures above 100 K. Inserting a thin barrier in the quantum well that acts as a phonon wall is predicted to reduce the electron-phonon scattering. In transport experiments an increase in the electron mobility was observed when three AlAs barriers were inserted into a GaAs/AlAs multiple quantum well (QW) [4]. The reduction in scattering rate was attributed to the confinement of optical phonons [4], but in a theoretical paper [5] the effect was explained by a modulation of the electron states. In several theoretical papers [6-9] it has been calculated that the introduction of thin AlAs barriers in rectangular QWs leads to suppression of intersubband scattering by optical phonons, which in turn enhances the electron mobility. Other theoretical work has argued against an observable enhancement of the mobility [10-11]. Clearly consensus is lacking. In this chapter we will focus on single- and double sided delta doped GaAs/InGaAs/GaAs pseudomorphic quantum wells of different width and doping levels. This chapter is divided in two parts that correspond to two different series of measurements. In the first part we will report how inserting a thin central AlAs barrier, which acts as a phonon wall, changes

both the transport as well as the optical properties of the system [2]. This changing of transport and optical properties by the phonon wall is ascribed to the influence it has on the electron-optical phonon coupling and how this in turn influences the intra- and inter-subband electron scattering [3,6,10,11]. Three pairs of samples have been measured. In each pair the width of the QW and the doping level are the same. What is different is that only one sample of each pair has a central AlAs barrier (*Fig*. 6.1). We will present the magnetotransport data and how the presence of the phonon barrier reveals itself in comparing the transport parameters for the two components of each pair. Photoluminescence spectra will be shown for all six samples. The results will be compared with those of the transport measurements. Later on we will present the results of self-consistent numerical calculations of the subband structure and envelope wave functions for the measured samples [12]. Finally a comparison will be made between transport- and photoluminescence data and numerical simulations. The abovementioned experiments and simulations pointed out an undesired feature of our GaAs/InGaAs/GaAs structures, namely the occurrence of additional V-shaped potential wells coinciding with the regions of the delta-doped layers. This feature occurs due to both high doping level by Si at the delta-doped layers and insertion of the AlAs central barrier. As a consequence the spatial distribution of the wave functions has been changed, whereby some have extended over both the InGaAs and the delta-doped layer quantum wells and some have become localized within the delta-doped layer quantum wells. This feature has drastic consequences for the mobility of the structure (due to the change in scattering mechanism) and adds undesired phenomena such as parallel conductivity. In order to deal with this problem a new series of samples, using the compounds AlGaAs/InGaAs/GaAs, has been grown consisting out of a single quantum well with one-sided delta doping in the AlGaAs cladding barrier and its counterpart where the dopant layer is additionally confined by two AlAs barriers of 1 nm thickness. As shown with the first series of samples the AlAs barriers are a tool to push the energy levels up and reshape the wavefunctions. In this way we should be able to relocate the wave-functions in the main quantum well. The parameters extracted from the transport data and the results of numerical band-structure calculations will show in how far we have succeeded in this. Finally some suggestions will be made for future experiments.

6.2 First series of samples

6.2.1 Sample structure (1)

All samples described in this chapter were grown at the Institute of Ultrahigh Frequency Semiconductor Electronics by G.B. Galiev and I.S. Vasil'evskii. The first series of samples consists out of pseudomorphic $In_{0.12}Ga_{0.88}As$ quantum wells with and without central AlAs barrier, grown on semi-insulating (001) GaAs substrates with the use of molecular-beam epitaxy (MBE). The samples consist out of the following layers: a GaAs buffer layer 0.6 μm thick, a Si δ-doping layer, a GaAs spacer layer 8.5 nm thick. The $In_{0.12}Ga_{0.88}As$ quantum well with well widths L_{QW} of 8 or 12 nm, a GaAs spacer layer 8.5 nm thick, an upper Si δ-doping layer, and an i-GaAs layer 75 nm thick. The latter was grown to eliminate surface potential effects. The structures were covered with a cap layer of Si-doped GaAs 10 nm thick. The substrate temperature was 510 °C for the pseudomorphic QW and 590 °C for the other layers. Samples were prepared with δ-doping layers with Si concentrations of $3.2x10^{12}$ cm^{-2} (heavily doped, samples #1 and #2) and $1x10^{12}$ cm^{-2} (moderately doped, samples #3 - #6). Samples without barrier (#1, #3, #5) and with barrier (#2, #4, #6) were prepared. The barrier consists of three monolayers of AlAs grown in the center of the QW. The structural and electro-physical characterization of the samples has been reported in *Ref.* [13]. In order to carry out transport measurements all samples were prepared in Hall bar geometry by conventional lithography and wet etching. In order to attach current and voltage leads, AuGe/Ni/Au ohmic contact pads were made on the samples. The structures are schematically shown in *Fig*. 6.1.

6.2.2 Transport properties

In *Fig.* 6.2 the temperature dependence of the sheet resistance measured for T = 4.2-300 K for all samples is shown. These curves where measured at the Low Temperature Physics Department of the Moscow State University by V.A. Kulbachinskii and co-workers. For the heavily doped samples #1 and #2 the resistance attains lower values and has weaker temperature dependence than the moderately doped samples (#3 - #6). The samples #3 and #5, with no barrier show metallic behavior from 300 K down to ~70 K, where the resistance decreases approximately linearly with decreasing temperature.

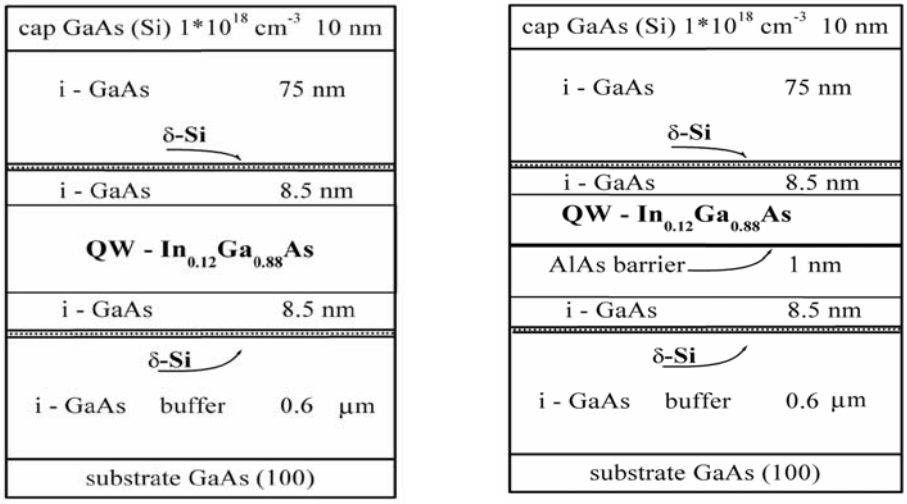

Figure 6.1 Schematic sample structure for the $In_{0.12}Ga_{0.88}As$ quantum wells: (a) without AlAs-barrier (samples #1,#3 and #5) and (b) with AlAs central barrier (samples #2, #4, #6). The width of the QW is 12 nm for sample #1 and #2 and 8 nm for samples #3-#6.

The temperature and magnetic field variation of the resistance below 70 K can be attributed to weak localization effects. The insertion of the barrier has a pronounced effect on the sheet resistance, notably in the moderately doped samples. In samples #4 and #6 the value of the resistance at 4.2 K increases by a factor 3 and 7 compared to samples #3 and #5 respectively. This large difference in resistance decreases with increasing temperature. The resistance values of the single QW sample #5 are smaller than those of sample #3, even though the well width is smaller (8 nm compared to 12 nm). This is due to the slightly larger carrier concentration in sample #5 (~ 5 %) as determined by the low temperature Hall data (see *Table* 6.1). The Hall densities n_H and Hall mobilities μ_H were determined at temperatures of 4.2, 77 and 300 K for all samples. An overview of the results is presented in *Table* 6.1. The Hall density n_H is derived from the linear part of ρ_{xy} according to:

$$n_H = -\frac{B}{\rho_{xy} e} \tag{6.1}$$

The Hall mobility is derived from:

$$\mu_H = \frac{\partial \rho_{xy}}{\partial B} \frac{1}{\rho_{xx(B=0)}} \tag{6.2}$$

Where ρ_{xy} and ρ_{xx} are the Hall resistivity and longitudinal resistivity's of the 2DEG. For the heavily doped samples #1 and #2 the Hall density amounts to 2.6-2.7x10^{12} cm^{-2} and is roughly temperature independent (to within ~ 10%). Also the mobility is quite low, which indicates that ionized impurity scattering is dominant. For the moderately doped single QWs (#3 and #5) the temperature variation of n_H and μ_H is consistent with the metallic behavior observed in the resistance. The overall increase of the mobility with decreasing temperature is attributed to the reduction in the phonon scattering rate. However, in the samples with barrier, #4 and #6, the Hall mobility on the whole decreases with decreasing temperature. At low temperatures (4.2 K and 77 K) the insertion of the barrier leads to a strong reduction of mobility by a factor 3-5, although the Hall density is roughly constant or even shows an increase (<20%).

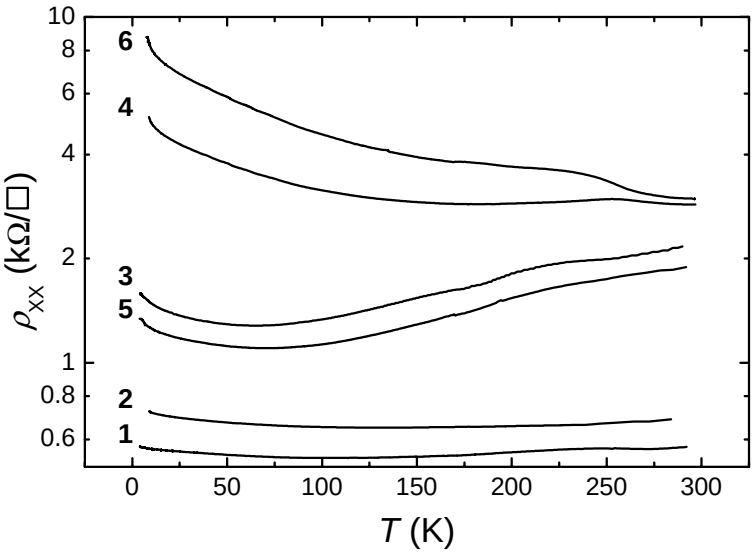

Figure 6.2 Temperature dependence of the sheet resistance for the $In_{0.12}Ga_{0.88}As$ quantum wells with (#2, #4, #6) and without (#1, #3, #5) the AlAs-central barrier.

Table 6.1: Structural and transport parameters (at T = 300 K, 77 K and 4.2 K) of the InGaAs QW samples; '*b*' indicates the presence of the AlAs-barrier.

sample	L_{QW}	N_d (Si)	T = 300 K		T = 77 K		T = 4.2 K	
			n_H	μ_H	n_H	μ_H	n_H	μ_H
#	nm	10^{12} cm^{-2}	10^{12} cm^{-2}	cm^2/Vs	10^{12} cm^{-2}	cm^2/Vs	10^{12} cm^{-2}	cm^2/Vs
1	12	3.2	2.72	3830	3.0	4700	2.86	3800
2	12+b	3.2	2.6	3150	2.33	5420	2.61	3300
3	12	1.04	0.54	5740	0.79	18500	0.52	10000
4	12+b	1.04	0.42	481 0	0.78	5300	0.57	2070
5	8	1.1	0.53	5910	0.76	18700	0.59	7980
6	8 + b	1.1	0.50	4000	0.87	3570	0.47	1520

Magnetotransport data

The longitudinal- and Hall resistance has been measured for all the samples up to 12 T in the temperature range of 0.25-4.2 K using the lock-in technique. In *Figs*. 6.3a-f, we present the results obtained for samples #1 to #6 respectively. In the heavily doped samples #1 and #2, the overall behaviour of the longitudinal resistance shows positive quadratic field dependence. The longitudinal component of samples #3-#6 exhibits a negative linear magnetoresistance, which is indicative of weak localization in low-density two-dimensional semiconductor structures. Samples #1-#5 display pronounced Shubnikov - de Haas (SdH) oscillations. After substracting the background and performing a Fast Fourier Transform on the SdH oscillations as function of 1/*B* we obtain the frequencies of the oscillations. Every frequency (*f*) corresponds to a (partially) filled subband. Making use of the relation [14]

$$n_e = \frac{2e}{h}.\frac{1}{T}, \tag{6.3}$$

where T is the period of the SdH-oscillations in the ρ_{xx} vs. 1/*B* plot, we can relate the frequencies to the electron density of the respective subband. Usually only subbands with a high quantum mobility are visible in the SdH oscillations. The subband densities obtained in this way are shown in *Fig.* 6.3. For samples #1-#5 only one frequency peak is observed, which means that the SdH-oscillations correspond to one subband. For sample #6 no clear

frequency is present in the FFT, which is due to the low mobility (see *Table* 6.1) and the long oscillation period. In the heavily doped samples #1 and #2 the SdH density decreases from 1.35×10^{12} cm^{-2} to 0.63×10^{12} cm^{-2} due to barrier insertion. This will be explained in section 6.2.6. The SdH density approaches the Hall density in the moderately doped samples #3-#6, but is much lower than the Hall density for the heavily doped samples #1-#2, especially for sample #2, indicating that several subbands are populated.

Quantum mobilities were determined from the envelope of the SdH-oscillations [15]. For the moderately doped samples the SdH- and Hall densities are comparable, indicating that transport is dominated by one high mobility subband. The Hall resistance (R_{xy}) is the most pronounced in the samples without barrier (odd numbers) because of the higher mobility. In samples #3-#6 we observe the quantum Hall effect regime with the integer plateaus corresponding to the filling factors $\nu = 2$ and 4. The Landau Levels are non-spin split in this region of the magnetic field. At these integer filling factors $R_{xx}=0$, which demonstrates the absence of parallel conduction. In samples #1 and #2 parallel conduction is obviously present and hampers the observation of the QHE.

6.2.3 Photoluminescence

Photoluminescence (PL) measurements have been carried out on all six samples. The corresponding spectra at $T = 77$ K are shown in *Fig*. 6.5. These curves where measured at the Low Temperature Physics Department of the Moscow State University by V.A. Kulbachinskii and co-workers. The spectra of all six samples exhibit a maximum in the energy range 1.35-1.47 eV, which is below the transition energy in bulk GaAs (1.508 eV). Notice that insertion of the barrier leads to a significant upward shift of the peaks in the order of 0.05 eV, without a substantial decrease of the PL intensity. The peaks for the single QWs (#1, #3, #5) are relatively broad and asymmetric with respect to the peaks for the coupled QWs. This indicates that the spectra of the single QWs are composed of several peaks with closely spaced subband energies. The samples with barrier do not dispay any additional transitions. This is attributed to the decreasing energy differences between the subbands due to the barrier. These energy gaps between the two electron subbands become so small that photoluminescence measurements cannot resolve the different transitions. Also note that for the single QW samples #1 and #3, which have the same well width but

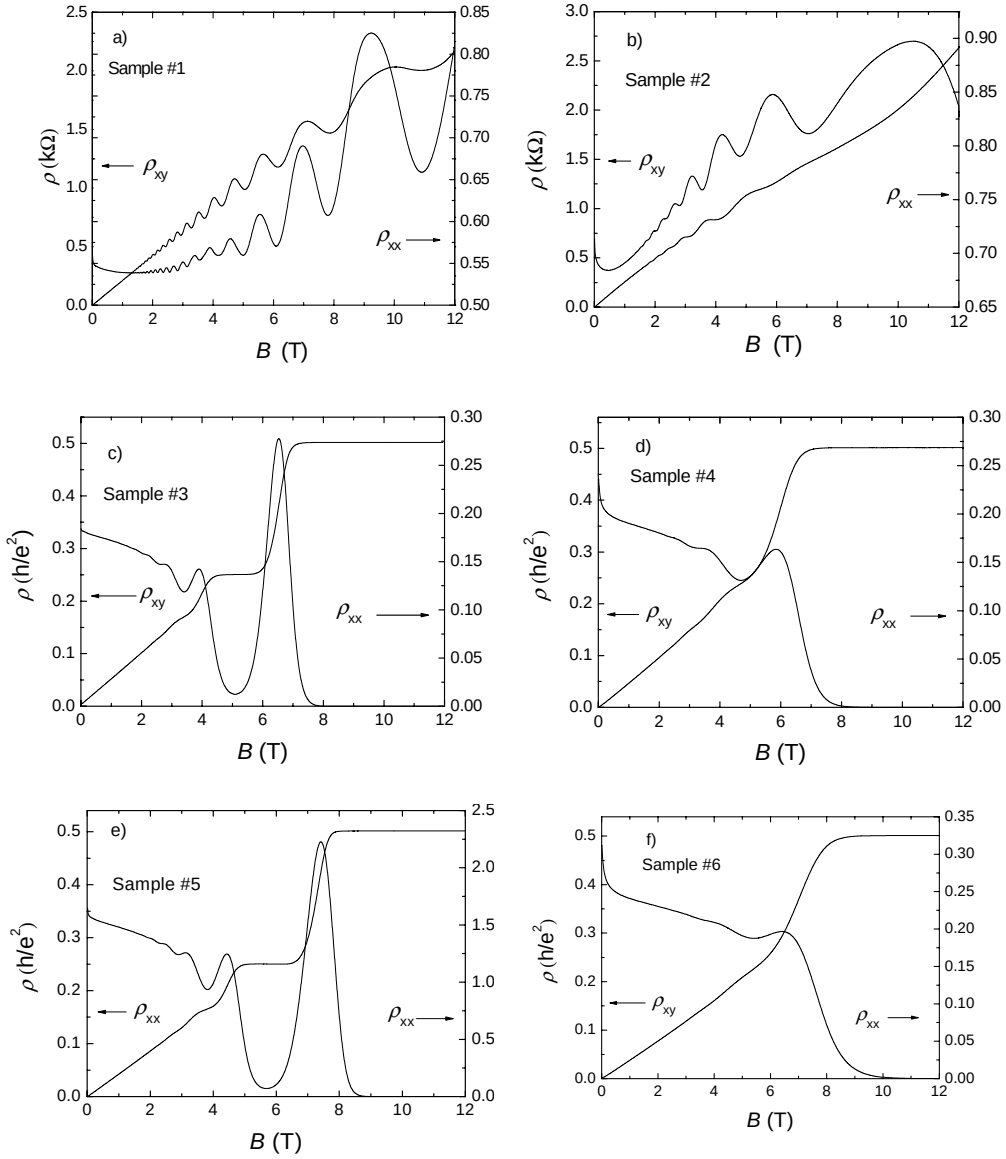

Figure 6.3 a)-f) Magnetotransport curves for the samples #1- #6 at T = 0.25 K.

different doping levels, the transition energies differ slightly (by 0.02 eV). After insertion of the barrier this energy difference disappears.

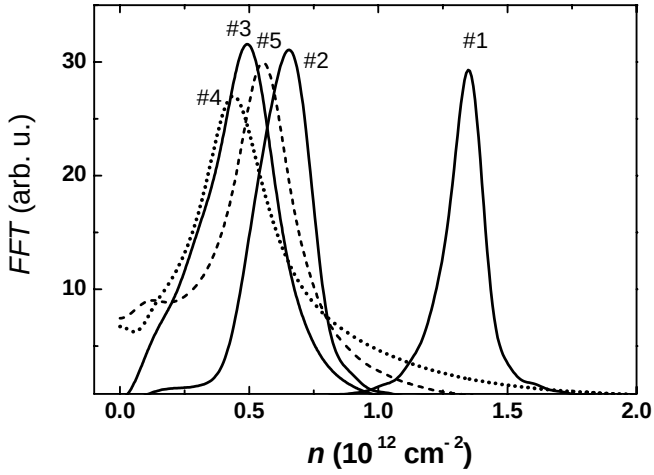

Figure 6.4 Fast Fourier spectra of the Shubnikov - de Haas oscillations for samples #1-#5 at T = 0.25K. The horizontal axis has been rescaled using *Eq*. 6.3 to show the electron-density obtained from the FFT.

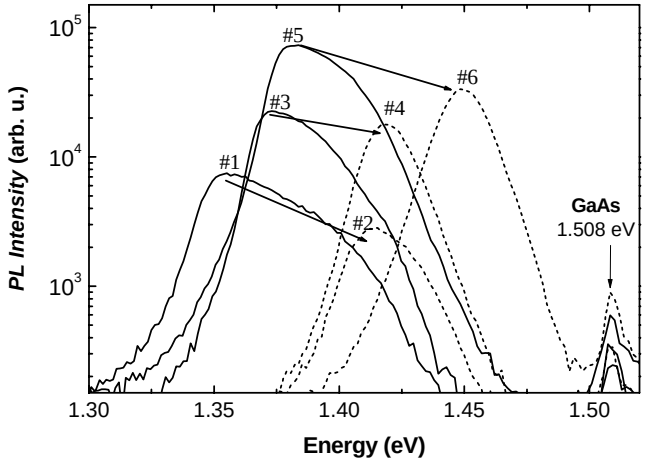

Figure 6.5 Photoluminescence spectra measured at T = 77 K for the $In_{0.12}Ga_{0.88}As$ quantum wells with AlAs barrier (#2, #4, #6) and without (#1, #3, #5).

6.2.4 Subband structure and wave function calculations

The conduction band profile and the subband structure and energy levels were calculated for all the structures by solving the Schrödinger and Poisson equations self consistently [12]. The width of the δ-doping layers has been taken 5 nm [16]. The results of these calculations for all six samples are presented in *Fig*. 6.6.

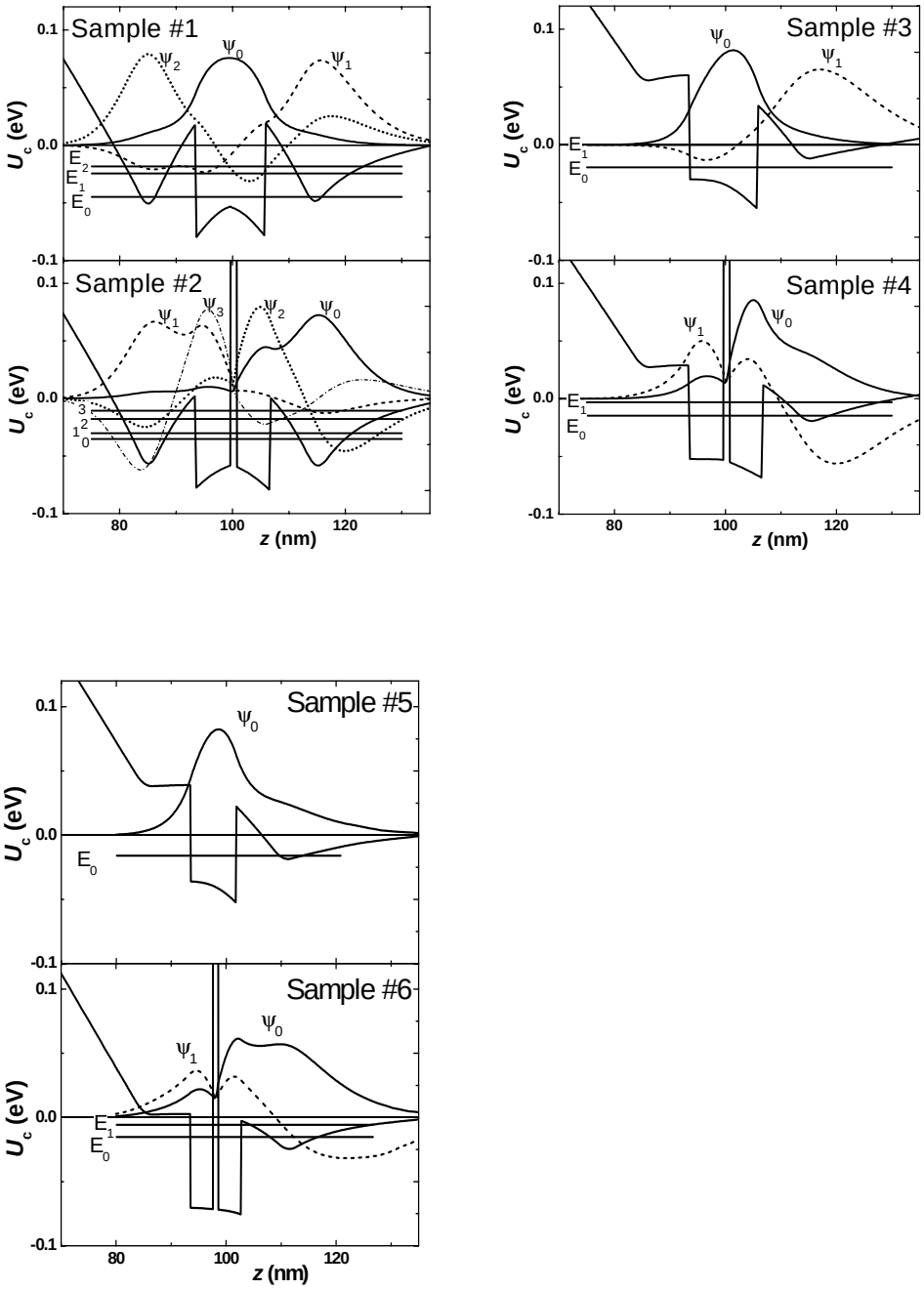

Figure 6.6 Calculated conduction band profiles, electron wave functions and subband energy levels for samples #1- #6.

Comparing the conduction band profile of the heavily doped samples (#1 and #2) and the moderately doped (#3-#6) we notice an important difference. In the heavily doped samples the δ-doped layers form additional V-shaped quantum wells almost of the same depth as the InGaAs QW. In sample #1 the ground state wavefunction Ψ_0 with energy E_0 is predominantly situated in the InGaAs QW, but partially penetrates the V-shaped QWs. The wavefunctions Ψ_1 and Ψ_2 are mainly confined in the V-shaped QWs and results in two decoupled subbands labeled E_1 and E_2. Insertion of the AlAs barrier (sample #2) causes a tunnel splitting of the central QW state Ψ_0 into the wavefunctions Ψ_2 and Ψ_3 and an upward shift of the subband energies E_2 and E_3 (before E_0). Hence the central QW states are no longer the ground state. The wave functions in the V-shaped QWs (Ψ_0 and Ψ_1) are less affected by the insertion of the barrier. Since wavefunction Ψ_2 and Ψ_3 are spread over the central QW and the V-shaped QWs, insertion of the barrier causes an increase of the electron density in the area of the V-shaped QWs and a decrease of the electron density in the area of the central QW. In the moderately doped QWs (#3 and #5) the V-shaped δ-layer QWs are significantly weaker. The conduction band profile is asymmetric. The ground state wavefunction is confined into the QW. As for the excited states, only states formed in the deeper V-shaped QW are below the Fermi energy. We observe that for sample #3 the ground state energy level E_0 lies below the deeper V-shaped QW, meaning that the electrons of the ground state subband are mainly confined in the central QW. Insertion of the AlAs barrier leads again to a redistribution of the wavefunction Ψ_0 towards the V-shaped QW. A similar redistribution of the wavefunction after insertion of the barrier can also be seen in samples #5 and #6.

6.2.5 Comparison of transport measurements, PL and calculations

The predicted upward shift in energy levels is most clearly seen in the PL data where the energy shift is in the order of 0.05 eV. The transport measurements reveal a slightly more complicated situation. For the heavily doped sample #1 the electron density of the high mobility subband, associated with the central QW, indeed decreases considerably: from 1.35×10^{-12} cm^{-2} to 0.63×10^{-12} cm^{-2} (*Fig*. 6.4). However, in the moderately doped sample #3 the electron density decreases only by 10% after barrier insertion (*Fig.* 6.4). From the band structure calculations it becomes clear that there is a strong influence of the δ-doped layers, which act as V-shaped QWs. For sample #3 it means that insertion of the barrier causes the

central wavefunction ψ_0 to delocalize and to form a hybrid state occupying both the central QW and the V shaped QW. From the calculations (*Fig.* 6.7) it follows that the groundstate energy E_0 shifts only slightly after insertion of the barrier (<0.005 eV). In fact the hybridization of the wavefunction over the central QW and the V shaped QW is equivalent to an enlargement of the QW. This causes the energy-shift to be smaller than expected. This calculated shift in energy level of the ground state is much smaller than the measured PL shift of 0.05 eV, but the shift in the photoluminescence data is also due to the shift in hole subband energy. The hybridization of the wave function causes also a decrease in mobility (see *Table* 6.1). This is because the scattering mechanism changes from phonon scattering (dominant in the central QW) to ionized impurity scattering (dominant in the V-shaped QWs). In case of the narrowest QW (samples #5 and #6) this shift of the wavefunction to the V-shaped QW is the most drastic which results in sample #6 having the lowest mobility. Notice that the transport mobility of sample #1 hardly decreases after barrier insertion (for T = 77 K it even increases). This can be explained from the bandstructure calculations. We see that ψ_0 is hybridized into ψ_2 and ψ_3. The corresponding energy level E_0 is split and shifted upward drastically. The expected decrease in mobility does not occur since the V-shaped QWs are already occupied by ψ_0 and ψ_1. These wavefunctions provide effective screening from the ionized impurity potential, so the mobility in the third subband stays high. From this we can conclude that the observed frequency in the SdH oscillations of sample #2 is attributed to the third hybrid subband. So far we have encountered the undesired effects of the δ-doped layer potential wells. There are several ways to deal with this. One way would be to make the central QW much deeper than the V-shaped QW, so that the wavefunctions are only localized in the central QW. In practice this is difficult to realize, since a material has to be found with a similar lattice constant as GaAs. One can also increase the cladding barrier height by using an $Al_xGa_{1-x}As$ compound layer. Another way is to make use of the same method described above: Inserting AlAs barriers around the δ-doped layers in order to shift the energy levels upward and thus the wavefunctions out of the V-shaped QW. The last method has been adapted, together with the use of an $Al_xGa_{1-x}As$ compound layer as cladding barrier, and samples with two AlAs-layers of one nm in width surrounding the δ doped layers have been grown. The results obtained from these samples will be presented in the next sections.

6.3 Second series of samples

6.3.1 Sample structure (2)

The second series of sample structures was grown in order to find out if the effects of the V-shaped QW at the height of the δ doped layer(s) can be neutralized. Central in these new structures is a pseudomorphic $Al_{0.22}Ga_{0.78}As/In_{0.2}Ga_{0.8}As/Al_{0.22}Ga_{0.78}As$ quantum well. These six samples can be again divided in three pairs. In the first pair a single quantum well with one-side δ-doping is compared with the same structure, but with two additional AlAs barriers of one nm in width around the Si δ-doped layer (samples #416 and #417). The second pair is similar, only with a lower doping level (samples #440 and #444). The last two samples are double-sided δ-doped single quantum wells that differ in doping level (samples #397 and #407). No additional AlAs barriers are added here (*Fig.* 6.7).

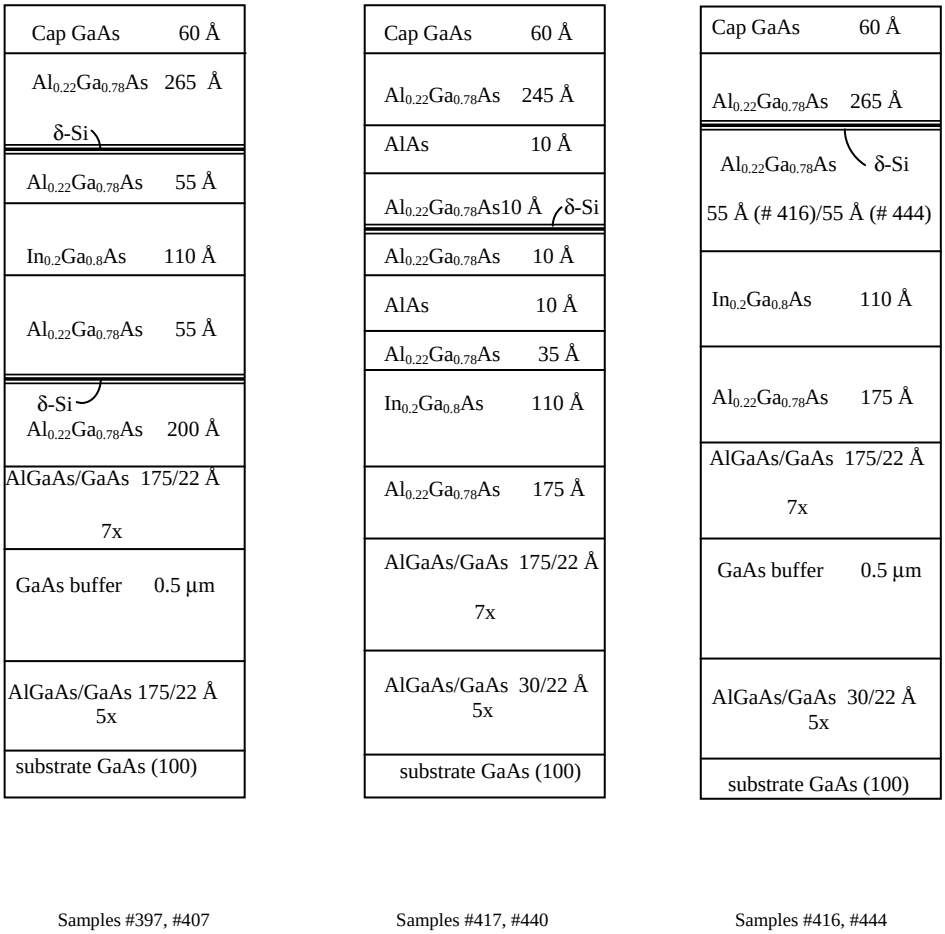

Figure 6.8 Sample structures of samples #397, #407, #417, #440, #416, and #444.

The reason for adding two AlAs barriers surrounding the dopant layer (samples #417, #440) is that some separation is needed between the Si-donors and the AlAs layer, in order to prevent formation of DX-centers which would trap part of the donor electrons.

6.3.2 Transport data and band-structure calculation

Let us consider the first pair of samples (#416, #417). The transport data are presented in *Figs*. 6.9 and 6.10 below.

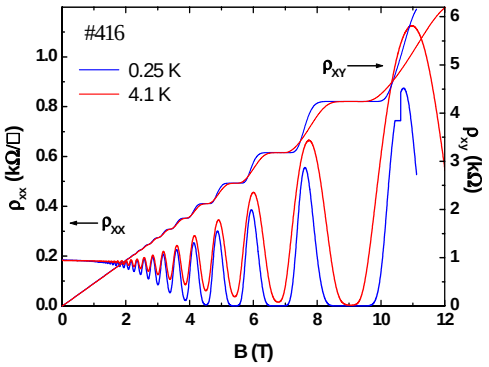

Figure 6.9 Hall- and longitudinal resistivity for #416 at temperatures of 0.25 K and 4.1.

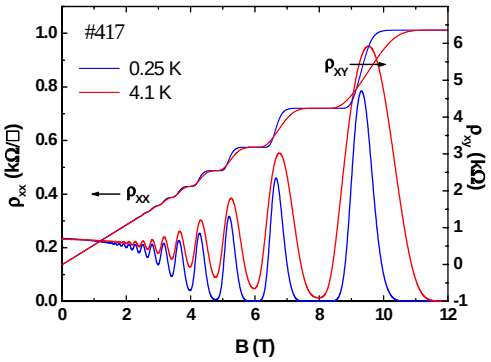

Figure 6.10 Hall- and longitudinal resistivity for #417 at temperatures of 0.25 K and 4.1K.

In sample #416 the highest plateau corresponds to filling factor $\nu = 6$. In sample #417 the highest plateau corresponds to $\nu = 4$. The SdH oscillations for both samples are well pronounced. The SdH and Hall densities for all samples are shown in *Table* 6.2. For both samples #416 and #417 n_{SdH} and n_H coincide. This indicates that only one subband is filled. The decrease of both n_{SdH} and n_H after barrier insertion can be attributed to the previous mentioned DX centers formation due to the AlAs atoms, which trap part of the dopant electrons. Next we consider the subband structure calculation for both samples.

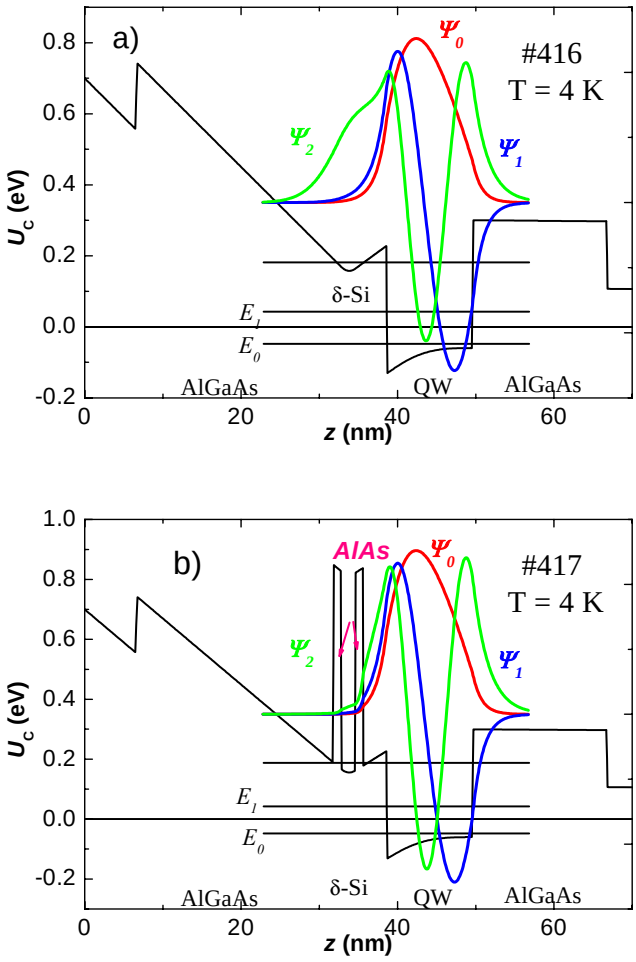

Figure 6.11 Subband structure and wavefunctions for a) #416 and b) for #417.

For sample #416 we see a wave function mainly confined to the V shaped QW (ψ_1), and a hybridized wavefunction (ψ_2). Inserting the AlAs barriers reconstructs the wavefunctions (*Fig.* 6.11b). The wavefunction ψ_1 is now fully confined to the QW together with ψ_0. The wavefunction ψ_2 is also reconstructed. The shift in energy levels after barrier insertion is minimal. However in both cases only one subband lies below the Fermi level.

Now let us consider sample pair #440 and #444. The transport data are shown in *Figs*. 6.12 and 6.13.

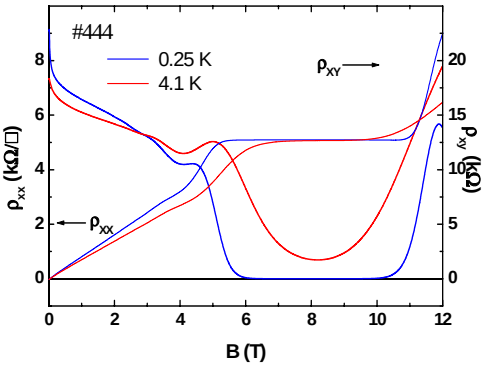

Figure 6.12 Hall- and longitudinal resistivity for #444 at *T* = 0.25 K and 4.1 K.

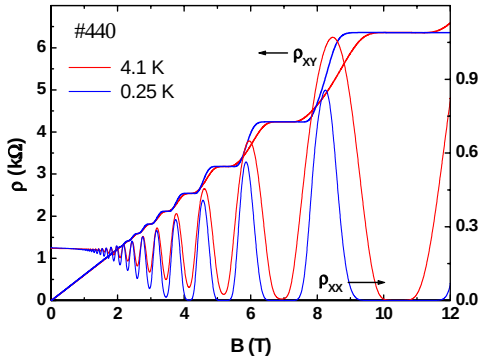

Figure 6.13 Hall- and longitudinal resistivity for #440 at T = 0.25 and 4.1 *K*.

For sample #444 both the electron density (n_H) and transport mobility are low (see *Table* 6.2), resulting in a very weak presence of SdH oscillations. The slope of the linear part of the Hall resistance varies with temperature, which means there is a temperature dependence of the electron density. So for this sample either doping has been insufficient, or the DX-centers formation immobilizes a significant part of the electrons. A suggestion to overcome the second feature could be to illuminate the sample. In *Fig.* 6.14 we show the band structure of both samples #440 and #444.

Again in both samples there is only one subband below the Fermi level. The subband electron concentration has been determined in the usual way of substracting a background from the SdH-oscillations, plotting the result vs 1/*B* and performing a FFT. The results of the Fourier transforms are shown in *Fig.* 6.15. For the double sided δ-doped samples we obtain the transport-data shown in *Figs.* 6.16a) and b).

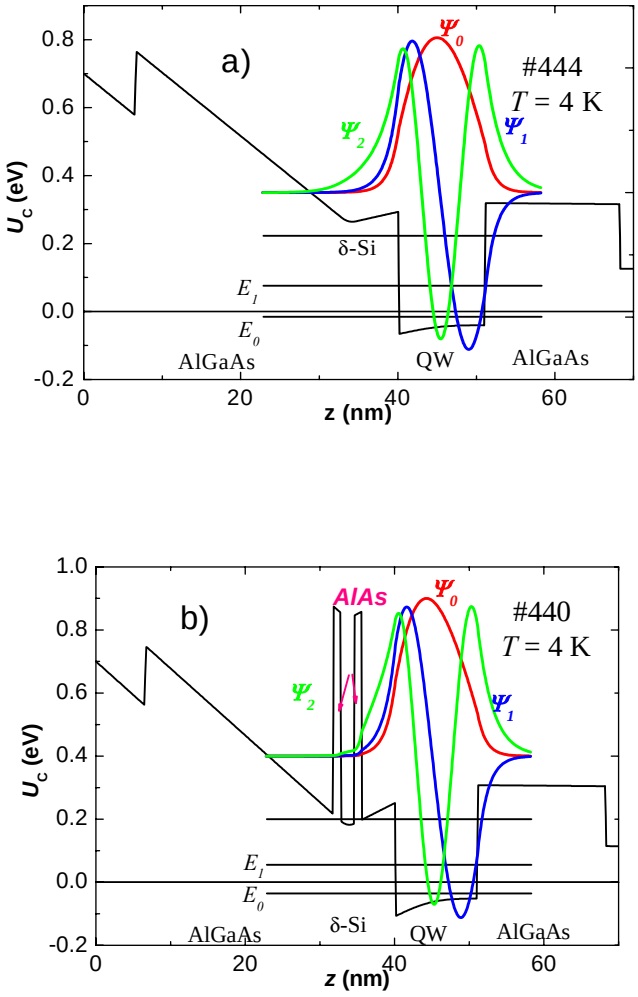

Figure 6.14 Subband structure and wavefunctions for a) #444 and b) for #440.

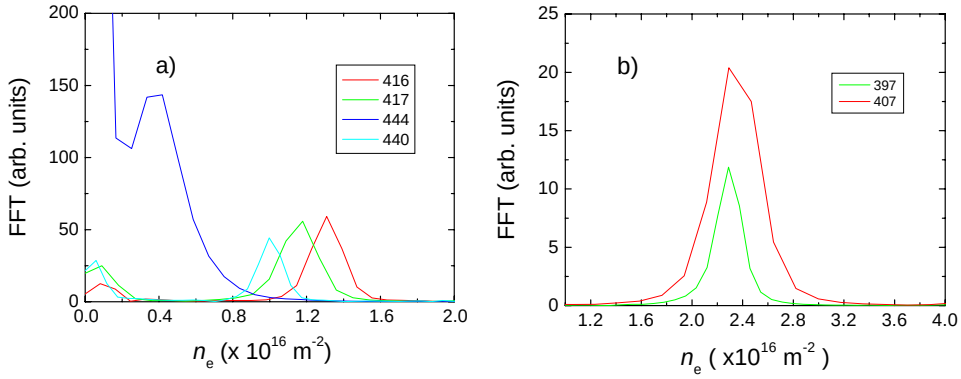

Figure 6.15 Fast Fourier spectra of the SdH oscillations for a) samples #416, #417, #444, #440, b) #397 and # 407 at T = 4.1 K. The horizontal axis has been rescaled to show the electron density using *Eq.* 6.3.

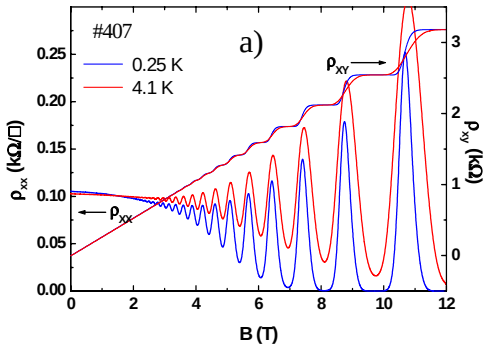

Figure 6.16a Hall- and longitudinal resistivity for #397 at T = 0.25 K and 4.1 K.

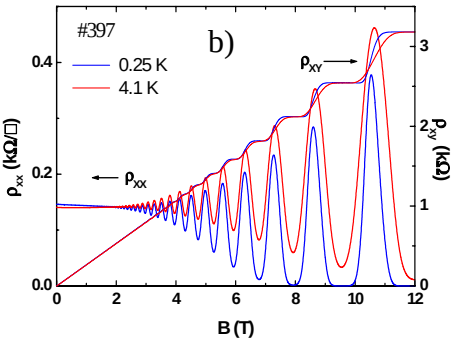

Figure 6.16b Hall- and longitudinal resistivity for #407 at T = 0.25 and 4.1 K.

SdH oscillations are very well pronounced in both samples. Now consider the subband structure shown in *Fig.* 6.17.

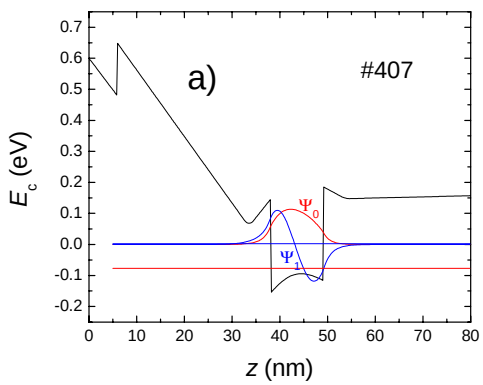

*Figure 6.17*a Subband structure and wavefunctions for #407.

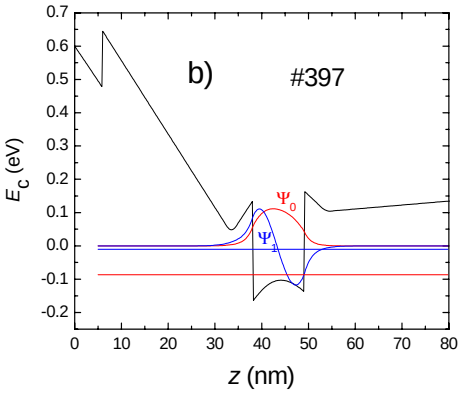

Figure 6.17b Subband structure and wavefunctions for #397.

The addition of a second dopant layer indeed leads to a more symmetric QW. For both samples the second subband ψ_1 is close to the population edge. Since #397 has a higher doping level, the second subband is slightly filled by electrons. For sample #407 the second subband is already depopulated. This depopulation of the second subband in sample #407 explains n_{SdH} and n_H being similar for this sample.

Table 6.2: Doping level and transport parameters at T = 4.1 K for samples #416, #417, #444, #440, #397 and #407.

Sample #	Doping (cm^{-2})	n_H (10^{12} cm^{-2})	μ_H ($cm^2/(Vs)$)	n_{SdH} (10^{12} cm^{-2})
416	5.9 x 10^{12}	1.32	25880	1.31
417	5.9 x 10^{12}	1.16	23100	1.16
444	5.4 x 10^{12}	0.4	28790	0.4
440	5.4 x 10^{12}	1.02	2310	1.0
397	6.3 x 10^{12}	2.37	18364	2.25
407	5.7 x 10^{12}	2.37	25708	2.37

Summarizing, for this second series of samples we can say that the main effect we hoped to observe after the insertion of the additional AlAs barriers in the V-shaped quantum wells

does not show up in the data and calculations. Ideally, what we would like to see is the occurrence of parallel conduction in the V-shaped quantum well, for the samples without barriers. This parallel conduction should disappear after insertion of the barriers, since the energy levels will shift and the wavefunctions become reconstructed and should become fully localized in the main quantum well. Another expected effect of the barrier would be the increased transport mobility in the sample. This is due to the change in scattering mechanism (from ionized impurity scattering to phonon scattering). The reason for not observing this is that in all four samples with additional AlAs-barriers (# 416, #417, #444 and #440) the electron density is not high enough to have more than one subband filled. Only the lowest subband is filled, of which in all four cases the energy level lies below that of the V-shaped quantum wells (see *Figs*. 6.11 and 6.14). We do observe a reconstruction of ψ_2 in sample 417 (*Fig.* 6.11b). However this effect does not influence the transport data, since this subband is empty. Suggested future attempts, in order to show the uplifting of the energy-levels by barrier insertion, leading to reshaping the wavefunctions and re-localizing them in the central QW, could consist in trying to obtain samples with higher electron concentration. This can be achieved by illuminating the sample after cooling down, to use a gate electrode in order to fill the V-shaped quantum well or by growing sample structures with higher doping levels.

6.4 Conclusions

For the first series of samples measured, all three methods used, magnetotransport, photoluminescence and calculation of the bandstructure, reveal that insertion of a thin central AlAs barrier influences the spatial distribution of the electron wave functions and causes an upward shift of the corresponding energy levels. Since the delta doped layers themselves cause V-shaped quantum wells, the wavefunctions reshape into hybrid states spread over the main quantum well and the V-shaped δ doped layers. Because of this ‘spread’ of the wavefunctions, the dominant scattering mechanism changes from phonon scattering into ionized impurity scattering. This results in the lowering of the transport mobility. In the heavily doped samples (#1 and #2), the subband responsible for transport is effectively screened from this ionized impurity scattering by the electron subbands fully localized in the V-shaped quantum wells. Since these V shaped quantum wells hinder the original goal of our experiments, a second series of samples has been grown. The reasoning

behind these is that the same technique used in the first series of samples to shift the energy levels and reshape the wavefunctions (namely the central AlAs barrier), this time used in the V shaped δ layer quantum wells, should be able to reshape the wavefunctions in such a way that they become localized only in the quantum well. Calculations of the bandstructures show that this in principle should be possible. Unfortunately the electron density in the actual samples was not high enough to obtain convincing evidence for this. In future attempts to determine the effect of AlAs barriers on the energy levels of the subbands and the shape of the wavefunctions, we strongly recommend that samples with a higher electron density should be used.

6.5 References

[1] T.Schmiedel, B.D. McCombe, A. Petrou, M. Dutta and P.G. Newman, *J. Appl. Phys*. **72** (1992) 4753.

[2] Q.X. Zhao, S. Wongmanerod, M. Willander, P.O. Holtz, E. Selvig and B.O Fimland, *Phys. Rev. B* **62** (2000) 10984.

[3] W. Trzeciakowski and B.D. McCombe, *Appl. Phys. Lett.* **55** (1989) 891.

[4] X.T. Zhu, H. Goronkin, G.N. Maracas, R. Droopad and M. Stroscio, *Appl. Phys. Lett.* **60** (1992) 2141.

[5] T. Tsuchiya and T. Ando, *Phys. Rev. B* **48** (1993) 4599.

[6] J.Pozela, V. Jucene and K. Pozela, *Semicond. Sci. and Techn.* **10** (1995) 1076.

[7] J.Pozela, A. Namajunas, K. Pozela and V. Juciene, *J. Appl. Phys*. **81** (1997) 1775.

[8] J.Pozela, A. Namajunas, K. Pozela and V. Juciene, *Physica E* **5** (1999) 108.

[9] X.F. Wang, I. C. Da Cunha Lima and X.L. Lei, *Phys. Rev. B* **58** (1998) 12609.

[10] C.R. Bennet, M.A. Amato, N.A. Zakhleniuk, B.K. Ridley and M. Babiker, *J. Appl. Phys.* **83** (1998) 1499.

[11] X.F. Wang, I.C. Da Cunha Lima, and X.L. Lei, *J. Appl. Phys.* **85** (1999) 6598.

[12] H.Tan, G.L. Snider, L.D. Chang and E.L. Hu, *J. Appl. Phys.* **68** (1990) 4071.

[13] I.S. Vasil'evskii, V.A. Kulbachinskii, G.B. Galiev, R.M. Imamov, A.A. Lomov and D. Prohorov, Proc. Int. Conf. on Micro- and Nanoelectronics, ICMNE-2005, Moscow Zvenigrod, Russia (2005) 2.

[14] E. Tiras, M. Cankurtaran, H. Celik and N. Balkan, *Phys. Rev. B* **64** (2001) 11.

[15] E**.** Skuras, R. Kumar, R.L. Williams, R.A. Stradling, J.E. Dmochowski and P. Wisniewski, *Semicond. Sci. Technol.* **6** (1991) 535.

[16] A. Leuther, A. Forster, H. Luth, H. Holzbreche and U. Breuer, *Semicond. Sci. Technol.* 11 (1996) 766.

7. Effect of tilted magnetic field on $In_xGa_{1-x}As$/GaAs bilayer quantum well with large Landé *g*-factor

7.1 Introduction

Whereas the single quantum well (SQW) is considered a standard topic in condensed matter physics, this is not the case for the double quantum well (DQW). Research on DQWs has been pioneered by Boebinger et al. [1,2,3] and still new facets of it are being discovered and explored today. The DQW adds several new dimensions to the physics describing the SQW. One is the existence of collective interlayer modes [4], due to inter-particle interactions between the layers. These interactions can be regulated by the distance between the quantum wells or by applying a magnetic field parallel to the DQW ($B_{\|}$). Another is the additional degree of freedom that an electron has (in which of both wells is it?), usually called the isospin or pseudospin [5]. Magnetotransport studies disclose relevant information about the subband structure in DQWs and how this structure is influenced by a magnetic field component parallel to the DQW. The magnetoresistane picture of the DQW is more complicated than for the SQW, since we have to consider not one Landau level fan, but two overlapping ones. This is due to the symmetric-antisymmetric splitting of the subband also called tunneling gap [6,7]. Most of the research on DQWs has been performed on GaAs/AlGaAs heterosystems having an optimal lattice match between the compounds and giving high mobilities. The biggest drawback of GaAs is its small Landé *g*-factor ($|g|$=0.44). The spin splitting observed in these types of DQWs is more than an order of magnitude enhanced at local magnetic fields because of exchange-correlations. This has been motivation enough for us to switch to a new heterosystem. In this chapter we will present magnetotransport data taken on an $In_xGa_{1-x}As$/GaAs heterosystem. The much bigger (positive) bulk value of the *g*-factor for InGaAs ($g \approx 3$) leads to a more stable behavior of the quantum magnetotransport and sheds a new light on the spin-splittings and its consequences in DQWs [8]. The measurements have been repeated for three different electron densities. The density has been increased by illuminating the sample with an

infrared LED using the same procedure as described in *Chap.* 4. Again increasing the density meant an improvement of the data. Several peculiarities have been observed in the data like the damping of the $\nu = 3$ minimum and local transformations of resistance peaks with increasing $B_{\|}$. So far only the suppression of the $\nu = 1$ state was known [9]. We will try to explain these peculiarities from calculated Landau level fans. We will also present data taken on a $In_xGa_{1-x}As/GaAs$ - SQW and observe that in this case the above mentioned peculiarities are absent, meaning that they can only be explained by the unique DQW-properties. Finally a curious phenomenon of different nature that showed up in our measurements will be mentioned.

7.2 Theoretical background

The most important consequence of splitting a SQW into a DQW by barrier insertion is the splitting of an energy level in the SQW into two energy levels for the DQW: the symmetric state and the anti-symmetric state (we assume that only one subband lies below the Fermi level). This splitting leads to the tunneling gap (Δ_{SAS}) and is dependent on the width of the barrier (See *Fig*. 7.1). So by changing the barrier width one can tune the magnitude of Δ_{SAS} [10].

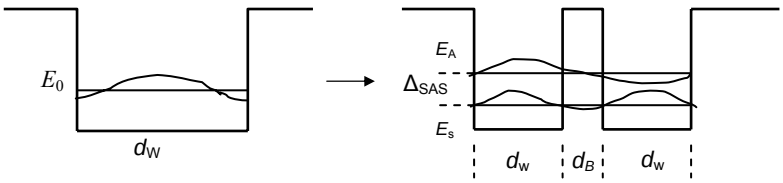

Figure 7.1 Splitting of the lowest energy subband into symmetric and an anti-symmetric subband after barrier insertion.

This subband splitting can also be represented in k - space. Below (*Fig*. 7.2) we see the splitting of the energy dispersion surface for a parallel magnetic field component ($B_{\|}$) equals to zero.

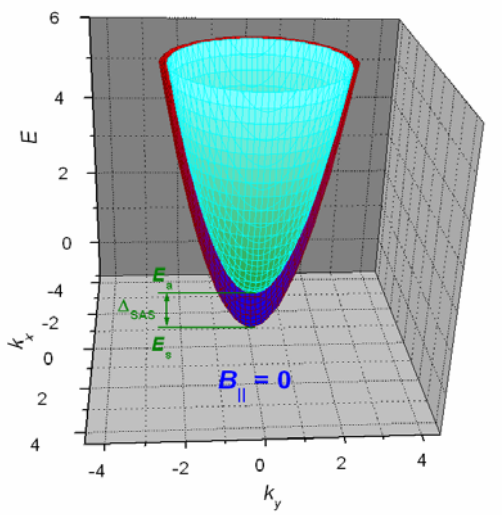

Figure 7.2 Splitting of the energy dispersion surface in *k*-space as a consequence of barrier insertion.

One has to keep in mind that as long as both subbands (E_S and E_A) are below the Fermi-level, tunneling between the quantum wells happens via both of the subbands. One can say that the quantum wells are connected by two channels. Central to the work presented in this chapter is the effect of a parallel field component on the subband structure and its subsequent effect on the magnetotransport. Let us first look at the effect on the energy dispersion paraboloids (*Fig*. 7.3).

What we observe in *Fig*. 7.3a) is that under influence of $B_{||}$ the energy dispersion paraboloids display an opposite shift in the k_y – direction. This leads to an anticrossing of the two surfaces resulting in an inner subband, also called “the lens”, and an outer subband, due to its shape also referred to as “the peanut” [11]. Between the lowest point of the lens and the saddle point visible in the peanut an energy gap appears. This constitutes the tunneling gap. The electron orbits are determined by the crossing of the energy subbands with the Fermi-surface. From *Fig*. 7.3b) it becomes clear that we can distinguish between three different situations. In the lowest image $B_{||} = 0$. Here both subbands are below the Fermi level, both subbands occupy both quantum wells and tunneling can happen via both subbands. In the middle image the lens is above the Fermi level. Still the Fermi level is within the tunneling gap and tunneling can occur via the peanut. Both quantum wells are still coupled. In the upper image the Fermi level lies below the tunneling gap.

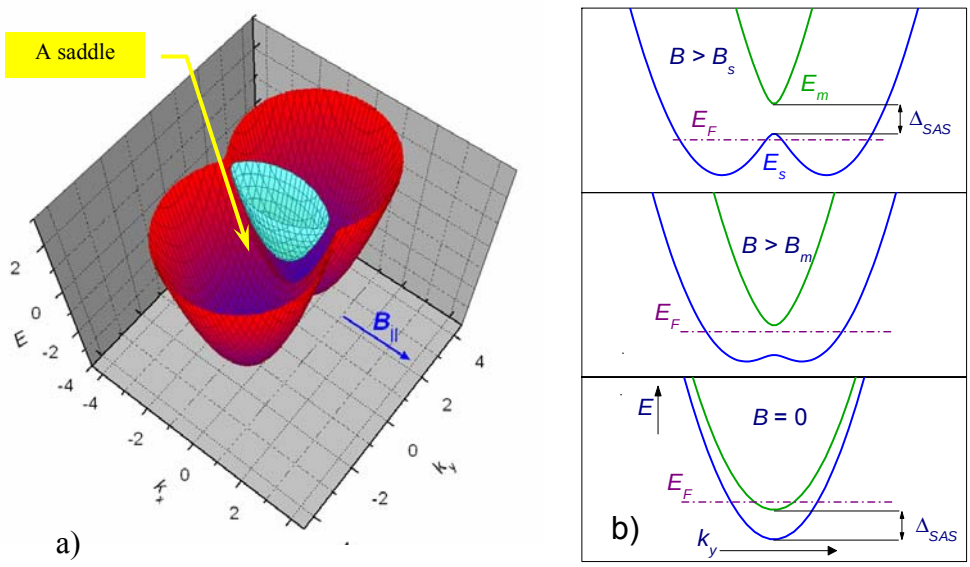

Figure 7.3 a) Effect of parallel field component on energy dispersion surfaces of E_s and E_A. b) vertical cross-section of the energy dispersion paraboloids under influence of an increasing parallel magnetic field component.

The effective orbit is now reduced from a peanut to two separate circular orbits (Fermi level lies also below the saddle point) and the quantum wells are now decoupled. Tunneling becomes impossible. In trying to understand this process of decoupling, just by picturing single electrons, it might be helpful to think of the following. Just imagine an electron tunneling from one quantum well to the other. An increasing $B_{\|}$ will cause a Lorentz force that works perpendicular on the pathway of the electron, thus making it difficult for the electron to reach the other well. As $B_{\|}$ further increases the electron gets more and more hindered in making the crossing and finally becomes localized in one of the quantum wells. The energy dispersion paraboloids mentioned above can be described by the following formula [3]:

$$E_{1,2} = \frac{\hbar^2(k_x^{\,2} + k_y^{\,2})}{2m} + \frac{E_S + E_A}{2} \pm \frac{1}{2}\sqrt{\Delta_{SAS}^{\,2} + (2\hbar \frac{eB_x d}{m} k_y)^2} \qquad (7.1)$$

Where $B_x = B_{\|}$, d is the interlayer distance, E_S and E_A are the edges of the two subbands with respect to the Fermi level and $m = 0.058\ m_0$ is the effective electron mass. *1* and *2* as subscripts of E indicate the symmetric and anti-symmetric subband, one of which is calculated by adding the last component of *Eq. 7.1* and the other by substracting the same component.

As usual the perpendicular component of the magnetic field ($B_\perp$) will result in Landau quantization of both of the subbands. In a quasi-classical way this can be calculated as follows.

$$N_M(E) \equiv \oint k_x(E_M, k_y)dk_y / 4\pi^2 = \frac{eB_\perp}{h}(N + \frac{1}{2}), N = 0,1,2,... \qquad (7.2)$$

Here $N_M(E)$ is the number of states within the area of the E_M projection to the (k_x, k_y) -plane. The integral taken is the contour integral of *Eq. 7.1* where k_x is expressed as a function of E_M and k_y. The component between brackets indicates the Landau level number. The Landau quantization of the energy dispersion paraboloid is shown in *Fig.7.4*. This Landau quantization occurs for both of the subbands: the lens and the peanut.

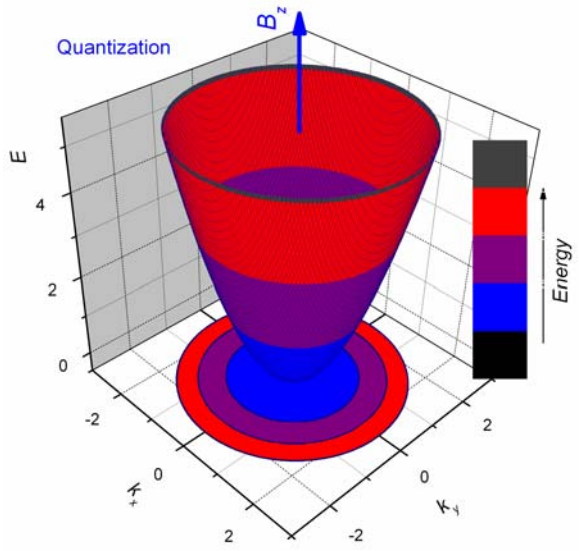

Figure 7.4 Landau quantization of the energy dispersion paraboloid under influence of a perpendicular magnetic field. Each sector on the (k_x, k_y)-plane represents a Landau level and contains an equal number of states: eB_z / h.

After calculating the Landau level splitting using *Eq*. 7.1 and 7.2, the spin splitting of the Landau levels can be added using

$$\pm\frac{1}{2}g^{*}\mu_{B}B \tag{7.3}$$

where g^* is the Landé g-factor, μ_B is the Bohr magneton and B is the total magnetic field. An example of the evolution of the Landau levels under an increasing magnetic field for a DQW is shown below. The three relevant energy gaps are displayed here.

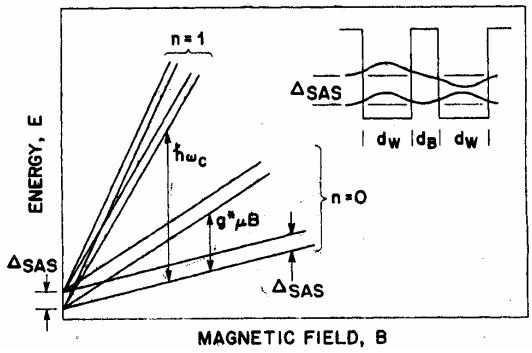

Figure 7.5 Landau level fan for a DQW. Notice the three different energy-gaps present. The tunneling gap (Δ_{SAS}), the cyclotron splitting ($\hbar\omega_c$) and the spin splitting ($g^*\mu_B B$) [1].

The spin-splitting ($g^*\mu_B B$) increases with increasing total magnetic field. The tunneling gap (Δ_{SAS}) can be influenced by $B_{\|}$, the cyclotron splitting ($\hbar\omega_c$) is influenced only by $B_{\perp}$.

7.3 Experimental aspects.

Having to measure magnetotransport in a DQW under a tilted magnetic field also adds a new dimension to the experimental setup. It means that one should be able to rotate the sample with respect to the magnetic field and be able to cover the necessary angular range. All this should be done with a certain angular resolution and accuracy. As one can easily picture, this will create additional problems to the wiring of the sample and thermally connecting it to that part of the setup of which the temperature can be regulated. In our case this will be the mixing chamber of the dilution refrigerator. The rotation aspect has been dealt with by mounting a so called Swedish rotator to the mixing chamber (*Fig. 7.6*).

Figure 7.6 Sample holder with sample mounted inside the cup of the Swedish rotator. This cup can be rotated 270 degrees with respect to the initial position shown here. This can be done with a resolution of 0.2 degree.

With the aid of an electrical control system the cup of the Swedish rotator visible in *Fig. 7.6* can be rotated 270 degrees with respect to the initial position shown. This can be done with a resolution of 0.2 degrees and an accuracy of the same value. The cup is made of a synthetic material to prevent eddy-current generation due to the changing magnetic field. Thermally connecting the sample holder with the mixing chamber has been done by a bundle of very flexible thin copper wires. This bundle of wires had to be thick enough to create a proper heat transfer and flexible enough to resist the torsion generated by the Swedish rotator. Both conditions where met by using so called "Lytze-wire". The cup offered enough possibilities to put all the wiring through. Having this initial conditions one should be able to probe the whole ($\rho_{xx,xy}$, $B_{\|}$, $B_{\perp}$) surface, where the magnitude of $B_{\|}$ and $B_{\perp}$ depend on the total magnetic field that one's setup can reach. An example of such a surface is given in *Fig. 7.7* for ρ_{xx}. Now there are two ways of doing the measurements. In the first one the magnetic field is fixed and the sample is rotated continuously. In the second one the angle is fixed and the magnetic field is swept continuously. The initial plan included the first option, since this allows one to get much more data points of the (ρ, $B_{\|}$, $B_{\perp}$) surface in the same amount of time (it takes less time to rotate the sample over and over, than to sweep the magnetic field over and over at a reasonable sweep rate). We had to abort

this initial plan however due to an unexpected factor. Rotating the sample at a reasonable rate caused a heating of the sample of up to 5 K above set temperature.

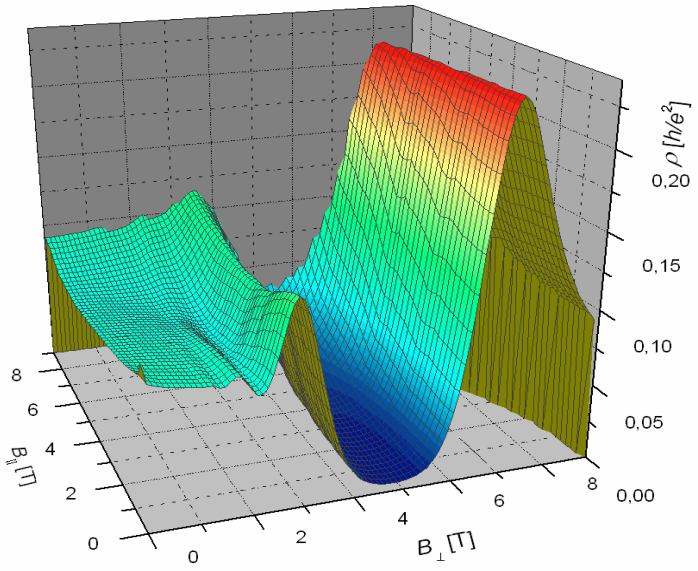

Figure 7.7 (ρ_{xx}, $B_{\|}$, $B_{\perp}$) surface measured with the technique described before, where the maximum total field is 9 T [12].

So finally a set of fixed angles has been determined and for each angle the magnetic field has been swept up to 16 T. The angles where chosen in such a way as to probe the most relevant features of the (ρ, $B_{\|}$, $B_{\perp}$) - surface. 0° is defined as the Hall bar being perpendicular to the magnetic field and for 90° the Hall bar is parallel to the magnetic field. The resistivities were measured using lock-in amplification. Next to the sample an infrared LED has been mounted enabling us to illuminate the sample and increase the electron density.

7.4 Double quantum well: results

The experiments described in this section where done on an $In_xGa_{1-x}As/GaAs$ DQW, where x = 0.2. The quantum wells are 5 nm in width and the barrier is 10 nm wide. The heterostructure has been symmetrically doped in both GaAs surroundings with 19nm

spacers. The electron density in the DQW can be tuned by illuminating the Hall bar. In the dark (without illumination) $n_e = 2.3 \times 10^{15}$ m^{-2}. This sample has been named: 3982. The sample is the same as in *Ref.* [12]. The energy profile is shown in *Fig.* 7.8.

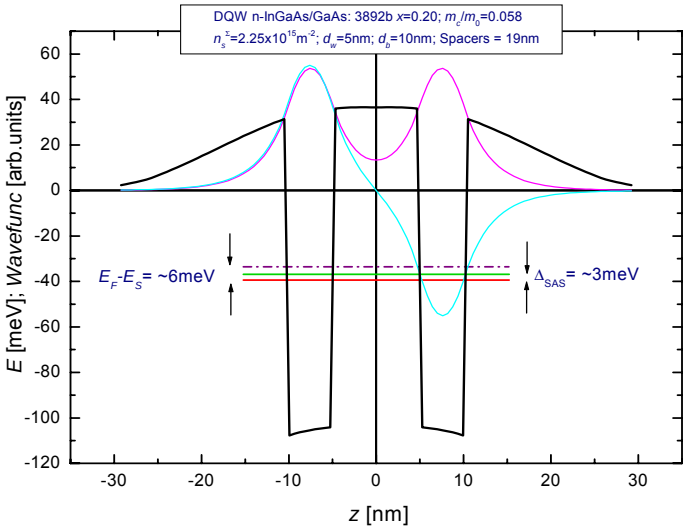

Figure 7.8 Energy profile of DQW, sample 3982.

We observe the symmetric and anti-symmetric subbands. The lowest energy level belongs to the symmetric subband. As common for Hallbars with tunable electron density, the quality of the data improves with improving density. A drawback is that the transitions will occur at higher magnetic fields for the higher densities, so the highest transitions cannot be studied for increasing tilt of the sample. On the other hand the lower transitions will become more pronounced and can be studied in more detail. The measurements where taken at a set temperature of 50 mK. The current used was 5 nA. In *Fig.* 7.9 the ρ_{xx} - data is presented for the lowest density measured for various (increasing) angles, which corresponds to increasing $B_{\|}$. For clarity the curves have been shifted vertically with respect to each other.

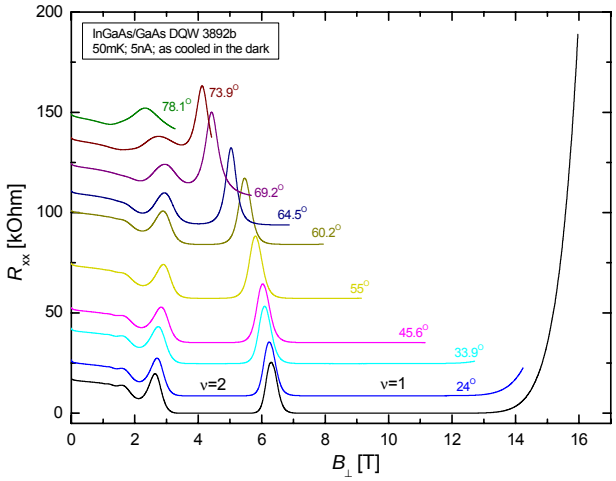

Figure 7.9 ρ_{xx} – data for several tilts of the Hallbar with respect to the magnetic field. The lowest curve is taken for the sample in perpendicular position with respect to the magnetic field. The highest is taken at an angle of 78.1°. $n_e = 2.3 \times 10^{15}$ m^{-2}

One very important feature to notice is the vanishing of the $\nu = 2$ minimum. Illuminating the sample led to the second density measured. Results are shown in *Fig*. 7.10.

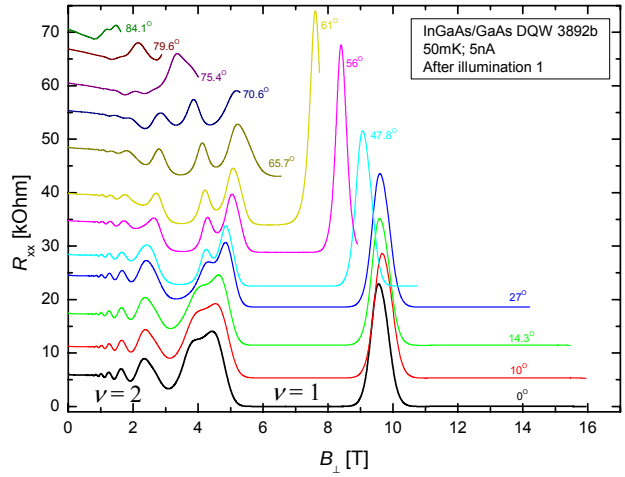

Figure 7.10 ρ_{xx} – data for several angles of the Hallbar with respect to the magnetic field after the first illumination. The lowest curve is taken for the sample in perpendicular position with respect to the magnetic field. The highest is taken at an angle of 84.1°. $n_e = 3.3 \times 10^{15}$ m^{-2}

Again we observe the vanishing of the $\nu = 2$ minimum and the appearing of the $\nu = 3$ minimum for increasing $B_{\|}$, showing that this minimum is due to spin splitting. After these series of measurements for the second density we proceeded to illuminate the sample to saturation density (n_e =5.1 × 10^{15} m^{-2}). The results for the ρ_{xx} – curves at different angles are shown in *Fig*. 7.11 below.

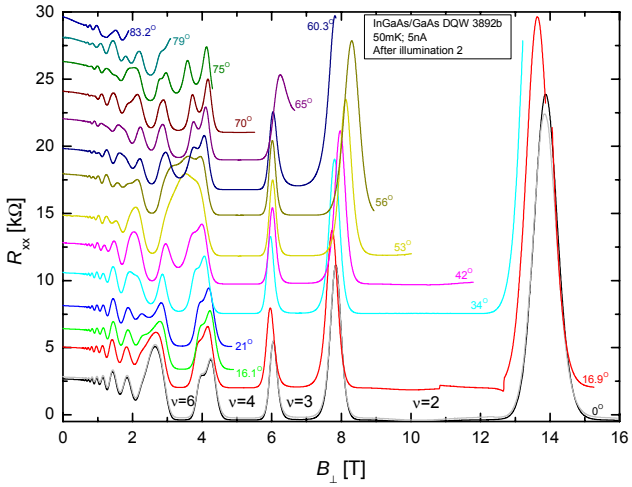

Figure 7.11 ρ_{xx} – data for several angles of the Hallbar with respect to the magnetic field after the second illumination. The lowest curve is taken for the sample in perpendicular position with respect to the magnetic field. The highest curve is taken at an angle of 83.2°. n_e =5.1 × 10^{15} m^{-2}.

The $\nu = 1$ minimum is not visible anymore. The $\nu = 2$ minimum is visible up to 34°. The $\nu = 3$ minimum for this density is already present at 0°. We observe an interesting peculiarity concerning this minimum. First its width appears to increase until 56°. For higher angles the width decreases. Also the $\nu = 6$ minimum behaves in an odd way for increasing angle. According to our initial claim the peculiarities observed in the data presented in this paragraph are inherent to the DQW and as such should not be observed in a SQW for comparable experimental and sample conditions. This will be elaborated in the next paragraph.

7.5 Comparison of the double quantum well and the single quantum well.

In this paragraph we will compare the results obtained from the DQW with the results obtained from the SQW under similar conditions. This sample has been named #2982. The measurements on the SQW where performed for four different densities, trying to match the densities measured in the DQW. The calculated energy profile of the SQW in shown below in *Fig*. 7.12.

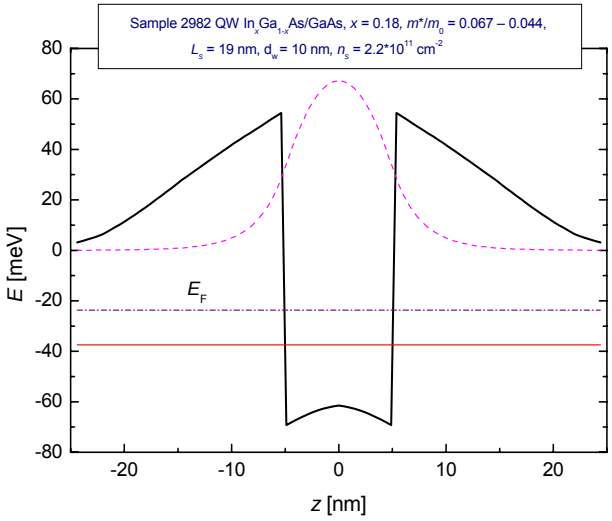

Figure 7.12 Energy profile of SQW, sample 2982.

The width of the SQW is 10 nm, which corresponds to the total well-width in the DQW. The width of the spacers is again 19 nm and the initial density $n_e = 2.2 \times 10^{15}$ m^{-2}. The value x = 0.18 is comparable to x = 0.20 of the DQW. Notice the single subband below the Fermi level in contrast of the two subbands for the DQW (*Fig*. 7.8). Other evidence for the number of filled subbands can be obtained from the Shubnikov-the Haas (SdH) oscillations in the low field regime. One filled subband corresponds to one period in the oscillations. Several interfering periods denote several filled subbands. In *Fig*. 7.13 on the next page the SdH- oscillations for both the SQW and the DQW are displayed. Notice that for the SQW there is only one period, while for the DQW several interfering periods are visible. The

number of individual subbands and their densities follow from the FFT of the longitudinal resistivity vs. the reciprocal magnetic field (not displayed here).

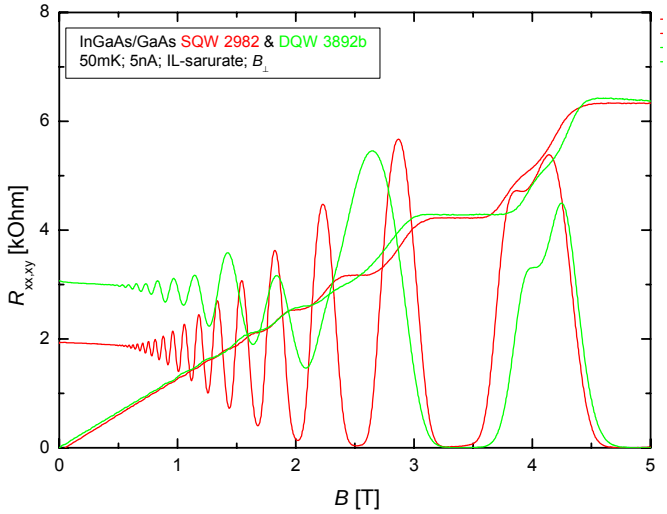

Figure 7.13 SdH-oscillations for both the SQW (red curve) and the DQW (green curve).

Next we consider the resistivity curves for the SQW for different angles of the Hallbar with respect to the magnetic field. On the next page the case for the second measured density (n_e = 2.62 x $10^{15}m^{-2}$) is shown (*Fig.* 7.14). The $\nu = 3$ minimum becomes more pronounced with increasing $B_\parallel$ as a consequence of the spin splitting of the Landau level. However, we don't observe the peculiarities observed for the DQW, like the vanishing of the $\nu = 2$ minimum. For the DQW at 61° this minimum has half of its width at 0° (*Fig.* 7.10), where in the SQW the width at 60° has hardly changed compared to the width at 0°.

Next we consider the resistivity curves for the highest measured density: n_e = 4.76 x $10^{15}m^{-2}$ (*Fig.* 7.15). At this density the $\nu = 3$ minimum is already fully present at 0° tilt. Now the $\nu = 5$ minimum gets induced with increasing tilt. Again for this density we do not observe any of the DQW peculiarities. The width of the minima does not change. There is no vanishing of any minimum and there is no irregular behavior in the width of the minima, like for the $\nu = 3$ minimum of the DQW. Also no minimum of the SQW displays the odd behavior of the $\nu = 6$ minimum of the DQW (*Fig.* 7.11).

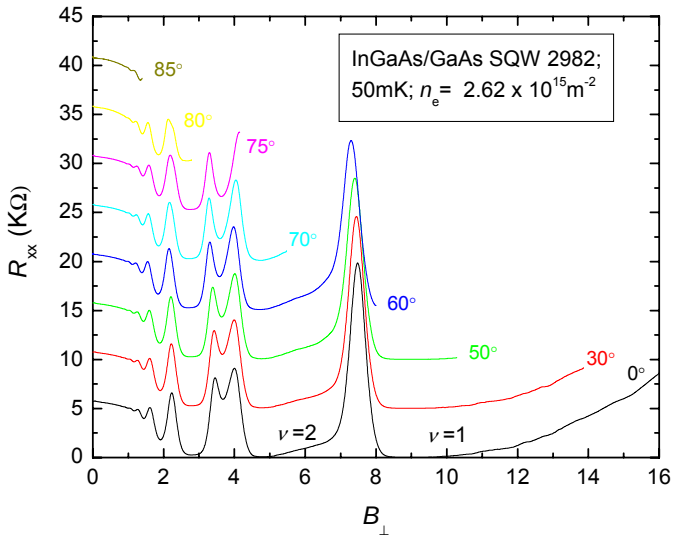

Figure 7.14 ρ_{xx} – data for several angles of the Hallbar with respect to the magnetic field after the first illumination (n_e = 2.62 x $10^{15}m^{-2}$). The lowest curve is taken for the sample in perpendicular position with respect to the magnetic field. The highest curve is taken at an angle of 85°.

This is evidence for the assumption that the observed peculiarities in the R_{xx} curves of the DQW are related to the intrinsic aspects of the DQW. An explanation for this, making use of the LL-structure of the DQW, will be given in section 7.6.

According to *Fig*. 7.3 another phenomenon can be expected as a consequence of the increasing parallel magnetic field, namely the depopulation of the lens subband. This happens in the transition from the lowest to the middle picture in *Fig*. 7.3b. Related to this process a dip becomes visible in the R_{xx} data [13,14]. In *Fig*. 7.16 we compare the SQW and the DQW for increasing $B_{\|}$. The angle of the sample with respect to the magnetic field is 90°, so there is no perpendicular component present.

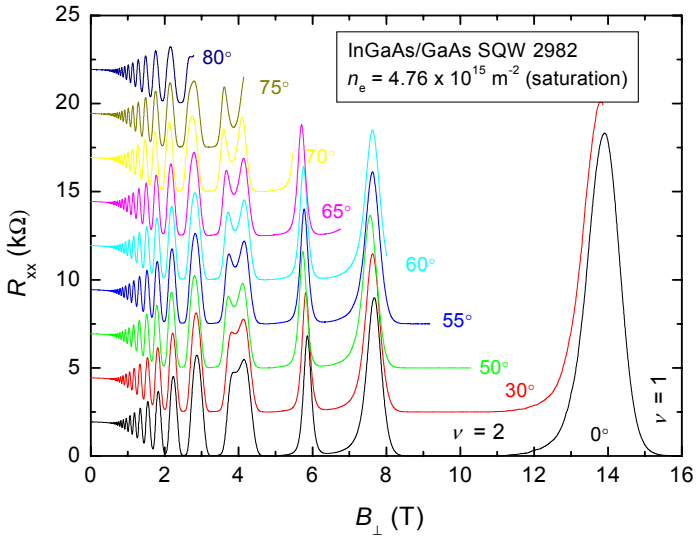

Figure 7.15 ρ_{xx} – data for several angles of the Hallbar with respect to the magnetic field after the third and final illumination (n_e = 4.76 x 10^{15}m^{-2}). Saturation density has been reached. The lowest curve is taken for the sample in perpendicular position with respect to the magnetic field. The highest curve is taken at an angle of 80°.

In *Fig*. 7.16a) both R_{xx} and R_{xy} are shown at saturation density. It is interesting to notice that the value of R_{xy} remains zero, meaning that there is no perpendicular component of the magnetic field present. R_{xx} increases monotoneously, suggesting a reduction in the conductivity of the 2DEG. This is related to the increased localization of the electrons due to $B_{\|}$. In *Fig*. 7.16b) we see a different scenario. Here for all three densities a minimum in the R_{xx} curves is observed, indicating the depopulation of the antisymmetric subband. This minimum shifts to the right with increasing density. This makes sense if assume that depopulation of a subband occurs at higher values of $B_{\|}$ for higher densities.

In the next section we will try to explain the DQW peculiarities by looking at how the Landau levels evolve as function of the magnetic field.

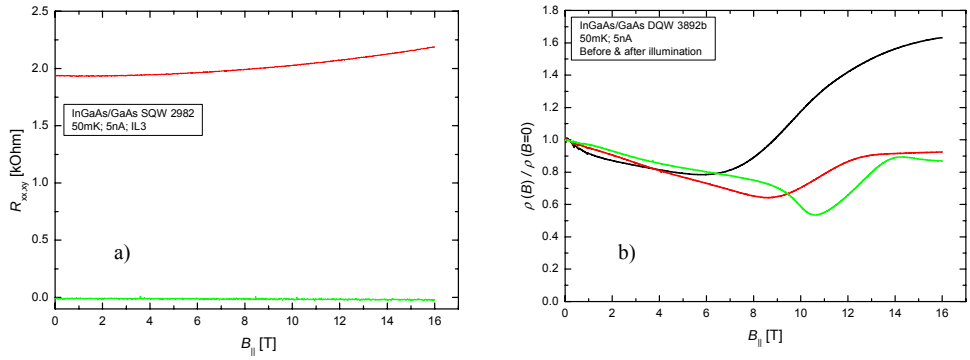

Figure 7.16 Resistance data as function of an increasing $B_{\|}$, when no $B_{\|}$ is present for a) the SQW at saturation density (n_e = 4.7 × 10^{15} m^{-2}) and b) the DQW for three densities (n_e = 2.3 × 10^{15} m^{-2} , 3.3 × 10^{15} m^{-2} and 5.1 × 10^{15} m^{-2}). For the SQW also R_{xy} is visible (flat line). Notice how its value remains zero, indicating that no perpendicular component is present.

7.6 Unique aspects of the double quantum well revised.

In order to understand the unique aspects observed in the resistivity curves of the DQW it is important to understand the nature of the transitions. From *Fig.* 7.5 for instance it is clear that there are three types of transitions possible. One between two Landau levels of the same subband whether or not they have the same spin-polarity. One between the two spin-splitted components of a Landau level and one between Landau levels of the two subbands. The same transition can belong to each of these three categories, dependent on how the Landau levels of the subbands are situated with respect to each other. It is exactly this aspect that is influenced by the parallel magnetic field component. By substituting *Eq*. 7.1 into *Eq*. 7.2, *LL*-fans have been calculated for our DQW for different values of $B_{\|}$. In the following we will show the calculated *LL*-fans, the cross sections of the energy dispersion paraboloids (*Eq.* 7.1) for k_x equals zero, the cross sections at the Fermi level and the measured data for the $B_{\|}$ values of 0, 6 and 15 T. There is no one to one correspondence between the measured data and the calculated LL fans, since in the former the angle is kept

constant (so $B_\parallel$ also increases with increasing magnetic field) and in the latter the value of $B_\parallel$ is kept constant. Still we will try to make this match as good as possible.

Below (*Fig*. 7.17) the situation for $B_\parallel = 0$ and zero tilt is shown. The data shown is for the highest measured density.

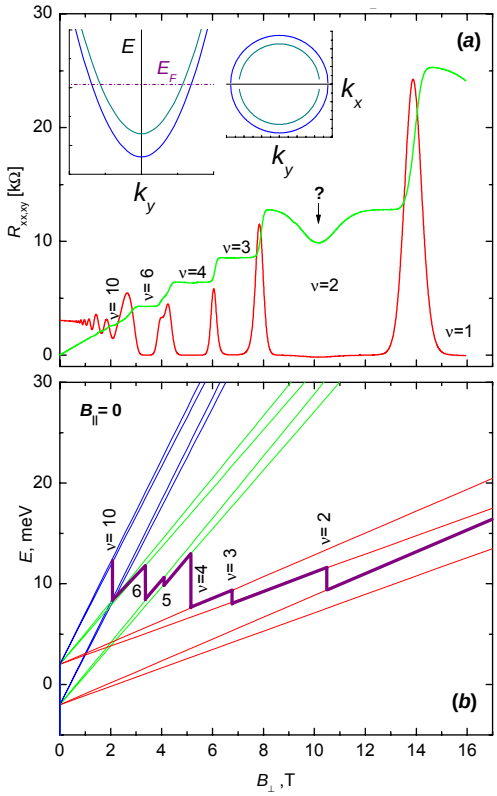

*Figure 7.17*a) Measured resistivities of the DQW for zero tilt and the highest density. Inset shows the cross sections of the energy dispersion paraboloids for $k_x = 0$ (left) and at the Fermi surface (right). b) Calculated *LL*-fans for $B_\parallel = 0$. The displayed LL's are $\nu = 1$, 2 and 3 for both subbands. The thick line indicates the Fermi level. Figure taken from Ref [15].

At $B_\parallel = 0$ there is no shift of the energy dispersion paraboloids and the surfaces for both subbands are equally centered as shown in the inset. The thick line in *Fig*. 7.17 b) is drawn by hand and represents the Fermi energy level 'moving' through the LL's. The value of E_F

has been calculated by substituting the value for the Fermi-wave vector $k_F = \sqrt{2\pi \cdot n_{2D}}$ in *Eq*. 7.1. In *Fig*. 7.18 below the same is shown for the cases of $B_{\|}$ = 6 T and a tilt of 56° (left) and 15 T and a tilt of 65° (right). For the case of $B_{\|}$ = 15 T, ρ_{xx} as function of a pure $B_{\|}$ is shown in the inset.

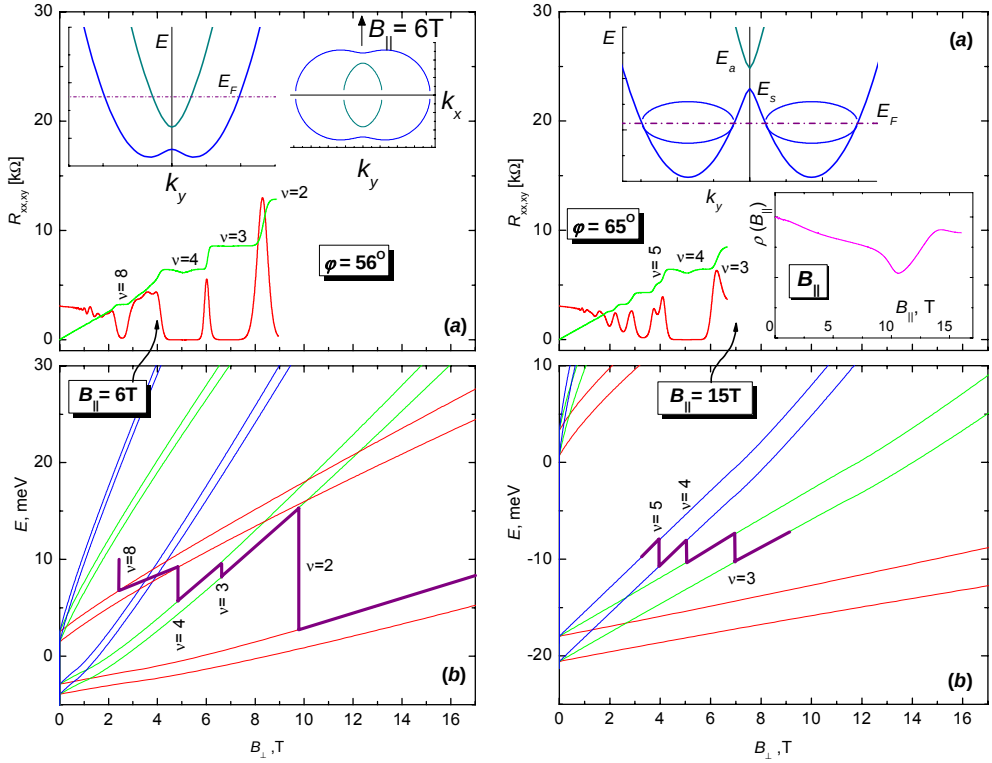

Figure 7.18 idem as *Fig*. 7.17 but for $B_{\|}$ = 6 T and a tilt of 56° (left) and $B_{\|}$ = 15 T and a tilt of 65° (right). Figure taken from Ref. [15].

The first thing to notice in *Figs*. 7.17 and 7.18 is how the nature of the $\nu = 3$ minimum changes with increasing $B_{\|}$. For $B_{\|} = 0$ the $\nu = 3$ minimum lies between two spin splitted LLs of the antisymmetric subband (*Fig*. 7.17b). For $B_{\|}$=0 the same minimum lies between two spin splitted LLs of the symmetric subband. For $B_{\|}$=15 T the $\nu = 3$ minimum lies between the same two spin splitted LLs of the symmetric subband. The gap is now bigger because of the increased $B_{\|}$=15 T. This changing of the LL configuration regarding the ν=

3 minimum explains the behavior we observe in the ρ_{xx}-curves for this minimum in the DQW (*Fig*. 7.11). The remarkable behavior of the $\nu = 6$ minimum (*Fig*. 7.11) can be explained because of the complicated pattern that arises in the LL pattern around 4 T, with increasing $B_{\|}$ (*Fig*. 7.18 left). The vanishing of the $\nu = 2$ minimum visible in *Fig*. 7.9 and 7.10 is probably explained by the separation of the symmetric and antisymmetric subband. This quasi-classical approach however has its limitations especially for high values of $B_{\|}$. A more accurate analysis of the magnetic level pattern can be done using a quantum mechanical approach [16].

7.7 An unexpected peculiarity

In addition to the above mentioned typical behavior of the DQW we observed another phenomenon that is very remarkable. It turned out that in the middle of the even numbered plateaus $\nu = 2$ and 4 a dip occurs. This dip decreases in size with increasing $B_{\|}$ for the $\nu = 2$ plateau, but increases in size with increasing $B_{\|}$ for the $\nu = 4$ plateau. This could not be explained by a sudden failure in the measuring circuit like a local increase in the out of phase signal. This behavior is visible in *Fig*. 7.17 and 7.18 and is displayed in more detail below in *Fig*. 7.19.

This behavior has been observed for all three the measured densities of the DQW and is again completely absent in the SQW (*Fig*. 7.20).
Notice how the dip is well pronounced at the $\nu = 2$ plateau, but completely absent at the $\nu = 4$ plateau for a pure perpendicular magnetic field. This behavior might be explained by the reentrant QHE [17].

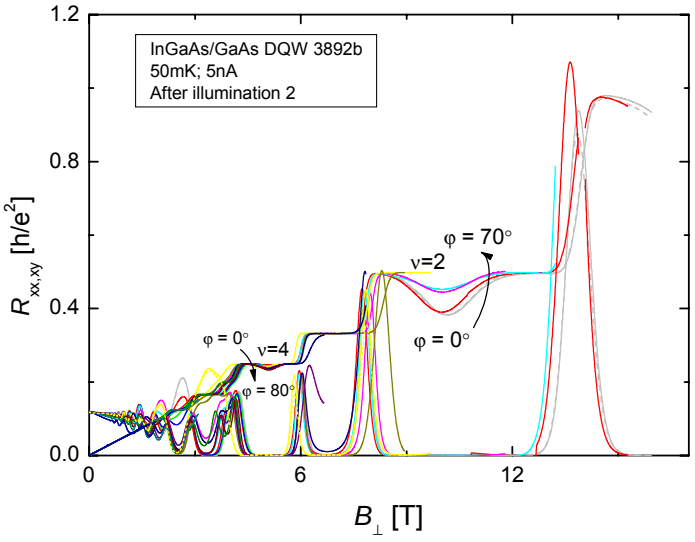

Figure 7.19 ρ_{xx} and ρ_{xy} – data of the DQW for the highest measured density for increasing $B_{\|}$. Notice the dip in the even plateaus $\nu = 2$ and 4 and how the size of this dip changes with changing $B_{\|}$.

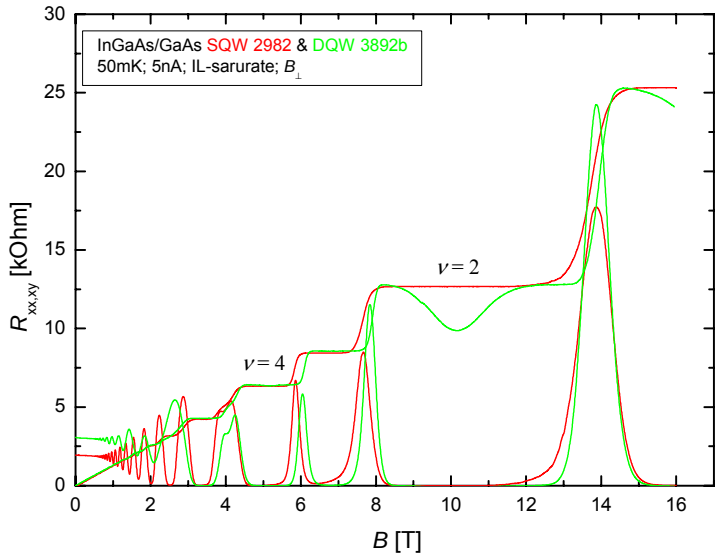

Figure 7.20 Comparison of the SQW and the DQW for pure $B_\perp$. Both have reached saturation density.

7.8 Conclusions

Magnetrotransport measurements have been carried out on an $In_xGa_{1-x}As$/GaAs DQW with a large Landé *g*-factor ($g \approx 3$) for three different electron densities. The results are compared with magnetotransport data taken on an $In_xGa_{1-x}As$/GaAs SQW with comparable characteristics. The main results of our study can be summarized as follows:

- The heterostructure used with $g \approx 3$ gave a well pronounced spin splitting of the Landau levels, which is not due to the exchange enhancement caused by the local magnetic field.
- The DQW-data display peculiarities that are absent in the SQW-data and can be explained only by the unique aspects of the DQW. These peculiarities are: (*i*) vanishing of the $\nu = 2$ minimum with increasing $B_{\|}$, (*ii*) a non-uniform behavior of the $\nu = 3$ minimum (first a broadening then a narrowing) with increasing $B_{\|}$, (*iii*) an irregular behavior of the $\nu = 6$ minimum with increasing $B_{\|}$ and (*iv*) a dip that occurs in the $\nu = 2$ and 4 plateaus of the DQW and of which the size changes with changing $B_{\|}$.
- The first three peculiarities can be explained by the quasi-classical Landau level pattern for the DQW. The last peculiarity has been attributed to the reentrant QHE.
- In order to further elucidate the typical features of DQW physics more extended calculations, notably quantum mechanical calculations of the Landau level patterns, are required [18].

7.9 References

[1**]** G.S. Boebinger, H.W. Liang, L.N. Pfeiffer and K.W. West, *Phys. Rev. Lett.* **64** (1990) 1793.

[2] A. macDonald, P.M. Platzman and G.S. Boebinger, *Phys. Rev. Lett*. **65** (1990) 775.

[3] G.S. Boebinger, A. Passner, L.N. Pfeiffer and K.W. West, *Phys. Rev. B* **43** (1991) 12673.

[4] D. Yoshioka, A. macDonald and S.M. Girvin, *Phys. Rev. B* **39** (1989) 1932.

[5] S.M. Girvin and A. macDonald, *perspectives in quantum Hall effect*, Eds. S.D. Sarma and A. Pinczuk, Wiley, N.Y., pp161-224 (1997).

[6] S.K. Lyo, *Phys. Rev. B* **50** (1994) 4965.

[7] J. A. Simmons, S. K. Lyo, N. E. Harff, and J. F. Klem, *Phys. Rev. Lett.* **73** (1994) 2256.

[8] T.P. Smith and F.F. Fang, *Phys. Rev. B* **35** (1987) 7729.

[9] S.Q. Murphy, J.P. Eisenstein, G.S. Boebinger, L.N. Pfeifer and K.W. West, *Phys. Rev. Lett*. **72** (1994) 728.

[10] N. E. Harff, J. A. Simmons, S. K. Lyo, J. F. Klem, G. S. Boebinger, L. N. Pfeiffer and K.W. West, *Phys. Rev. B* **55** (1997) 13405.

[11] N. E. Harff, J. A. Simmons, S. K. Lyo, J. F. Klem, G. S. Boebinger, L. N. Pfeiffer and K.W. West, *Physica E* **1** (1997) 185.

[12] M.V. Yakunin, 14th Int. Symp. "Nanostructures: Physics and Technology", Ioffe Institute (2006) 77.

[13] M.V. Yakunin, G.A. Al'shanskii, Yu. G. Arapov, V.N. Neverov, G.I. Kharus, N.G. Shelushinina, B.N. Zvonkov, E.A. Uskova, A. de Visser and L. Ponomarenko, *Semiconductors* **39** (2005) 107.

[14] M.A. Blount, J.A. Simmons and S.K. Lyo, *Phys. Rev. B* **57** (1998) 14882.

[15] M.V. Yakunin, G. Galistu and A. de Visser, 15th Int. Symp. "Nanostructures: Physics and Technology", Ioffe Institute (2007).

[16] J. Hu and A. macDonald, *Phys. Rev. B* **46** (1992) 12554.

[17] G. A. Csáthy, J. S. Xia, C. L. Vicente, E. D. Adams, N. S. Sullivan, H. L. Stormer, D. C. Tsui, L. N. Pfeiffer and K. W. West, *Phys. Rev. Lett*. **94 (**2005) 146801.

[18] M.V. Yakunin, A. de Visser, G. Galistu, S.M. Podgornykh, Yu.G. Sadofyev, N.G. Shelushinina and G.I. Harus, *J. Phys. Conf. Series* **150** (2009) 022100.

Summary

The work described in this thesis consists of two parts. The first and main part is dedicated to a magnetotransport study of the scaling of the integer quantum Hall effect, with an emphasis on probing the irrelevant critical behavior (*Chaps*. 3-5). The second part (*Chaps*. 6-7) is devoted to a magnetotransport study of quantum wells with a thin barrier and bi-layer quantum wells.

After an introduction of the quantum Hall effect (Chapter 1) and a summary of the theoretical aspects related to scaling (Chapter 2), we first describe the experimental technique used to measure the 2DEG in Hall bar samples in the high-ohmic regime (Chapter 3). Especially we describe a newly implemented dc-technique, which turned out to improve the measurement accuracy when compared to the traditional ac-technique. This is of particular importance for magnetotransport data taken in high magnetic fields, where the resistance of the samples rapidly increases in the regime of the plateau-insulator transition.

In Chapters 4 and 5 we report a scaling study carried out on a InGaAs/GaAs quantum well prepared with a relatively broad conduction channel as to reduce the total resistance of the Hall bar in high magnetic fields. The electron density of the 2DEG could be tuned by illumination and ranges from n_e= 1 to 2×10^{15} m^{-2}. Consequently, the plateau-insulator (PI) transition occurs in the magnetic field range 7.7-14.8 T. This work strongly builds on - and expands - the experimental scaling studies carried out previously at the Van der Waals-Zeeman Institute by De Lang and Ponomarenko on similar samples.

In Chapter 4 we focus on the characterization of the InGaAs/GaAs Hall bar by means of magnetotransport measurements. The gradient in the electron density along the bar is determined for four different electron densities by means of the method of "reflection symmetry" at the 2→1 plateau-plateau (PP) transition. The quality of the sample increases with increasing density. Next we investigate the relevant critical exponent κ extracted from the temperature variation of the longitudinal resistance at the PI transition. The deduced values κ = 0.43-0.53 are comparable to those obtained in previous studies. Numerical simulations are used to investigate the influence of density gradients on the value of κ. The

variation of κ is in part an experimental feature attributed to the remaining overlap of the Landau levels at the lower densities. On the other hand, the extracted κ values should be considered as "effective", because the scattering may exhibit long-ranged components with respect to the magnetic length.

In Chapter 5 we focus on the irrelevant critical exponent y_σ, which has been extracted from the deviations of the Hall resistance from the quantized value h/e^2. We have measured the Hall resistance using the dc-method for four different electron densities. A detailed analysis of the Hall data employing a new data collapse method results in y_σ ranging from 2.4 to 2.7 for the different electron densities. These values agree well with previously obtained values. However, in order to obtain a good data collapse it appeared necessary to apply a small temperature dependent shift of the data in the filling factor ν. The fact that the critical filling factor shows a small temperature variation underlines the high degree of macroscopic inhomogeneities in the sample. By using the universal scaling functions derived by Pruisken and the experimentally determined parameters for κ, y_σ and the characteristic temperatures T_0 and T_1 of the InGaAs/GaAs quantum well we construct the renormalization group flow diagram. This is the most important result obtained in this thesis. The flow diagram shows all the properties predicted for genuine scaling: relevant and irrelevant flow, the location of the critical point $(\sigma_H, \sigma_0) = (½e^2/h, ½e^2/h)$ and particle-hole symmetry. We stress that the determination of the flow diagram for the present sample is only possible through the determination of the conductivity tensor at the PI transition. Macroscopic sample inhomogeneities obstruct obtaining an accurate flow diagram from the conductivity tensor at the PP transition. Thus in order to unravel all facets of the arresting topic of scaling of the quantum Hall effect, progress can only be made after a complete understanding of the effect of macroscopic sample inhomogeneities.

In the remainder of the thesis quantum wells with a thin barrier and double layer quantum wells are investigated. In Chapter 6 we have investigated the energy spectrum of two sets of δ-doped GaAs/InGaAs/GaAs quantum wells, namely quantum wells with and without a thin central AlAs barrier. Our experimental probes are magnetotransport and photoluminescence. The experimental results were compared to numerical calculation of the energy levels and the wave function distributions. It turned out that the AlAs barrier can act as a phonon barrier and significantly changes the distance between the energy levels

and the spatial distribution of the wave functions. In addition, we found that the δ-doping regions act as V-shaped quantum wells and undesirably distort the wave functions. In order to relocate (confine) the wave functions in the central quantum well, a second series of samples was grown in which the V-shaped quantum wells were partly compensated by surrounding them with AlAs barriers. Unfortunately the electron density in the 2DEGs was not high enough to fill more than one subband and the desired improvement was not obtained for this second series of samples.

In Chapter 7 we have studied the effect of a tilted magnetic field on an $In_xGa_{1-x}As/GaAs$ bilayer quantum well with a large Landé *g*-factor. The large Landé *g*-factor is chosen to enhance spin-splitting effects. By performing magnetotransport measurements for different angles of the magnetic field with respect to the plane of the 2DEG, we can add a parallel component, $B_{\|}$, to the perpendicular magnetic field, while the effect of spin-splitting remains the same, i.e. one can study the effect of adding an in-plane magnetic field when the bilayer quantum well is tuned to a particular integer quantum Hall state. Magnetotransport data are taken on single (SQW) and double quantum wells (DQW) and compared with each other. The DQW data exhibit features that cannot be explained by the physics used to describe the SQW. These features are: (*i*) the $\nu = 2$ minimum disappears with increasing $B_{\|}$, (*ii*) the $\nu = 3$ minimum widens and narrows as a function of $B_{\|}$, (*iii*) the $\nu = 6$ minimum shows an irregular behavior with increasing $B_{\|}$ and (*iv*) an unexpected and still unexplained dip in the even integer plateaus of the Hall resistance. The first three features could be understood by an analysis of the calculated Landau Level fans. The latter feature is attributed to the reentrant quantum Hall effect.

Samenvatting

Dit proefschrift bestaat uit twee delen. Het eerste en tevens belangrijkste deel is gewijd aan een experimentele magnetotransport studie van het schalings-gedrag van het integer quantum Hall effect, met nadruk op het meten van het irrelevante kritische gedrag (*Hfdst.* 3-5). Het tweede deel (*Hfdst.* 6-7) is gewijd aan een magnetotransport studie van 'potentiaal putten (*quantum wells*)' met een dunne centrale (elektronen) barrière en aan *bi-layer quantum wells.*

Na een introductie van het quantum Hall effect (Hoofdstuk 1) en een samenvatting van de aan schaling ten grondslag liggende theoretische aspecten (Hoofdstuk 2), beschrijven we allereerst de experimentele techniek die gebruikt is om te meten aan het 2-dimensionale electron gas (2DEG) in samples met een Hall bar configuratie in het hoog-ohmische regime (Hoofdstuk 3). Er wordt hoofdzakelijk ingegaan op een recent door ons geïmplementeerde dc-techniek, die vergeleken met de traditionele ac-techniek, een verbeterde meetnauwkeurigheid bleek op te leveren. Dit is met name van belang voor magnetotransport metingen uitgevoerd bij hoge magneet velden, waar de weerstand van de samples snel toeneemt in het regime van de plateau-insulator overgang.

In de Hoofdstukken 4 en 5 beschrijven we een 'schaling studie' uitgevoerd op een InGaAs/GaAs *quantum well* met een relatief breed geleidingskanaal met als doel de totale weerstand van de Hall bar bij hoge magneet velden af te doen nemen. De electronen dichtheid van het 2DEG kon ingesteld worden door belichting en varieert van $n_e = 1$ tot 2×10^{15} m^{-2}. Dit betekent dat de plateau-insulator (PI) overgang plaatsvindt in het magneetveld bereik van 7.7 tot 14.8 T. Dit werk bouwt voort op – en is een uitbreiding van - de experimentele studies naar schaling eerder verricht op het Van der Waals-Zeeman Instituut door De Lang en Ponomarenko op vergelijkbare samples.

In Hoofdstuk 4 ligt de focus op het karakteriseren van de InGaAs/GaAs Hall bar d.m.v. magnetotransport metingen. De gradiënt in de elektronen dichtheid langs de Hall bar is voor vier verschillende elektronen dichtheden bepaald gebruik makende van de methode van ''reflectie symmetrie'' voor de $2 \rightarrow 1$ plateau-plateau (PP) overgang. De kwaliteit van de samples neemt toe met toenemende dichtheid. Vervolgens is onderzoek gedaan naar de

relevante kritische exponent κ zoals bepaald uit de temperatuur variatie van de longitudinale weerstand nabij de PI overgang. De hieruit afgeleide waarden van κ = 0.43-0.53 zijn vergelijkbaar met de waarden verkregen uit eerdere studies. Numerieke simulaties zijn gebruikt om de invloed van dichtheid gradiënten op de waarde van κ te bepalen. De variatie van κ is deels te verklaren doordat de Landau niveaus nog niet helemaal gescheiden zijn bij de laagste dichtheden. Aan de andere kant moeten de geëxtraheerde waarden van κ beschouwd worden als ‘‘effectief’’, omdat het scattering gedrag mogelijk componenten bevat die een grote reikwijdte hebben t.o.v. de magnetische lengte.

In Hoofdstuk 5 focussen we op de irrelevante kritische exponent y_σ, die is afgeleid uit de afwijkingen van de Hall weerstand van de integere plateau waarde h/e^2 bij toenemende temperatuur. De Hall weerstand is gemeten voor vier verschillende dichtheden gebruik makende van de dc-methode. Een gedetailleerde analyse van de Hall data, waarbij gebruik wordt gemaakt van een nieuwe methode van ‘data collapsen’ geeft waarden voor y_σ variërend van 2.4 tot 2.7 voor de verschillende elektron dichtheden. Deze waarden corresponderen goed met eerder verkregen waarden. Echter, voor het verkrijgen van een goede ‘data-collapse’ bleek het nodig te zijn om een temperatuur afhankelijke shift van de data uit te voeren in de vul factor ν. Het feit dat de kritische vul factor een kleine temperatuur afhankelijke variatie vertoont duidt op een hoge mate van macroscopische inhomogeniteiten in het sample. Door gebruik te maken van de universele schalings-functies zoals afgeleid door Pruisken en de experimenteel verkregen parameters voor κ, y_σ en de karakteristieke temperaturen T_0 en T_1 van de InGaAs/Gaas *quantum well* wordt het ‘renormalization group flow diagram’ geconstrueerd. Dit is tevens het meest belangrijke resultaat van dit proefschrift. In het ‘flow diagram’ komen alle eigenschappen terug die voorspeld zijn voor authentiek schalen: relevante en irrelevante flow, de plek van het kritische punt (σ_H, σ_0) = ($\frac{1}{2}e^2/h$, $\frac{1}{2}e^2/h$) en ‘particle-hole symmetrie. Het dient benadrukt te worden dat het bepalen van het flow diagram voor dit sample alleen mogelijk is door het bepalen van de geleidbaarheids tensor voor de PI overgang. Macroscopische inhomogeniteiten verhinderen het bepalen van een nauwkeurig flow diagram uitgaande van de geleidbaarheids tensor voor de PP overgangen. Dus voortgang in het ontrafelen van alle facetten van schalen binnen het quantum Hall effect kan alleen gemaakt worden nadat volledig begrip is verkregen omtrent macroscopische sample inhomogeniteiten.

In het resterende deel van dit proefschrift worden *quantum wells* met een centrale barrière en *bilayer quantum wells* onderzocht. In Hoofdstuk 6 is gekeken naar het energie spectrum van twee sets van δ-gedoopte GaAs/InGaAs *quantum wells*, te weten *quantum wells* met en zonder dunne centrale AlAs barriere. Onze experimentele sondes bestaan uit magnetotransport en fotoluminescentie metingen. De experimentele resultaten zijn vergeleken met numerieke berekeningen van de energie niveaus en de distributies van de golffuncties. Het is gebleken dat de AlAs barriere dienst doet als fononen barrière en de afstand tussen de energie niveaus en de ruimtelijke verdeling van de golffuncties aanzienlijk verandert. Bovendien is gebleken dat de δ-gedoopte gebiedjes als V-vormige potentiaal putjes ageren en de golffuncties op een ongewenste wijze vervormen. Om de golffuncties toch te beperken tot de centrale *quantum well* is een tweede serie samples gegroeid waarbij het effect van de V-vormige potentiaal putjes (deels) gecompenseerd is door deze te omgeven met AlAs barrières. Helaas was de electronen dichtheid in deze serie samples niet genoeg om meer dan een subband te vullen en kon de gewenste verbetering niet verkregen worden.

In Hoofdstuk 7 is gekeken naar het effect van een schuin invallend magnetisch veld op een $In_xGa_{1-x}As/GaAs$ bilayer *quantum well* met een grote Landé *g*-factor. Een grote Landé *g*-factor is gekozen om het effect van spinsplitsing te versterken. Door het uitvoeren van magnetotransport metingen voor verschillende hoeken tussen het magneetveld en het vlak van het 2DEG, is het mogelijk een parallelle veld component, $B_{||}$, toe te voegen aan het loodrechte magneet veld, terwijl het effect van spinsplitsing gelijk blijft. M.a.w. het is op deze manier mogelijk om het effect van het toevoegen van een parallelle component te bestuderen terwijl de *bilayer quantum well* in een bepaalde ‘integer quantum Hall’ toestand is gebracht door de loodrechte component van het magneetveld. Magnetotransport data verkregen van een *single* (SQW) en een *double quantum well* (DQW) worden met elkaar vergeleken. De DQW data vertonen eigenschappen die niet verklaart kunnen worden door de onderliggende fysica van de SQW. Deze eigenschappen zijn: (*i*) het verdwijnen van het $\nu = 2$ minimum voor toenemend $B_{||}$, (*ii*) het verwijden en vervolgens vernauwen van het $\nu = 3$ minimum als functie van $B_{||}$, (*iii*) het $\nu = 6$ minimum vertoont onregelmatig gedrag bij een toenemend $B_{||}$ en (*iv*) een onverwachte en nog steeds onverklaarde dip in de even ‘integer plateaus’ van de Hall weerstand. Een verklaring van de eerste drie eigenschappen

is verkregen a.d.h.v. analyse van de ‘Landau Level fans’. De laatste eigenschap wordt toegekend aan het ‘reentrant quantum Hall effect’.

List of publications

1. **G. Galistu**, A. de Visser and A.M.M. Pruisken, ‘‘*Magnetotransport study of relevant and irrelevant critical behavior in the quantum Hall regime of an InGaAs/GaAs heterostructure*’’, in preparation.

2. M.V. Yakunin, A. de Visser, **G. Galistu**, S.M. Podgornykh, Yu.G. Sadofyev, N.G. Shelushinina and G.I. Harus, ‘‘*Evolution of the spin-split quantum Hall states with magnetic field tilt in the InAs-based double quantum wells*’’ J. Phys.: Conf. Series **150** (2009) 022100.

3. M.V. Yakunin, **G. Galistu** and A. de Visser, ‘‘*Tilted magnetic field quantum magnetotransport in the double quantum well with a sizable bulk g-factor* $In_xGa_{1-x}As/GaAs$’’, Physica E **40** (2008) 1451-1453.

4. V.A. Kulbachinskii, I.S. Vasil'evskii, R.A. Lunin, **G. Galistu**, A. de Visser, G.B. Galiev, S.S. Shirokov and V.G. Mokerov, ‘‘*Electron barrier transport and optical properties of shallow GaAs/InGaAs/GaAs quantum wells with a thin central AlAs barrier*’’ Semicond. Sci. Techn. **22** (2007) 222-228.

5. A. de Visser, L.A. Ponomarenko, **G. Galistu**, D.T.N. de Lang, A.M.M. Pruisken, U. Zeitler and D. Maude, ‘‘*Quantum critical behavior of the plateau-insulator transition in the quantum Hall regime*’’ J. Phys.: Conf. Series **51** (2006) 379-386.

Acknowledgements

Even though I believe that happy endings are rare in this life, the fact that I am writing these acknowledgements right now convinces me that once in a while they do occur. I would like to use these final pages to express my gratitude to the people that contributed to the completion of this thesis.

First I would like to express my gratitude to my co-promotor and supervisor Dr. Anne de Visser. Thank you for introducing me into the surreal world of experimental low temperature physics. Thank you for your efforts to instill into me the right attitude of an experimentalist, for your daily guidance and support and not in the least, for patiently checking and correcting this manuscript. Likewise I would like to thank my promotor Prof. Aad Pruisken, the inspired theoretician. Thank you for being a guide to us experimentalists, for your very useful suggestions on how to do data-analysis, and as member of the inner core from the very beginning, for elaborating to me what it took over the years to reach the latest understanding of scaling within the quantum Hall effect. Even though my field of research will change now from 2-dimensional to 3-dimensional systems, which in addition, are also breathing (hopefully!), I am sure I will take the luggage you both gave to me into my future life.

Then there are my senior *quantum Hall* colleagues. Leonid, next to being a friend you were also like an older brother to me, always keeping a watchful eye on the youngest sibling of the quantum Hall group. Dennis, even though it was a very busy period for you when I joined the group, you still took plenty of time to explain complicated concepts to me and were always available for advice. Thank you so much. This is not to forget my *non quantum Hall* group members. Huy, I really appreciated your friendship during the last years. Many memories… the two of us building up the labs…having fun during summer school in Switzerland…you were always disposed to help, to listen, to share … I have to keep my promise and come to visit you in Vietnam. And then there is Alessia, this other one of a kind. Thank you Ale for assisting me in the lab, sometimes even in the weekend and also for occasionally correcting my use of Italian language (and eating habits). Meena

and Erik also a kind word for you. I feel that you are all special people that gave color to this journey called Ph.D.

An important part of the work in this thesis could not have been done without the help of our colleagues from Eindhoven. Many thanks to Paul Koenraad, P.Nouwens and H. Kunzel from the Technical University of Eindhoven for assisting us and providing useful samples to us. Thanks to Ulrich Zeitler for his support during the experiments in the HMFL in Nijmegen.

The work presented in the last two chapters of this thesis has been done in collaboration with Vladimir Kulbachinskii from the Moscow State University and Michael Yakunin from the Institute of Metal Physics in Ekaterinburg, Russia. Thank you for sharing your knowledge and expertise with me. I really enjoyed working together with you. Also I would like to mention Ivan Vasilievsky from the Moscow State University for his efforts and advice in analyzing the data obtained in Amsterdam.

Where would we researchers be without the people from the mechanical and electronic workshop and all the others assisting research and other matters going on in the WZI. In particular Ben 'labview' Harrison, Frans Pinkse, Joost Overtoom, Wietze Buster, Harry Beukers, Johan te Winkel, Bert Zwart, Hans Agema, Theo van Lieshout, Piet Sannes, Ton Gortemulder, Rene Rik, Luuk Lusink, Dirk de Vries, Ineke Baas, Mariet Bos, Rita Vinig and all the others thank you so much! You are some of the friendliest people I have met during my stay in Amsterdam.

Special thanks to Mark Golden for caring about the smaller issues going on outside his own group. It is my humble opinion that you have set some standards on how a good director should be. Thanks to the other staff members for the interesting discussions and support. Jeroen Goedkoop, Gerard Wegdam, Jacques Klaasse, Ekkes Bruck and Rudolf Sprik.

Also I want to mention my other colleagues in the WZI and some from the ITFA that contributed to a pleasant time in the WZI. Tracy, Stan, Iman, Jorge, Tegusi, Lian, Henk, Duc, Nacho, Anton, Freek, Sanne, Cam Tanh, Salima, Abdel, Asmae, Mounir, Antje, Phil, Antina and Vijay, thank you for your kindness, Nazly, Oleg, Ha, Abdullaye, Rijn, Jesse, Sara, Wing Kiu, Vinh, Mark K., Salvo, Richard, Sasha, Xerxes, Bahar, Ingmar, Gerardo, Pasquale, Michele, Mark A. and all the other colleagues and friends that in the tunnel-like

focusing of my mind caused by writing this thesis I forgot to mention here.

Beyond what I can express by the written word is the gratitude that I have for my parents, for their unconditional love and encouragement. *Cari papa e mama, non ho parole per ringraziarvi, vi voglio tanto bene*. Also I want to mention my brother Tore, my future sister in law Carol, my uncles and aunts, especially zia Angela and zio Mario, cousins and the rest of my family. I hope this booklet will bring a smile on your faces.